Title: Extracellular matrix and microglial regulation of cognitive aging

Authors: Daniel T. Gray[1], Abigail Gutierrez[1], Yasaman Jami- Alahmadi[2], Vijaya Pandey[2], Lin Pan[3], Ye Zhang[3], James A. Wohlschlegel[2], Ross A. McDevitt[4], Lindsay M. De Biase[1]

Author Affiliations:

1. Department of Physiology, David Geffen School of Medicine, University of California, Los Angeles. Los Angeles, CA 90095
2. Department of Biological Chemistry, David Geffen School of Medicine, University of California, Los Angeles. Los Angeles, CA 90095
3. Department of Psychiatry and Biobehavioral Sciences, Semel Institute for Neuroscience and Human Behavior, David Geffen School of Medicine, University of California, Los Angeles. Los Angeles, CA 90095
4. Comparative Medicine Section, National Institute on Aging, Baltimore, MD, United States of America

Co-Corresponding Authors: Daniel T. Gray and Lindsay M. De Biase

Department of Physiology, David Geffen School of Medicine

University of California, Los Angeles

10833 Le Conte Avenue, 76-100E CHS; Los Angeles, CA 90095

E-mail address: dtgray@mednet.ucla.edu; lmdebiase@mednet.ucla.edu

Abstract

Synapse dysfunction is tightly linked to cognitive changes during aging. Emerging evidence suggests that microglia and the extracellular matrix (ECM) can potently regulate synapse integrity and plasticity. Yet the brain ECM, and its relationship with microglia, synapses, and cognition during aging remains virtually unexplored. Using ECM-optimized proteomic workflows and histological analyses, we discovered striking regional differences in ECM composition and aging-induced ECM remodeling across key basal ganglia nuclei. Moreover, we combine two distinct behavioral classification strategies with fixed-tissue confocal imaging and proteomic analysis to identify robust relationships between the hyaluronan- and proteoglycan-rich ECM and cognitive aging phenotypes. Finally, we provide evidence that aging midbrain microglia lose capacity to interact with and regulate the ECM, and that these aging-associated microglial changes are accompanied by local ECM accumulation and worse behavioral performance. Together, these foundational observations implicate changing microglia-ECM-synapse interactions as a key determinant of cognitive functioning during healthy aging.

Main

Synapse loss and changes in synaptic plasticity are hallmark features of both normative brain aging and preclinical phases of neurodegenerative disease[1–3]. These synaptic changes have critical consequences, as preserved synapse status is linked to better cognitive outcomes in healthy aged rodents and nonhuman primates[1,4]. Growing evidence suggests the extracellular matrix (ECM) is a robust regulator of synaptic physiology during development and in early adulthood[5,6]. The ECM is not a static structure, but rather a dynamic network of proteins and carbohydrates remodeled to support numerous brain functions including synaptic plasticity and tissue repair[5–7]. Histochemical staining of ECM components suggests that ECM abundance[8] and composition[9,10] vary across brain regions and that ECM remodeling can occur during aging[7,11,12]. This raises the possibility that ECM status helps determine vulnerability of specific brain regions to aging-related synaptic decline.

Relative to other bodily tissues, the brain ECM is relatively depleted in fibrous ECM proteins like collagens and elastins and enriched in glycosylated proteins like proteoglycans[5,13,14]. Ongoing regulation of the brain ECM is a cooperative effort amongst different neuronal, vascular, and glial cell subtypes involved in ECM protein and carbohydrate synthesis, assembly, and degradation[5,6,15]. Microglia, the brain's innate immune cells, express numerous ECM-relevant degradative enzymes as well as protease inhibitors[16–18], positioning them as potent modifiers of ECM structure. Microglia also regulate synapses[19–24], including through a recently discovered mechanism involving targeted degradation of ECM proteoglycans[7,25,26]. Moreover, microglial properties are substantially altered during aging, and changes in microglial density in the cerebral cortex are associated with ECM alterations in mouse models of Alzheimer's disease and aging macaques[27,28]. Together, these observations suggest that changes in microglia-ECM interactions may play central roles in shaping synapse dynamics during aging, and consequently patterns of age-associated cognitive decline. Yet, this microglia-ECM-synapse triad remains virtually unexamined in most brain regions in both young adulthood and aging.

Numerous cognitive deficits associated with normative aging have been linked with dysregulation in midbrain dopaminergic circuits[29,30]. Microglia near midbrain dopamine neurons exhibit robust aging-related phenotypes characterized by increases in proliferation and inflammatory factor production that are evident by middle age in mice[31]. Whether these premature microglia aging phenotypes coincide with changes in ECM composition, and whether microglial-ECM responses to aging impact cognitive phenotypes remains unexamined. This study combines high-resolution imaging, quantitative tissue proteomics, and sophisticated behavioral-characterization strategies to comprehensively map how microglial-ECM responses to aging in the basal ganglia align with individual differences in synapse status and cognition.

Results

ECM-optimized proteomics reveals strong associations between ECM and synapse abundance in the aging basal ganglia

ECM proteins are highly glycosylated and comparatively insoluble, making it difficult to leverage traditional proteomic approaches to comprehensively map the brain ECM (i.e., matrisome). We compared two tissue processing workflows that have been used for ECM enrichment and analysis in peripheral bodily tissues: solubility-based subcellular fractionation[32] and chaotropic extraction and digestion[33]. While the two approaches identified similar numbers of structural ECM proteins (core matrisome) in brain tissue, subcellular fractionation on average was more efficient at enriching ECM proteoglycans, while chaotropic digestion better enriched more fibrous ECM proteins like collagens **(Ext. Data Fig. 1**). Given the relative enrichment of proteoglycans in brain tissue[13,14], we used the solubility-based workflow to create the first comprehensive proteomic mapping of the aging ECM proteome in the midbrain and striatum, two key basal ganglia nuclei, from young-adult (3 months) and aged (20+ months) wild-type mice (**Figure 1a**).

Volcano plots of the abundance of all proteins in the tissue showed a relatively even split between proteins that were up- and down-regulated during aging (**Figure 1b**). In contrast, most core matrisome proteins increased in abundance during aging. Beyond protein abundance, changes to the structure and assembly of the matrix can occur and will be reflected in alterations to solubility of specific ECM components. As expected, in both brain regions, ECM proteins were primarily detected in more insoluble tissue fractions (**Figure 1c**). In the midbrain, individual ECM proteins exhibiting significant aging-related changes in abundance were relatively equally distributed across solubility fractions (**Figure 1d**). In the striatum, however, the majority of individual matrisome proteins that changed in abundance with age were found in the most insoluble fraction (**Figure 1d**). These regional differences were also observed at the level of protein abundances such that midbrain ECM protein abundances showed similar aging-related increases across subcellular fractions (**Figure 1e**) whereas striatum ECM protein abundances disproportionately increased within insoluble fractions during aging (**Figure 1e**). To probe this data further, we determined the number of ECM proteins showing significant changes in solubility during aging. This analysis revealed that just 6 percent of midbrain ECM proteins became more soluble in older animals and none more insoluble, whereas no striatal ECM protein became more soluble and 18 percent became more insoluble (**Ext. Data Fig 1**). These results indicate there are important regional differences in both the abundance and solubility of ECM proteins at different points of the lifespan.

Core matrisome proteins fall into 3 subclasses: glycoproteins, proteoglycans, and collagens. Comparable numbers of glycoproteins were detected in the midbrain and striatum, and several were significantly upregulated in both regions with aging (e.g., VWA 1, TARP). Laminin glycoproteins were specifically upregulated in the aging striatum (**Figure 1f**). More proteoglycans were detected in the midbrain compared to striatum, and nearly half of midbrain proteoglycans showed significant increases in abundance with age compared to just 1 in the striatum (**Figure 1f**). Collagen abundances also varied prominently between regions, with eight distinct collagens detected in the midbrain compared to just two in striatum (**Figure 1f**). Finally, several ECM regulatory proteins, which include metalloproteinases and protease inhibitors, were significantly more abundant in the aged midbrain (HTRA1, ADAM10, Cystatin C), whereas none changed in abundance with aging in the striatum (**Figure 1f**). Together, these observations demonstrate that regional heterogeneity in ECM composition and modulation during aging extends to all three subclasses of ECM proteins and their regulators.

To relate matrisome status with other features of the whole tissue proteome, Weighted Gene Coexpression Network Analysis[34] was leveraged for unbiased identification of protein co-expression patterns (**Figure 2a**). This analysis identified 12 modules of covarying proteins. Most core matrisome (~82%) and synapse proteins (~63%) were members of yellow, brown, or tan modules (**Figure 2a**), highlighting these modules as warranting further analysis. Innate immune proteins, which can play key roles in synapse remodeling[23], were also found within yellow (15%) and brown modules (12%), in addition to prominent presence in the turquoise (33%) module. Examination of module eigengenes revealed stark regional differences for the brown, yellow, and tan modules, but not the turquoise module (**Figure 2b**). Pathway analysis indicated that brown module proteins were associated with numerous metabolic processes, yellow with chemical synaptic transmission, turquoise with RNA metabolism and translation, and tan with a mix of biological processes including ECM organization (**Figure 2c**).

To further evaluate relationships between these modules and ECM, synapse, and immune proteins, we treated individual protein abundances as “traits” and examined their correlation with module eigengenes across samples (**Figure 2d**). Striking associations were observed between ECM proteoglycans and brown/yellow/tan module eigengenes, with the hyaluronan linker proteins HAPLN1-4 and aggrecan showing significant correlations. Although many immune signaling proteins also showed significant associations with brown/yellow/tan module eigengenes (**Ext. Data Fig. 2**), complement proteins C1qA and C1qB, which are known to tag synapses for microglial engulfment[23], were only significantly correlated with turquoise module eigengenes. Finally, numerous synaptic proteins showed relationships with brown/yellow/tan module eigengenes, whereas very few correlated significantly with the turquoise module. Collectively, these observations suggest that synaptic and ECM protein abundances are tightly linked in the basal ganglia, and that complement signaling may not be involved in targeted ECM remodeling in these brain regions.

Overall abundance of most synaptic proteins did not significantly differ between young-adult and aged mice, indicating that substantial synapse *loss* is likely not occurring in the basal ganglia during healthy aging (**Figure 2e**). This aligns with previous reports showing that, while synapse loss does occur in vulnerable brain regions during healthy aging, synapse numbers remain stable in many others[1,35]. To further explore relationships between age-associated changes in ECM composition (**Figure 1**) and synapse status, we carried out additional pathway analysis focusing only on module proteins that were significantly altered during aging. Visualizing identified pathways as network plots revealed interconnected clusters of brown/yellow/tan module proteins associated with ECM organization and ECM-receptor interactions in the midbrain. This cluster was directly connected to clusters associated with synapse organization (bolded lines; **Figure 2f**), meaning that functional annotation predicts that proteins within these pathway “nodes” influence one another. While similar ECM clusters were observed in the striatum, they were not directly connected to pathway nodes associated with synapse organization (**Ext. Data Fig. 2**), suggesting that age-associated ECM remodeling has region-specific relationships with synapse status. Together, this proteomic mapping of matrisome, synapse, and immune proteins indicates that, in a normative aging context, regional variation in ECM status plays key roles in establishing and/or maintaining regional basal ganglia synapse profiles.

Mesolimbic ECM networks differ across region and age and are positioned for synapse interactions

Although proteomic approaches provide unbiased and comprehensive quantification of ECM protein abundance, they cannot reveal the morphology and spatial distribution of ECM

169 components. For independent analysis of brain ECM proteoglycans during aging, we
170 histologically examined the ventral tegmental area (VTA, midbrain) and nucleus accumbens
171 (NAc, ventral striatum), first using Wisteria floribunda agglutinin (WFA), a lectin that
172 preferentially labels N-acetylgalactosamine residues that are most commonly found on
173 chondroitin sulfate proteoglycans (i.e., aggrecan, brevican, neurocan, phosphacan)[36–39]. High-
174 resolution (63x) confocal images were acquired from young-adult (4 months) and late-middle-
175 aged (18 months), wild-type C57Bl6 mice, and ECM field-of-view coverage was calculated. In
176 both the VTA and NAc, WFA label was distributed relatively evenly across fields of view and
177 perineuronal net accumulations were only occasionally observed, indicating presence of a
178 prominent interstitial matrix in both regions (**Figure 3b**). WFA tissue coverage was similar
179 between the VTA and NAc of young-adult mice, and substantially greater in the VTA of middle-
180 aged mice compared to young (**Figure 3c**). Chondroitin sulfate proteoglycans are sometimes
181 referred to as 'hyalectans' due to their ability to interact with the ubiquitous ECM scaffold
182 hyaluronan via several different linker proteins (hyaluronan and proteoglycan link proteins;
183 HAPLNs)[40]. Because proteomic mapping suggested that numerous hyalectans and HAPLNs
184 were significantly upregulated in the aged midbrain (**Figure 1**), and because hyaluronan is
185 positioned to play central roles in determining overall ECM tissue topology[26,41], we also
186 histologically examined hyaluronan in young-adult and late-middle-aged mice. Hyaluronan
187 tissue coverage was greater in the VTA compared to NAc, and on average higher in the VTA
188 during aging (**Figure 3e**). Together, these histological findings are consistent with proteomic
189 detection of greater midbrain ECM protein levels during aging (**Figure 1f**) and indicate that one
190 prominent feature of VTA aging is an accumulation of the proteoglycan-rich ECM.

191 Proteoglycans anchored to hyaluronan can impact synapses via multiple mechanisms,
192 including limiting structural remodeling and regulating lateral diffusion of neurotransmitter
193 receptors[7,42]. To relate ECM structure to local synapse status, densities of excitatory pre- and
194 post-synaptic proteins (VGlut1 and Homer2, respectively) were quantified (**Figure 3f**). Both
195 VGlut1 and Homer2 densities were greater in the NAc compared to VTA but not altered by
196 aging in either region (**Figure 3g; Ext. Data. Figure 3)**, consistent with proteomic data
197 suggesting minimal synapse loss in the aging midbrain and striatum. The abundance of
198 colocalized VGlut1-Homer2 puncta, which may better represent functional synapses, also did
199 not differ with age in either region (**Ext. Data. Figure 3).** To probe spatial relationships between
200 ECM and synapses, hyaluronan fibrils were reconstructed and dilated by 0.5 μm, to estimate the
201 density of Homer2 puncta within the potential territory of proteoglycans anchored to this scaffold
202 (**Figure 3h**)**.** In both regions, hyaluronan-homer2 spatial associations were greater than would
203 be expected by chance (associations detected when rotating one fluorescence channel by 90
204 degrees, **Figure 3i**), supporting the idea of functional associations between local ECM and
205 synapses. The density and proportion of Homer2 within 0.5 μm of hyaluronan was similar in
206 young-adult and late-middle-aged mice and not different across regions, although greater
207 variability was observed in the NAc. Together, these histological findings validate regional ECM
208 heterogeneity revealed by proteomics, confirm regional differences in age-associated ECM
209 remodeling, and suggest that ECM-synapse spatial associations occur throughout life.

210

211 *Microglia-ECM relationships during normative aging*

212 VTA microglia exhibit robust aging-related phenotypes characterized by changes in
213 proliferation, morphology, and inflammatory factor production[31], raising the possibility that
214 microglia contribute to ECM accumulations in the aging VTA. Furthermore, aging-related
215 increases in ECM protein abundance at the level of tissue proteomics (**Figure 1**) arose
216 alongside increases in the abundance of most detected microglia-enriched proteins with

advanced age (**Figure 4a**). To examine whether changes in microglial and ECM abundance align in the aging VTA, we histologically co-labelled the ECM (hyaluronan) and microglia (IBA1) in young-adult (4 months) and late-middle-aged (18 months) wild-type mice and examined relationships between the two. VTA microglia densities were greater in middle-aged mice compared to young-adults (**Figure 4b;** see scatter plot). Microglia densities were significantly positively correlated with hyaluronan tissue coverage in young-adult mice, and this significant relationship was lost in the older mice (**Figure 4b**). Next, microglial morphology was evaluated using a 2-dimensional Sholl analysis and, as shown previously[31], aged VTA microglia exhibited fewer Sholl intersections compared to young, indicative of a less complex morphology (**Ext. Data Fig. 4**). As with microglia densities, microglial morphological complexity was significantly positively correlated with hyaluronan deposition in young-adult mice and this relationship was lost in the older animals (**Figure 4c**). To determine whether VTA microglia make direct contact with the hyaluronan matrix, reconstruction of microglia and hyaluronan was carried out in Imaris using tissue from young-adult (3-4 months), middle-aged (12-17 months) and aged (18-22 months) $Cx3Cr1^{EGFP/+}$ mice, which enable precise visualization of microglial morphology. VTA microglia in young mice made relatively regular putative contacts with hyaluronan fragments, both along their processes and proximal to microglial somas. Quantification of the density of hyaluronan contacts normalized to GFP signal revealed an age-associated decrease in microglia-hyaluronan contacts in the VTA (**Figure 4d**). This raises the intriguing possibility that loss of ability of VTA microglia to interact directly with hyaluronan networks is related in some way to greater hyaluronan deposition within the tissue.

Young-adult VTA microglia attenuate ECM deposition

To probe observed correlations between ECM deposition and microglial properties in the VTA, we examined tissue from young-adult (3-4 months) microglia-deficient mice ($Csf1r^{\Delta FIRE/\Delta FIRE}$ mice; **Figure 4e**)[43]. Compared to control mice, $Csf1r^{\Delta FIRE/\Delta FIRE}$ mice exhibited higher VTA hyaluronan deposition but no difference in Homer2 densities (**Figure 4f, 4g**), as observed in aging wild-type mice (**Figure 3**). Together with findings that the ECM accumulates with age in the VTA (**Figure 3**), these observations suggest that young-adult microglia attenuate ECM deposition in the VTA and that this microglial function is diminished with normative aging. While elevated hyaluronan deposition was not associated with altered numbers of postsynaptic structures in either aging wild-type or microglia-deficient mice, these changes likely impact proteoglycan deposition around synapses and modify capacity for synapse plasticity[5].

Next, we sought to examine the ECM in a context where microglia are present but undergoing distinct aging trajectories. Cx3Cr1 deficiency has been suggested to alter microglial aging phenotypes[31,44], impact synaptic plasticity[45], and regulate ECM composition in other bodily tissues[46,47]. Indeed, when we mined a published RNAseq dataset[44] of microglia from young-adult (2 months) and middle-aged (12 months) wild-type (WT) and Cx3Cr1-deficient (KO) mice, we found that over 50 matrisome-related genes (both structural ECM proteins and ECM regulatory proteins) were differentially expressed in 2mo KO microglia compared to 2mo WT microglia (**Ext. Data Fig. 4**). Critically, more ECM-relevant genes were altered during aging in WT microglia compared to the number that were altered during aging in KO microglia, indicating that Cx3Cr1-deficiency perturbs ECM-related aspects of microglial aging. The most robust difference between genotypes was an age-related upregulation of genes associated with negative regulation of peptidase and hydrolase activity in WT microglia that was absent in KO microglia (**Figure 4h; Ext. Data Fig. 4**). Altogether, these results indicate that Cx3Cr1-deficiency is a suitable manipulation to probe how altered microglial aging trajectories impact the ECM.

Via immunostaining, we found that VTA microglia from KO (*Cx3Cr1*$^{EGFP/EGFP}$; KO) mice exhibited reduced morphological complexity compared to Cx3Cr1-heterozygous (*Cx3Cr1*$^{EGFP/+}$, HET) mice, confirming that this manipulation enhances features of VTA microglial aging that we have reported previously (**Ext. Data Fig. 4**)[31]. We then examined ECM (WFA) and synapse abundance (Homer2) in the VTA of young-adult (3-4 months) and middle-aged (12-18 months) WT and KO mice. WFA tissue coverage was significantly greater in KO mice compared to WT both in young-adulthood and middle-age (**Figure 4i**), and this same effect was also observed in the NAc (**Ext. Data Fig. 5**). Moreover, age-related ECM accumulations observed in WT mice was absent in KO mice (**Figure 3**; **Figure 4i**), further supporting the hypothesis that Cx3Cr1-defiency alters ECM-related aspects of microglial aging phenotypes. Intriguingly, hyaluronan abundance was not significantly different between WT and KO mice at any age (**Ext. Data. Fig. 5**), suggesting that effects of Cx3Cr1-deficiency on ECM regulation preferentially impact some ECM components over others. KO mice exhibited significant reductions in Homer2 density by middle age, unlike WT mice where synapse numbers were stable into late middle age (**Figure 3; Figure 4j**). Analysis of colocalization between microglia, hyaluronan, and homer2 in KO mice indicated that putative microglial hyaluronan engulfment was not different with age (**Ext. Data. Fig. 5**). Putative microglial synapse engulfment was also not different in young-adult and middle-aged KO mice (**Ext. Data. Fig. 5**), indicating that age-associated reductions in synapse density in these mice do not arise from greater microglial synapse engulfment. Together these results indicate that WT microglia have an attenuating effect on ECM deposition relative to contexts where microglia are absent or altered, and that during normative aging this microglial function is lost to some degree. It will be critical to replicate these observations using conditional microglial manipulations, as some findings may be influenced by developmental compensations that arise in constitutive models.

Hyaluronan and synapse remodeling in the VTA aligns with reward-based memory in middle-aged mice

Healthy brain aging is an active process that engages endogenous mechanisms of plasticity to protect circuit function as aging-related challenges emerge[48]. To begin understanding whether ECM accumulations in the aging VTA represents vulnerabilities or adaptive responses that support continued circuit function, we developed a behavioral paradigm that engages reward circuitry and probes aspects of dopamine-relevant cognition known to be altered with aging, including reward memory and cognitive flexibility (**Figure 5a**)[29,49]. In this task, mice learn to explore a large arena and forage for palatable food reward that changes location daily. During testing, mice encode a rewarded location and, after 2 or 24 hours, reenter the arena with 4 unrewarded feeders to measure their memory of the rewarded location (probe trials; **Figure 5a**). Mice then immediately re-enter the arena and are allowed to consume food reward in the previously rewarded location to minimize extinction of training (**Figure 5a**). In total, mice undergo 5 weeks of training/testing (5 days/week), which allows for robust assessment of cognitive status of individual mice and minimizes behavioral variables like novelty and stress at the time when tissue is collected for histological examination.

Both young-adult (4 months) and late-middle-aged (18 months) non-food-restricted mice learned the task and exhibited consistent foraging at similar points of the experiment timeline (**Figure 5b, Ext. Data Fig. 6**). Average walking speeds, start box exit latencies, and proportion of time on the arena perimeter did not differ between age groups, indicating similar levels of task engagement and absence of prominent age-related differences in anxiety-like behavior (**Figure 5b).** During probe sessions, young-adult mice showed similar performance that was better than chance following both 2- and 24-hour delays. Middle-aged mice performed comparably to

young-adults with a 2-hour delay but made fewer correct feeder visits and more errors following 24-hour delays (**Figure 5c**). Critically, we observed higher variability in middle-aged mice during 24-hour probe trials compared to young, which is a hallmark of cognitive aging[50]. Hence, this nuanced behavioral paradigm establishes a strategy to probe links between cellular/molecular features of mesolimbic dopaminergic circuits and age-associated changes in reward-based cognition.

To enable assessment of the impact of the 5-week behavioral training itself, each cohort of mice included sedentary controls housed in the same vivarium as behaving mice for the duration of the experiment (**Figure 5e**). Compared to sedentary mice, behavior-trained mice exhibited significantly less hyaluronan within the VTA (**Figure 5f, 5g**), particularly at middle-age. Hence, the accumulation of VTA hyaluronan observed in aging sedentary animals appeared to be mitigated by engaging in behavioral training. Furthermore, middle-aged mice with lower hyaluronan densities showed better task performance (**Figure 5h**), indicating that this remodeling is beneficial. Behavior-induced hyaluronan remodeling was not observed in multiple other brain regions examined, including the NAc, mPFC, and retrosplenial cortex (**Ext. Data Fig. 6**). Behavior-associated hyaluronan reductions were observed in the substantia nigra pars compacta and hippocampus, suggesting that hyaluronan remodeling occurs only in specific circuits when animals repeatedly engage with reward-based spatial memory tasks.

To link behavior-induced VTA hyaluronan remodeling with synapse status, Homer2 was also analyzed in these mice. Compared to sedentary mice, behavior-trained mice had elevated Homer2 puncta densities, indicating that behavioral training/testing had net synaptogenic effects (**Figure 5i, 5j**). Surprisingly, however, behavior-trained mice with fewer synapses showed better task performance (**Figure 5k**), suggesting that synapse refinement that impacts performance may also occur across this 5-week paradigm. In sedentary mice, hyaluronan tissue coverage and Homer2 puncta densities were not correlated in either young-adult or late-middle-aged mice. Importantly, however, a significant positive correlation between hyaluronan tissue coverage and homer2 densities was observed in middle-aged mice that underwent behavioral training, but not in the young-adults (**Figure 5l**). Furthermore, behavior-trained middle-aged mice with more hyaluronan tissue coverage had a higher density of Homer2 puncta within 0.5 µm of hyaluronan (see ECM-synapse proximity analysis; **Figure 3h**), and again this relationship was not seen in young-adult mice or in sedentary mice at either age (**Figure 5m**). Together, these experiments suggest that greater VTA hyaluronan abundance may stabilize excitatory synapse numbers but limit synaptic refinements that optimize reward-driven behavior in aging mice.

Proteomic signatures of cognitive phenotypes in middle-aged mice

Because histochemistry cannot provide comprehensive quantitative information on large families of proteins, we sought to use tissue proteomics to identify matrisome and synapse protein expression patterns associated with cognitive function in aging mice. To this end, young-adult (4 months) and late-middle-aged (18 months) wild-type mice were tested on 3 standard mouse behavioral paradigms: an open field test of anxiety-like behavior, a novel object recognition (NOR) test of non-spatial recognition memory, and a T-maze test of spontaneous alternation behavior (**Figure 6a**). These 3 behaviors were selected due to their relatively high-throughput nature, allowing for a more rapid assessment of cognitive status while minimizing remodeling effects of extended behavioral training, and because this behavioral battery will be more easily replicated across laboratories within different experimental contexts. Middle-aged mice on average exhibited lower discrimination and alternation on the NOR and T-maze tasks, respectively, both of which are indicative of poorer performance. As in the foraging paradigm

(**Figure 5**), middle-aged mice also exhibited higher variability in performance across tasks. Leveraging this variability, we performed unbiased hierarchical clustering analysis to cognitively classify all mice tested in this pipeline. This analysis resulted in two parent clusters, one containing 75% of the young-adult mice and roughly half (46%) of the middle-aged mice, and another cluster containing the remaining animals. Using these clusters, we categorized the mice into 3 groups: young average, middle-aged unimpaired, and middle-aged impaired (**Figure 6a**). Midbrains were harvested from mice in each age and cognitive group and subjected to solubility-based subcellular fractionation (**Figure 1)**, and membrane, cytoskeletal, and insoluble fractions were analyzed via mass spectrometry.

Principal component analysis (PCA) of entire proteomes from each fraction revealed the emergence of group separations between middle-aged impaired and unimpaired mice **(Ext. Data. Fig. 7),** suggesting links between the overall midbrain proteome and cognitive status of middle-aged mice. When restricting PCA analysis only to matrisome proteins, more prominent separations with respect to age and cognitive status were apparent across subcellular fractions (**Figure 6b**), supporting the idea that midbrain ECM status critically shapes cognition during aging. Among ECM subfamilies, proteoglycans showed more robust group separations in membrane and cytoskeletal fractions, while glycoproteins showed the greatest separation in insoluble fractions **(Ext. Data. Fig. 7)**. These observations suggest that both the abundance and subcellular localization/solubility of proteoglycans play roles in maintaining cognitive function with advanced age.

Proteoglycan abundance in membrane and cytoskeletal fractions was substantially higher in middle-aged mice compared to young (**Figure 6c; Ext. Data Fig. 7**). In membrane fractions, proteoglycan abundance was also significantly greater in middle-aged impaired mice compared to unimpaired (**Figure 6c**), whereas this separation in proteoglycan abundance with respect to cognitive status was not observed in either the cytoskeletal or insoluble fractions (**Ext. Data Fig. 7**). To evaluate what specific proteins drive these relationships, regression analyses between abundances of individual proteoglycans, age, and cognitive status were performed. This approach revealed that the predominant proteoglycans driving separations between middle-aged impaired and unimpaired mice were multiple HAPLNs (proteins that anchor proteoglycans to hyaluronan) and chondroitin sulfate proteoglycans (e.g., aggrecan, brevican, etc.; **Figure 6c**). Consistent with our prior proteomic analyses, many of these proteins increased in abundance during aging and showed significant positive correlations with age. Moreover, supporting the idea that this accumulation is not beneficial cognitively, many of these same proteins exhibited significant negative correlations with behavioral performance. As observed in our prior proteomic dataset, abundance of most synaptic proteins in these tissues did not change with age (**Figure 6d; Ext. Data. Fig. 8**), although multiple neurotransmitter receptors were negatively correlated with behavioral performance, indicating that middle-aged mice with less synaptic protein performed better on the cognitive battery (**Figure 6d; Ext. Data. Fig. 8**). This data provides an independent verification that having lower ECM proteoglycan and excitatory synapse abundances in the midbrain is cognitively beneficial for middle-aged mice and identifies the hyaluronan-proteoglycan matrix as a key modulator of cognitive aging phenotypes.

Synapse and ECM abundance on dopamine neurons map onto cognitive aging phenotypes

Proteomic mapping in cognitively classified mice indicated that hyalectan abundances strongly align with cognitive phenotypes in middle-aged mice (**Figure 6**). In the subset of cognitively characterized mice (**Figure 6a**) that did not undergo proteomic analysis, we sought to independently validate this finding via immunohistochemistry for HAPLN1, an ECM link

409 protein that directly interacts with hyaluronan, and aggrecan, an abundant chondroitin sulfate
410 proteoglycan in the brain. HAPLN1-aggrecan complexes were found throughout the VTA,
411 primarily near the surfaces of dopamine neurons and other neuronal or glial cells (**Figure 7a**),
412 suggesting that HAPLN1 likely helps organize hyaluronan-proteoglycan interactions within the
413 VTA. While field of view (FOV) HAPLN1 abundance did not differ across age, middle-aged
414 impaired mice exhibited significantly higher HAPLN1 abundances compared to middle-aged
415 unimpaired mice (**Figure 7b**). Aggrecan abundance did not differ with age or cognitive status
416 (**Figure 7b**), although there were trends toward increased aggrecan abundance in middle-aged
417 impaired mice. When analysis was restricted to zones within ~0.5μm of dopamine neuron
418 surfaces, we observed that HAPLN1 abundance was greater in middle-aged mice, and trending
419 towards being significantly higher in impaired mice compared to unimpaired mice (**Figure 7c**).
420 Aggrecan abundance on dopamine neurons did not differ with age or cognitive status. However,
421 the abundance of aggrecan-HAPLN1 *complexes* on dopamine neuron surfaces was greater in
422 middle-aged mice and also trending towards being significantly higher in impaired mice
423 compared to unimpaired mice ($p = 0.07$; **Figure 7g; Ext. Data Figure 9**). These observations
424 suggest that local ECM proteoglycan deposition on and around dopamine neurons critically
425 informs overall cognitive performance during late middle age.

426 To further explore the role of dopamine-neuron-localized ECM in cognitive aging, we
427 carried out similar analyses in tissue from mice trained in our 5-week food reward foraging
428 paradigm (**Figure 5**), as well as sedentary controls (**Figure 7d**). Synapse abundance, as
429 assessed via Homer2, on dopamine neurons did not differ between sedentary and behaving
430 mice or across age. However, middle-aged animals with fewer dopamine-neuron-localized
431 Homer2 puncta exhibited better task performance (**Figure 7e, 7f**), consistent with FOV analyses
432 indicating that fewer VTA synapses correlated with better performance (**Figure 5k**). Hyaluronan
433 abundance on dopamine neurons was lower in behavior-trained mice compared to sedentary
434 mice (**Ext. Data Fig. 9**), agreeing with FOV findings that behavior training reduces hyaluronan
435 density (**Figure 5g**). Importantly, both young and aging behavior-trained mice with more
436 hyaluronan on dopamine neurons had significantly more Homer2 on dopamine neurons (**Figure**
437 **7g**). This correlation was completely absent in sedentary mice, suggesting that behavioral
438 training engages hyaluronan-synapse remodeling around VTA dopamine neurons, and that
439 failure to generate *and refine* these complexes is associated with cognitive decline in aging.
440 Collectively, these histological observations identify hyaluronan and proteoglycan link proteins
441 as promising targets for future mechanistic studies of cognitive resilience vs. decline.

442

443 *Microglia and ECM abundances independently correlate with cognitive aging phenotypes*

444 Our findings in the context of microglial depletion (*Csfr1*$^{\Delta FIRE/\Delta FIRE}$) and altered microglial
445 aging trajectory (*Cx3cr1*$^{EGFP/EGFP}$, Cx3cr1 KO) indicate that microglia may be poised to regulate
446 abundance of VTA hyaluronan and proteoglycans (**Figure 4**). Moreover, in the context of
447 normative aging, VTA microglial density was correlated with abundance of hyaluronan, and our
448 results suggest that reduced microglial-ECM contact may contribute to ECM accumulations. To
449 further probe potential links between microglial aging in mesolimbic circuits and cognition, we
450 quantified VTA and NAc microglial densities in tissue from mice trained in the 5-week food
451 reward foraging paradigm. As we showed previously, microglia densities were higher in the NAc
452 compared to VTA and increased with aging only in the VTA (**Figure 8a, 8b**)[31]. Middle-aged mice
453 with more VTA microglia exhibited worse task performance (**Figure 8c**), highlighting
454 associations between this feature of microglial aging and cognition. Surprisingly, NAc microglia
455 densities showed the opposite relationship, where mice with greater microglial densities

exhibited better performance (**Figure 8c**). This suggests that regional microglial specializations and aging phenotypes uniquely impact the neuronal circuits in which they reside.

Proteomic mapping also revealed increased abundance of multiple microglia-enriched proteins in the aged midbrain, and many of these increases were associated with age-related cognitive impairment (**Figure 8d**). The strong alignment between ECM abundance and cognitive aging phenotypes (**Figure 4**) prompts the question of whether microglia-ECM interactions influence cognitive aging, or whether their associations with cognition are independent of one another. To glean insights into this question, we first performed regression analyses between individual ECM proteoglycan abundances from cognitively-characterized aging mice (**Figure 6**), and total microglial and synapse receptor abundances in tissue proteomes from the same mice (**Figure 8e**). This analysis suggested that microglial protein abundances were not strongly aligned with most ECM proteoglycan abundances, although a significant negative correlation was observed with HAPLN2. Conversely, synapse receptor abundances showed strong positive relationships with HAPLN1-4 and all chondroitin-sulfate proteoglycans detected in this tissue (**Figure 8e**). To further evaluate these relationships, correlation network plots that integrate cognitive performance with microglial, ECM, and synapse abundances (measured via proteomics and histology) were created. In these plots, nodes represent individual features, and line thicknesses represent r values of pairwise correlations between traits. In young-adult mice, microglia abundances were strongly correlated to both ECM and synapse abundances, both of which showed relatively pronounced correlations with cognition (**Figure 8f**). In middle-aged mice, however, microglial relationships with both ECM and synapse abundances were drastically reduced, and ECM-synapse and ECM-cognition relationships were substantially higher (**Figure 8f**). Taken together, these analyses suggest that microglia and the ECM somewhat independently influence cognitive aging trajectories, and that ECM-synapse dynamics become more central to cognitive processing during normative aging.

Discussion

As the predominant structure occupying the extracellular space, the ECM is positioned to play central roles in almost all neurological processes. Yet, brain ECM research remains nascent, and optimal strategies for observing and measuring the ECM's complexity are still being defined. Revealing how the ECM impacts discrete brain structures – such as synapses – is a challenge for the field. ECM near synapses can regulate AMPA receptor diffusion, positioning of neuronal pentraxins[42,51], extracellular ion concentrations, and access of phagocytic cells to synaptic elements[26,52]. Moreover, the "sweet spot" of optimal ECM abundance near synapses depends on context; appropriate ECM deposition may protect against synapse loss, but targeted ECM degradation is also essential for structural plasticity in support of learning and memory[7]. Advancing knowledge in this area is likely to reshape our understanding of synapse regulation in the aging brain and illuminate novel approaches to manipulate the brain ECM in support of healthy circuit function.

This report presents comprehensive proteomic mapping of the brain ECM during normative aging and reveals stark regional heterogeneity in ECM composition and age-associated remodeling across different basal ganglia nuclei. This argues that findings about the ECM in one brain region cannot be generalized to other brain regions and that similar ECM mapping of additional brain regions in a wide variety of contexts (CNS development, brain injury, brain cancer, neurodegeneration, etc.) is urgently needed. In general, basal ganglia matrisome protein abundance increased during aging, and histological examination of ECM proteoglycans and glycosaminoglycans confirmed this increase, aligning with previous biochemical and gene expression studies[53,54]. In the same tissue, we found no evidence of substantial aging-related synapse loss in the midbrain or striatum across multiple histological and proteomic datasets. This differs from previous reports that have shown age-related synapse loss in forebrain regions, including the prefrontal cortex and hippocampus[1,55,56]. These discrepancies could either reflect true brain region differences or that the present study primarily focused on middle-aged rather than geriatric mice. In terms of regional heterogeneity, the NAc had significantly more excitatory synapses and less ECM deposition compared to the VTA. This raises the possibility that NAc networks are more malleable, as the ECM is thought to restrict plasticity since, for example, the closing of developmental critical periods aligns with drastic increases in ECM abundance[57]. Furthermore, it may suggest that, although excitatory VTA synapse numbers remain stable with age, those synapses may also become increasingly rigid as VTA ECM deposition increases during aging.

Indeed, our data reveals multiple lines of evidence implicating the ECM as a key regulator of basal ganglia synapse function even in the absence of any changes to synapse number. For example, unbiased computational analyses of our proteomic data revealed that abundance of specific synaptic proteins strongly aligned with WGCNA modules containing ECM proteins, arguing that even in the absence of changes in synapse *number*, there is a critical role for the ECM in shaping synapse structure and composition. Histological analyses also revealed close anatomical proximity between postsynaptic markers (homer2) and hyaluronan, consistent with a structural and potentially functional relationship between ECM components and synaptic elements. Surprisingly, this analysis also revealed that synaptic protein abundances were not aligned with WGCNA modules containing complement proteins. Thus, while microglial synapse engulfment through complement tagging has been implicated in numerous disease contexts[23,58,59], our data argues that local ECM status plays more prominent roles in regulating synapses during healthy brain aging. An important future direction for this research will be to examine relationships between basal ganglia ECM, immune, and synapse protein status using isolated synaptosomes, which allow for a more targeted quantification of synapse-associated proteomes[60]. Additionally, it will be critical to directly measure synaptic activity and capacity for

synaptic plasticity and relate such measures to aging-related changes in ECM abundance and composition.

Our observation that middle-aged mice with *fewer* excitatory synapses exhibited better cognitive performance across both naturalistic foraging behaviors (paired with histology) and high-throughput behavioral assays (OF, NOR, T-maze - paired with proteomics) was rather unexpected. These observations challenge prevailing assumptions that more synapses automatically equates to better cognition[4,35] and suggest that positive cognitive aging outcomes depend critically on the ability to refine and remodel synaptic networks. In support for this idea, we observed that repeated engagement in naturalistic foraging-based behavior had a net synaptogenic effect for both young and late-middle aged mice. However, mice that performed best on the foraging tasks had *fewer* excitatory postsynaptic puncta, implying that capacity to remodel rather than retain synapses is critical for optimal circuit function. Critically, in both behavioral experiments, greater synaptic protein levels and poorer cognitive performance were also associated with greater ECM abundance. These findings support a model in which excessive ECM accumulation may constrain the synapse remodeling and pruning required for optimal cognition[6,7,61,62], and extends this framework into the context of normative brain aging. Moreover, these findings carry important implications for pathological aging contexts, including presymptomatic neurodegeneration or recovery from brain injury, where compensatory synaptogenic responses have been observed[63–65]. Our data argue that if these newly formed synapses are not appropriately refined, they may, at best, fail to facilitate appropriate circuit activity, and, at worst, exacerbate network dysfunction and cognitive decline through formation/retention of aberrant or inefficient synaptic connections. Nonetheless, an important limitation of our study is lack of information about the source and identity of synaptic inputs into the VTA and midbrain. Future studies leveraging connectivity mapping and *in vivo* functional imaging will be essential to fully understand how ECM-driven synaptic dynamics contribute to circuit-level adaptations and cognitive resilience in aging.

One unique feature of the VTA is that microglia within this region exhibit accelerated aging phenotypes, characterized by increases in proliferation and inflammatory factor production, compared to microglia in other basal ganglia nuclei[31]. Here, we provide critical replication of these VTA microglial aging patterns and build on this work by identifying what may be a previously unrecognized feature of midbrain microglial aging - a loss of capacity to contact and regulate the ECM. Several key findings support this hypothesis. First, while microglia densities and morphologies were significantly correlated with ECM deposition in young-adult mice, these relationships were lost by late-middle-age. Next, constitutive microglial depletion phenocopied normative age-associated increases in ECM abundance, arguing that microglia typically restrict ECM deposition and that this ability is lost during aging. Finally, perturbing microglial aging trajectories via deletion of Cx3Cr1 resulted in a failure to upregulate key ECM-regulatory genes that are upregulated in aging wild-type microglia[44], resulting in greater ECM deposition compared to wild-type mice, and a loss of excitatory postsynaptic puncta by early middle age. These findings align with recent work showing that microglia regulate ECM structure to support synaptic plasticity in young-adult brains[7,25], and argue that a loss of microglial regulation of the ECM during normative aging may contribute to excess ECM accumulation patterns we observe. An important future direction is to causally test how microglia modify ECM-synapse interactions in genetic mouse models with conditional manipulations to key microglial ECM-sensing proteins and ECM-degradative enzymes.

Our data also indicated several features of microglial aging that may impact cognition independently of microglial interactions with the ECM. For example, we found that abundance of complement proteins C1qA, C1qB, and C1qC was elevated with advanced age, consistent with previous work[67]. Via proteomic mapping of cognitive aging phenotypes, we also found that late-

580 middle-aged mice with better cognitive performance had lower levels of complement proteins.
581 Complement proteins could be influencing cognition via tagging synapses for phagocytic
582 removal or via complement-ECM interactions that shape accessibility of synapses for pruning[68].
583 However, our proteomic analysis indicates that complement proteins do not strongly align with
584 ECM- and synapse protein proteomic profiles during healthy aging. Moreover, recent findings
585 indicate that C1q interacts with neuronal ribonucleoprotein complexes in an age-dependent
586 manner, perturbing neuronal protein synthesis in a way that impacts cognition[69]. Together,
587 these observations point to both ECM-dependent and ECM-independent molecular mechanisms
588 by which microglia and immune molecules can potentially shape neural circuit function and
589 cognitive resilience during aging.

590 This study lays a robust foundation for future research of glial-matrix biology in the
591 context of cognitive aging. One of the more powerful elements of our study design was inclusion
592 of two unique and sophisticated behavioral strategies that uniquely enabled us to link distinct
593 cellular- and molecular-level observations about midbrain ECM and synapses to cognitive status
594 of individual young and aging mice. For example, by including sedentary control mice in
595 experiments where young-adult and middle-aged mice underwent reward-based behavioral
596 training, we were able to detect behavior-induced hyaluronan matrix remodeling characterized
597 by less ECM deposition around dopamine neurons that was aligned with synaptic phenotypes
598 associated with better reward-based memory. This remodeling may reflect the engagement of
599 somatodendritic dopamine release within the VTA in mice engaged in this task, as D1/D5
600 receptor activation has been linked to downstream protease release and ECM degradation[70].
601 More broadly, this observation demonstrates that ECM structure in the aging brain is not
602 passively shaped by chronological age alone, but rather actively shaped by behavioral
603 experience. This opens up exciting possibilities for non-invasive interventions (e.g., cognitive
604 training or environmental enrichment)[71,72] to modulate ECM states in support of cognitive
605 function during aging.

606 Another critical finding for cognitive aging research was that protein expression patterns
607 in tissue proteomes of late-middle-aged mice segregate solely based on unsupervised
608 classification of their performance on canonical, high-throughput behavioral phenotyping tasks.
609 This approach enabled us to directly link cognitive heterogeneity to underlying molecular states
610 and identify the hyalectans as a specific family of ECM proteins strongly aligned with cognition
611 in late-middle-aged mice. This behavioral classification strategy parallels work in the rat
612 hippocampus linking histological and electrophysiological signatures of excitatory/inhibitory
613 imbalance to poor cognitive aging[73]. More broadly, our work provides a scalable and unbiased
614 experimental framework for appropriately sampling cognitive variability in aging mice in support
615 of downstream experiments aimed at mechanistically dissecting cognitive resilience vs. decline.

616 While this work establishes novel pipelines for aligning ECM composition with cognitive
617 performance, the immense complexity of the ECM leaves much to be uncovered. For example,
618 our regional proteomic mapping experiments revealed aging-related changes in numerous
619 perivascular ECM molecules (e.g., collagens and laminins) that have been linked to microglial
620 activation patterns and remodeling of the neuronal ECM[74]. Given the important links between
621 neurovascular health and cognitive function during aging[75,76], it will be critical for future studies
622 to focus on aging-related changes in the basement membrane-associated ECM in the context of
623 cognitive aging. Moreover, our current methods provide limited insight into ECM assembly and
624 spatial architecture beyond colocalization patterns. While we did not detect major shifts in
625 solubility of most midbrain ECM proteins, we did observe aging-related differences in
626 hyaluronan fragment size and filament length. Hyaluronan size has been shown to influence
627 membrane excitability, diffusion properties in the extracellular space, and receptor
628 signaling[26,77,78]. It will be important for future studies to understand how these subtler changes in

629 ECM composition influence such physiological processes in the healthy aged brain. In this
630 regard, there is evidence that unique post-translational modifications on ECM proteoglycans
631 (i.e., hydroxylation, sulfation, and glycosylation) can alter key aspects of ECM physiology and its
632 regulation of neuronal function during aging[10,11]. While our primary findings are based on
633 relative comparisons within consistent experimental and analytical frameworks, our proteomic
634 database searches did not include assessment of these ECM-relevant post-translational
635 modifications, meaning that we likely underestimated matrisome protein abundance[79–81] and
636 cannot provide insights into more subtle changes in matrisome composition. A key future
637 direction will be to implement proteomic pipelines and enrichment strategies that incorporate
638 ECM-relevant post-translational modifications in order to capture the full complexity of the aging
639 brain matrisome and its relationship with cognition.

640 Furthermore, there remains a pressing need for more precise and physiologically-
641 relevant ECM manipulation strategies in neuroscience. Pharmacological approaches using
642 compounds like 4-methylumbelliferone, a hyaluronan synthesis inhibitor, show inconsistent
643 efficacy in the brain, require long treatment timelines, and provide limited temporal and spatial
644 control[82,83]. Enzymatic ECM-degradation strategies have also been widely implemented in brain
645 research; however, these treatments require invasive intracranial surgeries that induce
646 mechanical injuries and the associated inflammatory and glial scarring responses[84,85]. This
647 presents a major confound when examining normative aging phenotypes of neuron-extrinsic
648 factors like the ECM and microglia[86,87]. These considerations underscore the need for new tools
649 to manipulate specific ECM targets through viral approaches using retro orbital delivery[88] or
650 similar minimally invasive methods.

651 Finally, while this study identifies numerous aging-related ECM and microglial
652 phenotypes associated with cognitive impairment, brain aging is not a passive process and
653 there are numerous examples of adaptive aging-related neurobiological changes[48]. One
654 potential example from the present study was that, while VTA microglial aging phenotypes
655 aligned with worse behavioral performance, aging mice with more *NAc* microglia showed better
656 goal-directed behavior. Hence, while some aspects of microglial aging represent vulnerabilities
657 to circuit function, others may arise as adaptive responses that maintain neuronal network
658 activity. As novel technologies emerge that allow for *in vivo* monitoring of specific ECM
659 components, microglia-ECM interactions, and ECM-synapse interactions, such a framework
660 (recognizing both detrimental and adaptive/beneficial aging-induced changes) will be critical in
661 linking regional specializations in microglia-ECM-synapse dynamics with cognitive aging
662 outcomes.

663

Material and Methods

Mice

This study uses C57Bl6 wild-type mice, CX3CR1$^{EGFP/+}$ and CX3CR1$^{EGFP/EGFP}$ mice, and Csf1r$^{+/+}$ and Csf1r$^{\Delta FIRE/\Delta FIRE}$ mice[43]. C57Bl6 wild-type mice used for behavioral experiments and histochemical experiments were purchased from the National Institutes on Aging (NIA) colony (Bethesda, Maryland), and the mice used for regional proteomic mapping (**Figures 1-2**) were purchased from Jackson Laboratory (Bar Harbor, ME; stock #000664). CX3CR1$^{EGFP/EGFP}$ breeders on a C57Bl6 background were originally purchased from the Jackson Laboratory (stock #005582) and crossed with C57Bl6 wild-type mice to obtain heterozygous (CX3CR1$^{EGFP/+}$) mice and CX3CR1$^{EGFP/EGFP}$ mice to obtain homozygous mice (CX3CR1$^{EGFP/EGFP}$). In these mice, EGFP is knocked into the fractalkine receptor (CX3CR1) locus, which is a receptor expressed specifically by most myeloid-lineage cells, including microglia[90]. Previous work has demonstrated that EGFP expression in these mice is specific to microglial cells in the basal ganglia[18]. Csf1r$^{\Delta FIRE/\Delta FIRE}$ breeders on a B6CBAF1/J background were originally purchased from Jackson Laboratory (stock # 032783) and crossed with C57BL/6 mice after which their offspring were interbred. These mice carry CRISPR/Cas9-generated deletion of the fms-intronic regulatory element (FIRE) of the Csf1r gene[43].

For immunohistochemical and histochemical experiments in sedentary wild-type mice, up to 12 young-adult (4 months; 6 male, 6 female) and 12 late-middle aged mice (18 months; 6 male, 6 female) were used. Histochemical quantifications of synapse and ECM abundance in Cx3Cr1-deficient and knockout mice utilized 4 young-adult Cx3Cr1$^{EGFP/EGFP}$ (3-4 months; 2 male, 2 female) and 4 middle-aged Cx3Cr1$^{EGFP/EGFP}$ mice (12-15 months; 2 male, 2 female). Histological examinations comparing microglia-deficient mice with controls utilized 3 young-adult Csf1r$^{\Delta FIRE/\Delta FIRE}$ mice (3-4 months, 2 females, 1 male) and 3 young-adult Csf1r$^{+/+}$ mice (3-4 months, 1 female, 2 males). Quantitative proteomic experiments comparing ECM enrichment protocols utilized 8 young-adult wild-type mice (3-4 months). Midbrain tissue from 4 mice (2 male, 2 female) underwent chaotropic extraction and digestion protocol and tissue from 4 mice (2 male, 2 female) underwent the tissue fractionation protocol. Quantitative proteomic experiments of the midbrain and striatum of non-behaviorally characterized aging mice included 4 young-adult (3-4 months; 2 male, 2 female) and 4 aged (22-24 months; 2 male, 2 female) wild-type mice. Quantitative proteomic experiments of the midbrain of behaviorally-characterized mice included 6 young-adult mice (4 months; 3 male, 3 female), 5 middle-aged unimpaired (18 months; 2 male, 3 female), and 7 middle-aged impaired mice (18 months; 4 male, 3 female). Histological experiments of behaviorally characterized mice included 8 young-adult mice (4 months; 4 male, 4 female); 6 middle-aged unimpaired (18 months; 5 male, 1 female), 4 middle-aged impaired mice (18 months; 0 male, 4 female). Foraging-based behavioral testing and histological examinations utilized 18 young-adult (4 months; 9 male, 9 female) and 18 late-middle-aged (18 months; 9 male, 9 female) wild-type mice. Note that in all experiments measurements were taken from distinct samples from each animal. All mice within a given experiment were housed in the same vivarium with a normal light/dark cycle and were provided *ad libitum* access to food and water. Experiments adhered to protocols approved by the Animal Care and Use Committee and UCLA.

Transcardial perfusion, immunohistochemistry, and histochemistry

Mice were deeply anesthetized in a covered beaker containing isofluorane and perfused transcardially with 1M phosphate buffered saline (PBS; pH 7.4) followed by ice-cold 4% paraformaldehyde (PFA) in 1M PBS. All perfusions were performed between 8:00 am and 12:00

711 pm to minimize the contribution that circadian changes may have on ECM, synapse, and
712 microglial properties[91]. Brains were extracted immediately following perfusions and were
713 allowed to post-fix for ~4 hours in 4% PFA and then stored in 1M PBS with 0.1% sodium azide
714 until tissue sectioning.

715 Coronal brain sections were prepared using a vibratome in chilled 1M PBS solution and
716 stored in 1M PBS with 0.1% sodium azide until histochemical labelling. Sections containing the
717 ventral tegmental area (VTA) and nucleus accumbens (NAc) were selected using well-defined
718 anatomical landmarks at 3 distinct anterior-posterior locations per mouse. Free-floating brain
719 sections were briefly rinsed in 1M PBS (5 minutes) and then permeabilized and blocked in a
720 solution of 1% bovine serum albumin (BSA) and 0.1% saponin for 1 hour. For hyaluronan
721 labelling, sections were then incubated with a biotinylated HABP lectin (1:250; Sigma-Aldrich
722 cat: 385911) in the 1% BSA and 0.1% saponin block solution overnight at 4ºC with mild
723 agitation. Sections were washed in 1M PBS (4x10 minutes) and then incubated with
724 streptavidin-conjugated AlexaFluor-647 in the 1% BSA and 0.1% saponin block solution for 2
725 hours. The tissue underwent another 4x10 minute wash in 1M PBS, and then was blocked
726 again in 5% normal donkey serum with no additional permeabilization agent for 1 hour and was
727 then incubated overnight with mild agitation in a solution containing different combinations of
728 goat anti-GFP (1:1000; Frontier Institute cat: GFP-go-Af1480), rabbit-anti-IBA1 (1:500; Wako
729 cat: 019-19741), chicken anti-TH (1:500; Aves cat: TYH), rabbit anti-Homer2 (1:2000; Synaptic
730 Systems cat: 160 003), mouse anti-Vglut1 (1:2000; DSBH cat: N28/9), biotinylated WFA (1:100;
731 Vector Labs, B-1355), rabbit anti-aggrecan (1:200; Sigma Aldrich AB1031), goat-anti HAPLN
732 (1:200; R&D Systems cat: AF2608) and the biotinylated HABP lectin in 5% NDS solution.
733 Sections were again washed in 1M PBS (4x10 minutes). Prior to secondary antibody incubation,
734 all sections were treated with TrueBlack lipofuscin autofluorescence quencher (5%; Biotium cat:
735 23007) for 90 seconds followed by a 3x5 minute rinse in 1M PBS. Sections were then incubated
736 in a secondary antibody solution containing combinations of chicken AlexaFluor-405 or chicken
737 AlexaFluor-594, goat AlexaFluor-488 or goat AlexaFluor-647, mouse AlexaFluor-647, rabbit
738 AlexaFluor-488 or rabbit AlexaFluor594, and streptavidin-conjugated AlexaFluor-647 in 5% NDS
739 for 2 hours at room temperature with mild agitation. Experiments in which hyaluronan labelling
740 was not performed were done in 1% BSA and 0.1% saponin throughout. The sections were
741 again washed in 1M PBS (4x10 minutes), coverslipped (#1.5 thickness), and mounted using
742 Aqua-Poly/Mount (Polysciences cat: 18606).

743

744 *Image acquisition and analysis*

745 Fixed-tissue was imaged using a Zeiss LSM-700 confocal microscope using a 63x
746 objective at a z interval of 0.3 µm or a Leica STELLARIS 5 confocal microscope using 20x (z =
747 1.5) and 63x objectives (z = 0.3). For quantification of hyaluronan and WFA fibril deposition
748 patterns, 63x images were imported into Fiji image analysis software and underwent a
749 background subtraction (rolling-ball radius = 15) and de-speckling. The processed images were
750 then binarized using the 'MaxEntropy' setting and the proportion of a field of view covered by
751 hyaluronan or WFA was calculated. Hyaluronan fibril densities and sizes were assessed using
752 the 3D Object Counter plugin in Fiji using a minimum pixel cutoff of 10. Hyaluronan distribution
753 regularity was quantified in the same images using the Fractal Dimension plugin in Fiji. HAPLN1
754 and aggrecan field of view coverage was calculated by importing images into Fiji image analysis
755 software, applying a gamma correction and then a background subtraction (rolling-ball radius =
756 15). The processed images were then binarized using the 'MaxEntropy' setting and the
757 proportion of a field of view covered by HAPLN1 or aggrecan was calculated. Densities of
758 Homer2, VGlut1, putative Vglut1-Homer2 colocalization, putative hyaluronan-Homer2

759 interactions, and hyaluronan, HAPLN1, aggrecan, and Homer2 near TH-positive dopamine
760 neurons were examined in 3-dimensions using custom-written MATLAB (Natick, MA) scripts
761 using binarized images. Densities of ECM or synaptic components were normalized by the total
762 surface area of TH signal within the field of view.

763 Microglia densities were calculated by manually counting microglial cell bodies within a
764 z-stack using the Cell Counter plugin and then normalizing these counts by the volume of the
765 image. Microglial morphological complexity was examined with 2-dimensional Sholl analysis
766 using the SNT and Sholl Analysis plugin in Fiji[92]. Images containing IBA1 or GFP signal were
767 first maximum intensity projected in the z dimension. A mark was placed in the center of each
768 microglial soma and concentric radii were drawn from that point. The initial radius size was 7.5
769 µm and the step size of each radius after was 2.5 µm. The standard output values given by this
770 plugin were used for analysis. Sholl intersection plots were made using MATLAB code. Manual
771 reconstructions of microglia and the hyaluronan matrix were done by importing high-
772 magnification (63x) confocal z-stack images into Imaris (Bitplane; Belfast, UK) software for
773 reconstruction using the surfaces module. For each channel, a threshold that most accurately
774 represented the signal was manually set and surfaces smaller than 1 μm^3 were filtered out.
775 Hyaluronan-microglia contacts were captured by filtering the hyaluronan surface using the GFP
776 fluorescence histograms. The number of GFP-filtered hyaluronan aggregates was normalized
777 by the total GFP within the field of view.

778

779 *Quantitative proteomics: sample preparation*

780 Young and aged wild-type mice were anesthetized with isofluorane and perfused with
781 1M PBS. Brains were extracted and the midbrain and striatum were dissected using a scalpel,
782 minced, triturated, washed in 1M PBS, and stored at -80ºC until further processing. For
783 solubility-based fractionation experiments, the tissue was processed using protocols from Naba
784 et al., 2015[32] that use a compartment protein extraction kit (Millipore cat: 2145). Triturated brain
785 tissue was thawed on ice for ~30 minutes before being homogenized in 2 ml/g of Buffer C
786 (HEPES (pH 7.9), MgCl2, KCl, EDTA, Sucrose, Glycerol, Sodium OrthoVanadate) with protease
787 inhibitors. This mixture was rotated on ice for 20 minutes and then spun at 20,000xg at 4ºC for
788 20 minutes. The supernatant was removed and stored at -80ºC until proteomic analysis. This
789 fraction was considered the cytoplasmic fraction. The pellet was washed in 4 ml/g of the same
790 buffer (HEPES (pH 7.9), MgCl2, KCl, EDTA, Sucrose, Glycerol, Sodium OrthoVanadate) with
791 protease inhibitors, rotated for 5 minutes at 4ºC, and spun at 20,000xg at 4ºC for 20 minutes.
792 The supernatant was removed and discarded. The pellet was then incubated in 1ml/g of Buffer
793 N (HEPES (pH 7.9), MgCl2, NAcl, EDTA, Glycerol, Sodium OrthoVanadate), rotated at 4ºC for
794 20 minutes, spun at 20,000xg for 20 minutes, and the supernatant was removed and stored at -
795 80ºC until proteomic analysis. This fraction was considered the nuclear fraction. The pellet was
796 then washed in 1ml/g of Buffer M (HEPES (pH 7.9), MgCl2, KCl, EDTA, Sucrose, Glycerol,
797 Sodium deoxycholate, NP-40, Sodium OrthoVanadate), rotated at 4ºC for 20 minutes, spun at
798 20,000xg for 20 minutes, and the supernatant was removed and stored at -80ºC until proteomic
799 analysis. This fraction was considered the membrane fraction. The pellet was washed in 0.5
800 ml/g of buffer CS (Pipes (pH6.8), MgCl2, NAcl, EDTA, Sucrose, SDS, Sodium OrthoVanadate),
801 rotated at 4ºC for 20 minutes, spun at 20,000xg for 20 minutes, and the supernatant was
802 removed and stored at -80ºC until proteomic analysis. This fraction was considered the
803 cytoskeletal fraction. The final remaining insoluble pellet was also stored at -80ºC for proteomic
804 analysis. This fraction was considered the insoluble fraction.

805 Chaotropic extraction and digestion experiments followed protocols from McCabe et al.,
806 2023[33], with the following modifications: Frozen samples were milled into powder in liquid

807 nitrogen using a mortar and pestle. Approximately 5 mg of tissue was resuspended in a fresh
808 prepared high-salt buffer (50 mM Tris-HCL, 3 M NaCl, 25 mM EDTA, 0.25% w/v CHAPS, pH
809 7.5) containing 1x protease inhibitor (Halt Protease Inhibitor, Thermo Scientific) at a
810 concentration of 10 mg/ml. The samples were vortexed for 5 minutes and rotated at 4° C for 1
811 hour. The samples were then centrifuged for 20 minutes at 18,000xg at 4° C. The supernatants
812 were discarded, and the pellets were resuspended in a high-salt buffer, vortexed for 5 minutes,
813 and rotated again at 4° C for 1 hour. The samples were then recentrifuged for 15 minutes at
814 18,000xg at 4° C and the final pellets were used for proteomic analysis.

815 50-100ug protein was processed for mass-spectrometry analysis. Samples were
816 resuspended in an equal volume of 100mM Tris-Cl (pH 8) and 8M urea. Proteins were then
817 reduced with TCEP, alkylated using IAA, and cleaned using SP3 beads. Proteolytic digestion
818 was performed overnight using lysC enzymes and trypsin. Peptides were subsequently cleaned
819 using the SP3 protocol and eluted in 2% DMSO. Following elution, samples were dried in a
820 speed vacuum and the resulting peptides were resuspended in 5% formic acid prior to liquid
821 chromatography–tandem mass spectrometry (LC-MS/MS) analysis.

822

823 *LC-MS/MS parameters and database search*

824 For quantitative proteomic experiments comparing ECM enrichment strategies (**Ext.**
825 **Data Figure 1; Supplementary Table 1**) and experiments comparing midbrain and striatum
826 proteomes of non-behaviorally characterized aging mice (**Figure 1; Supplementary Table 2**),
827 LC-MS/MS was carried out as detailed in[93]. Approximately 200-500ng peptide amounts were
828 subjected to LC-MS/MS analysis. Briefly, peptide separation was carried out using reversed-
829 phase chromatography on a 75 µm inner diameter fritted fused silica capillary column, which
830 was packed in-house to a length of 25 cm with 1.9 µm ReproSil-Pur C18-AQ beads (120 Å pore
831 size). An increasing gradient of acetonitrile was delivered using a Dionex Ultimate 3000 nano-
832 LC system (Thermo Scientific) at a constant flow rate of 200 nL/min. Tandem mass spectra
833 (MS/MS) were acquired in data-dependent acquisition (DDA) mode on an Orbitrap Fusion
834 Lumos Tribrid mass spectrometer (Thermo Fisher Scientific). Full MS1 scans were acquired at a
835 resolution of 120,000, followed by MS2 scans at a resolution of 15,000. The raw LC-MS/MS
836 data were analyzed using the MaxQuant computational platform[94]. The Andromeda search
837 engine, integrated within MaxQuant, was employed for peptide identification against the UniProt
838 reference proteome for *Mus musculus* (UP000000589). Search parameters allowed a maximum
839 of two missed tryptic cleavages and included cysteine carbamidomethylation as a fixed
840 modification and N-termination acetylation and methionine oxidation as variable modifications. A
841 false discovery rate (FDR) threshold of 1% was applied at both peptide and protein levels.
842 Label-free quantification (LFQ) was enabled, with a minimum LFQ ratio count set to one.
843 Precursor ion and fragment ion mass tolerances were set at 20 ppm and 4.5 ppm, respectively.
844 The resulting MaxQuant output files were subsequently used for statistical analysis to identify
845 differentially enriched proteins. Raw data files have been deposited in the MassIVE proteomics
846 repository under accession number MSV000096508. MS metrics and metadata information can
847 be found in **Supplementary Table 3**.

848 For quantitative proteomic experiments of the midbrain of behaviorally-characterized
849 mice (**Figure 6; Supplementary Table 4**), the cytosolic (CS), membrane (M), and insoluble
850 (Insol) fractions were subjected to sequential reduction and alkylation steps using 5 mM tris(2-
851 carboxyethyl)phosphine (TCEP) and 10 mM iodoacetamide, respectively. Following this, the
852 protein aggregation capture (PAC) protocol, as described by Batth et al., (2019)[95] was employed
853 to purify the reduced and alkylated proteins. Proteins were then enzymatically digested
854 overnight at 37 °C using Lys-C and trypsin proteases. The resulting peptide mixtures were dried

855 completely and prepared for subsequent LC-MS/MS analysis. Dried tryptic peptides were
856 resuspended in 5% formic acid and subjected to liquid chromatography-tandem mass
857 spectrometry (LC-MS/MS) analysis using a Vanquish Neo ultra-high-performance liquid
858 chromatography (UHPLC) system coupled to an Orbitrap Astral mass spectrometer (Thermo
859 Fisher Scientific, Bremen, Germany). Briefly, peptide samples were introduced into a PepSep
860 C18 reverse-phase analytical column (150 mm × 150 µm, 1.7 µm particle size), maintained at
861 59 °C, and separated using a trap-and-elute workflow. The UHPLC system employed mobile
862 phase A consisting of water with 0.1% formic acid and mobile phase B consisting of acetonitrile
863 with 0.1% formic acid. Peptide separation was achieved using a 15-minute chromatographic
864 gradient with the following composition: 5% B from 0–1 min at a flow rate of 2.45 µL/min; a linear
865 increase from 5% to 15% B from 1–5 min at 1.75 µL/min; 15% to 25% B from 5–12.6 min at
866 1.75 µL/min; 25% to 38% B from 12.6–13.6 min at 1.75 µL/min; and a rapid gradient from 38%
867 to 80% B between 13.6–13.7 min at 2.45 µL/min, followed by a hold at 80% B until 15 min,
868 maintaining the flow at 2.45 µL/min.

869 Mass spectrometric acquisition was carried out in data-independent acquisition (DIA)
870 mode on the Orbitrap Astral instrument operating in positive electrospray ionization mode. MS1
871 survey scans were acquired across an m/z range of 380–980 with a resolution of 240,000, using
872 a normalized AGC (automatic gain control) target of 500% and a maximum injection time of
873 3 ms. For DIA, sequential isolation windows of 4 m/z were used to comprehensively cover the
874 380–980 m/z range. Fragment ion (MS2) spectra were acquired at a resolution of 80,000, with a
875 normalized higher-energy collisional dissociation (HCD) energy of 25%, an AGC target of 500%,
876 and a maximum injection time of 7 ms. The raw Thermo .RAW files were analyzed using DIA-
877 NN software, searching against an in silico predicted spectral library generated from the Mus
878 musculus reference proteome (UniProt ID: UP000000589), as described by Demichev et al.,
879 (2020)[96]. The resulting DIA-NN outputs were processed using FragPipe Analyst to identify
880 differentially expressed proteins, following the workflow outlined by Hsiao et al., (2024)[97]. All raw
881 data files have been deposited in the MassIVE proteomics repository under accession number
882 MSV000096508. MS metrics and metadata information for these data can be found in
883 **Supplementary Table 5**.

884

885 *Quantitative proteomics: analysis*

886 Protein intensity values for all samples were batch corrected via quantile normalization
887 and median centering. For regional mapping experiments of ECM protein abundance across
888 subcellular/solubility fractions (**Figure 1c-1e**), age-related shifts in protein solubility were
889 examined by calculating the fold-change of individual ECM protein abundance (log2-normalized
890 protein intensities) that were detected across at least 2 distinct fractions (fold change relative to
891 the more insoluble fraction), and comparing these fold-changes between young-adult and aged
892 mice. For regional mapping experiments of total ECM protein abundance, and WGCNA analysis
893 (see below), data for each identified protein was summed across solubility fractions for each
894 mouse and log2 normalized for analysis to estimate total protein intensity. For proteomic
895 mapping of cognitive phenotypes, log2-normalized protein intensities detected in membrane,
896 cytoskeletal, and insoluble fractions were examined independently. This proteomic mapping
897 was only performed on midbrain tissue. To be included in the analysis, a protein needed to be
898 detected in 75% or more of the samples within a brain region. Fold changes were calculated as
899 the ratio of the aged signal relative to the young signal. Statistical significance was assessed
900 using unpaired t-tests with an alpha-level of 0.05. Annotations for different protein classes were
901 downloaded from publicly available online databases. ECM protein annotations were

902 downloaded from the Matrisome project database[98], innate immune system protein annotations
903 from the InnateDB database[99], and synapse protein annotations from the SynGo database[100].

904

905 *Quantitative proteomics: weighted gene correlation network analysis (WGCNA)*

906 To examine relationships between age, cognitive status, synaptic, matrisome, and innate
907 immune proteins, proteomic data underwent unsupervised clustering using Weighted Gene
908 Correlation Network Analysis (WGCNA) in R[34]. For the regional mapping experiment, processed
909 log2(intensity) data from the midbrain and striatum were used for network construction. One
910 striatal sample from an aged female mouse was identified as an outlier and removed from this
911 analysis. WGCNA provides modules of covarying proteins that are agnostic to traits of the
912 samples (i.e., age, region, sex). The distribution of synaptic, matrisome, and immune proteins
913 across the protein modules was used to identify modules of interest for further analysis.
914 Relationships between modules and external traits or protein abundance were examined using
915 the module-trait relationship code provided in the WGCNA R package. Process enrichment
916 analysis of the protein modules was conducted in Metascape[101] using default parameters. For
917 the proteomic mapping of cognitive phenotypes experiment, only proteomic data from the
918 midbrain was used for WGCNA analysis. Using age and cognitive status (see below) as traits,
919 protein-trait relationships were derived using the module-trait relationship code provided in the
920 WGCNA R package.

921

922 *Mining of published RNAseq data from wild-type and Cx3Cr1 deficient microglia*

923 Publicly available bulk RNA-seq datasets of isolated microglia from Cx3cr1 knockout
924 (Cx3cr1$^{-/-}$), Cx3Cr1 heterozygous (Cx3cr1$^{+/-}$), and wild-type mice were retrieved from Gyoneva
925 et al., 2019[44]. Analysis was restricted to a curated list of matrisome genes, defined according to
926 the MatrisomeDB[98], encompassing core ECM proteins and ECM regulators. Fold changes of
927 aging-induced changes in matrisome genes were extracted from datasets comparing 2 month
928 and 12 month old Cx3Cr1-knockout and wild-type mice. Additionally, fold changes of matrisome
929 gene expression between Cx3Cr1 heterozygous and Cx3Cr1 homozygous knockout (Cx3cr1$^{-/-}$)
930 mice (2 months old) were examined. This targeted approach enabled the identification of
931 Cx3cr1-dependent alterations in microglial ECM-associated gene expression.

932

933 *Foraging-based behavioral testing procedures*

934 For the foraging-based behavioral experiment, behavioral testing was conducted in a
935 large square open field (120 cm x 120 cm) with 35 cm high walls made from transparent
936 Plexiglas. On one wall, there was a 20 cm x 20 cm opening where a start box equipped with a
937 guillotine door was placed. This start location did not change across testing sessions. Mouse
938 bedding was placed on the floor of the arena, and 2 intra-arena reference cues were placed at
939 two fixed locations for the entire experiment. To also provide fixed distal landmarks to the mice,
940 black corrugated plastic was placed on two adjacent walls in the arena, and white corrugated
941 plastic was placed at the other two. Plexiglas dishes were filled with Sandtastik play sand
942 (Sandtastik Products LLC, Port Colborne Ontario) and were used to plug 5TUL purified rodent
943 tablets into (TestDiet; cat: 1811142; Quakertown, PA) to engage foraging behavior. Identical
944 feeders without reward pellets were used as distractor feeders to test goal-directed memory.
945 The feeders were placed at 1 of 4 locations within the arena. All feeders were sham baited with
946 powdered reward pellets (5% by weight). Mouse behavior was recorded using a 1.3 megapixel,

947 low-illumination overhead camera (ELP; Shenzhen, Guangdong, China) and Bioserve Viewer
948 software (Behavioral Instruments; Hillsborough, NJ).

949 Young-adult (3-4 months) and late-middle-aged (16-18 months) mice were ordered in 3
950 cohorts of 20. Twelve mice from each cohort then underwent behavioral testing and the other 8
951 lived with the behavior-trained mice but did not undergo testing (sedentary controls). Thus, in
952 total this experiment used 24 sedentary mice (12 young, 12 middle-aged; 6 male and 6 female
953 in each group) and 36 behavior-trained mice (18 young, 18 middle-aged; 9 male and 9 female in
954 each group). Sample sizes were determined based on variability in pilot data and from
955 published data on a similar task from which this one was derived[102].

956 Behavior-trained mice were handled daily for 1 week prior to testing. During week 1 of
957 testing (habituation phase) mice were placed within the start box for ~2-3 minutes prior to the
958 guillotine door opening to allow entry into the arena. A single sand well with 4 reward pellets
959 was placed at one of the reward locations and the mice were allowed 5 minutes to explore the
960 arena and retrieve the reward. This procedure was repeated daily for 5 sessions for each
961 mouse and the location of the rewarded feeder was changed daily and was counterbalanced
962 within a day across mice. During weeks 2 and 3 (training phase), the mice again entered the
963 arena via the start box and foraged for reward in a single sand well at one location in the arena
964 for 5 minutes (encoding). Following a 30-minute delay period, mice reentered the arena with the
965 rewarded feeder in the same location and 3 unrewarded feeders in the other locations for 2
966 minutes (retrieval). Note that this is a win-stay strategy. Again, the location of the rewarded
967 feeder was changed daily for each mouse. Each mouse underwent 10 training sessions across
968 2 weeks of testing. In the final 2 weeks of testing (test phase), mice repeated the encoding
969 procedures described above. Following either 2- or 24-hour delays, mice underwent a probe
970 test in which 4 unrewarded feeders were placed within the arena, 1 at the previously rewarded
971 location. After 2 minutes the mice exited the arena through the guillotine door and the
972 experimenter placed reward pellets in the previously rewarded location. The mice then
973 reentered the arena and consumed the food reward to minimize extinction. Again, rewarded
974 locations changed across sessions, and the 2- and 24-hour delays were interleaved to eliminate
975 practice effects between the two conditions.

976

977 *Foraging-based behavioral testing data analysis*

978 Mouse behavioral tracking was collected using Bioserve Viewer software in 1-second
979 timestamps and was used to determine the time of entry and exit to various zones of interest
980 within the arena. These zones included the reward feeder locations, and a box that separated
981 the arena's perimeter from the center. Data were exported from the Bioserve Viewer software
982 and loaded into Matlab for behavioral analysis using custom-written scripts. From this data the
983 following output measures were derived: average running speed, start-box exit latency,
984 proportion of time on the arena's perimeter, number of feeder visits, proportion of feeder visits to
985 the correct feeder, the relative proportion of time in correct and incorrect feeders, and the
986 number of errors prior to correct feeder visits. Note that because there were 4 foraging
987 locations, chance performance during probe trials is 25% for proportional measures and 1.5 for
988 error measures. Probe trial data were used as the estimate of goal-directed memory function in
989 these mice.

990 The temporal progression of the emergence of foraging behavior was tracked across
991 sessions for each animal with a state-space modeling approach using Bernoulli observation
992 models[103]. Mice were considered to have foraged if they consumed at least 1 of the 4 treats
993 within the arena during the encoding sessions. Using this binary assessment (1 = consumed, 0

994 = non consumed), a learning curve, its 90% confidence bounds and the trial at which consistent
995 foraging was observed were determined. This trial was defined as the point in which the lower
996 bound of the 90% confidence interval exceeded chance (50%) and stayed above chance for the
997 remainder of the experiment.

998

999 *Behavioral battery for proteomic mapping of cognitive phenotypes*

1000 For behavioral characterization experiments using spontaneous rodent behaviors, 12
1001 young-adult (4 months; 6 male and 6 female) and 24 middle-aged (18 months; 12 male and 12
1002 female) were used. First, all mice underwent an open field test to assess general locomotor
1003 activity and anxiety-like behavior using a square arena (60cm x 60 cm with opaque walls 30 cm
1004 high). Mice were placed in the center of the arena and allowed to explore freely for 10 minutes.
1005 Their behavior was tracked with an overhead camera using Bioserve Viewer software, and the
1006 floor of the arena was digitally divided into central and peripheral zone to calculate the
1007 proportion of time spent in the center and periphery of the arena. The arena was cleaned with
1008 70% ethanol and water between mice. Following open-field testing, all mice then underwent a
1009 novel object recognition (NOR) task in the same behavioral apparatus. Because testing was
1010 done in the same apparatus, the open field test also served as habituation for the NOR test.
1011 Thus, NOR testing began with familiarization of two identical objects (either two LEGO stacks or
1012 two PVC pipes of equal height and width, counterbalanced across subjects) that were placed
1013 symmetrically near the corners of the arena. Mice again were allowed to explore for 10 minutes.
1014 Using a separate group of aging mice, we confirmed that mice did not inherently prefer one
1015 object over the other by placing one of each object within the arena and allowing mice to
1016 explore for 10 minutes. After a retention interval of 2 hours, NOR mice underwent the test phase
1017 of the task where one familiar object was replaced with a novel object. The position of the novel
1018 object (left/right) was counterbalanced across subjects to control for side preference. Again
1019 mice explored for 10 minutes. Object exploration was defined as the mouse directing its nose,
1020 within 2 cm from the object. Using this data, a discrimination index was calculated as follows:
1021 (time with novel – time with familiar) / (total time with both objects). Objects were cleaned with
1022 70% ethanol and water between trials. Following NOR testing, mice underwent a T-maze
1023 spontaneous alternation test. This testing was done in a t-shaped maze made of white
1024 corrugated plastic comprising of a start arm and two goal arms. Each arm was 30 cm long, 10
1025 cm wide, and 25 cm tall. During the first trial, mice were forced into either a right or a left
1026 decision using a removable barrier. This forced choice was counterbalanced between mice.
1027 During all subsequent trials, mice were allowed to freely choose between the two goal arms.
1028 After entering one of the goal arms, mice were returned to the start arm for the subsequent trial.
1029 The procedure was repeated for 10 consecutive trials, with an inter-trial interval of ~30 seconds.
1030 An alternation was recorded when the mouse chose the goal arm opposite to the one it entered
1031 on the previous trial, and an alternation index was calculated as follows: number of alternations /
1032 total number of trials.

1033

1034 *Classification of middle-aged unimpaired and impaired mice*

1035 To behaviorally classify middle-aged mice as cognitively impaired or unimpaired,
1036 behavioral data from open field, NOR, and the T-maze were used for unsupervised hierarchical
1037 clustering analysis. For each mouse, a behavioral performance vector was created using the
1038 proportion of time on the arena perimeter from the open field test, the discrimination index from
1039 the NOR test, and the alternation index from the T-maze. All data was z-scored prior to
1040 constructing these vectors to ensure equal weighting across features. Hierarchical clustering

1041 was performed in MATLAB using the 'linkage' function with Ward's method (minimizing total
1042 within-cluster variance) and Euclidean distance as the similarity metric. A dendrogram was
1043 generated using the 'dendrogram' function to visualize hierarchical relationships between
1044 subjects. Clusters were identified by applying a threshold to the dendrogram (via cluster function
1045 with k=2), resulting in two distinct clusters. Middle-aged mice that fell within the cluster with the
1046 majority of young mice (75%) were considered unimpaired and the middle-aged mice that fell in
1047 the other cluster were considered impaired. This data-driven behavioral classification was then
1048 used to examine group-level differences in proteomic and histological data.

1049

1050 *Statistical analysis*

1051 Statistical analyses were done using either MATLAB or R. Statistical significance of
1052 proteomic protein-intensity data was evaluated using unpaired t-tests. Immunohistochemical
1053 data was statistically analyzed using multi-way ANOVAs with Tukey's post-hoc tests where
1054 applicable, and foraging behavior data was assessed using repeated-measures ANOVAs and
1055 unpaired t-tests. All statistical tests included age and sex (wild-type) or age, sex, and genotypes
1056 (Cx3Cr1 KO) as covariates and were two-sided. Relationships between anatomical variables
1057 and behavioral variables, or between different anatomical variables were assessed using robust
1058 regression analyses. Relationships between proteomic data and cognitive status were
1059 examined using point-serial correlation analysis (regression with one binary variable). To
1060 visualize relationships between all behavioral, anatomical, and proteomic variables created in
1061 both behavioral experiments, a correlation-based network analysis was performed in MATLAB.
1062 Here, a pairwise Pearson correlation matrix was computed across all behavioral measures
1063 using the 'corrcoef' function with pairwise deletion for missing data. Self-correlations on the
1064 diagonal ($r = 1$) were set to zero to exclude self-links in the resulting network. This network was
1065 then visualized as an undirected graph using the 'graph' function. For all experiments, a
1066 significance cutoff of $p < 0.05$ was used. Potential sex differences in ECM, microglia, and
1067 excitatory synapse status were evaluated in all cases, and all statistical parameters and test
1068 statistics are available in **Supplementary Table 6**.

Data Availability: Statistical source data is provided with this paper in supplementary files. Raw quantitative proteomics datasets were deposited in the MassIVE online database (accession number MSV000096508). Any other data is available upon request from the authors.

Code Availability: Custom code used for analyses are available on CodeOcean (capsule number: 18-559067-0).

1076 **Figures and Figure Legends**

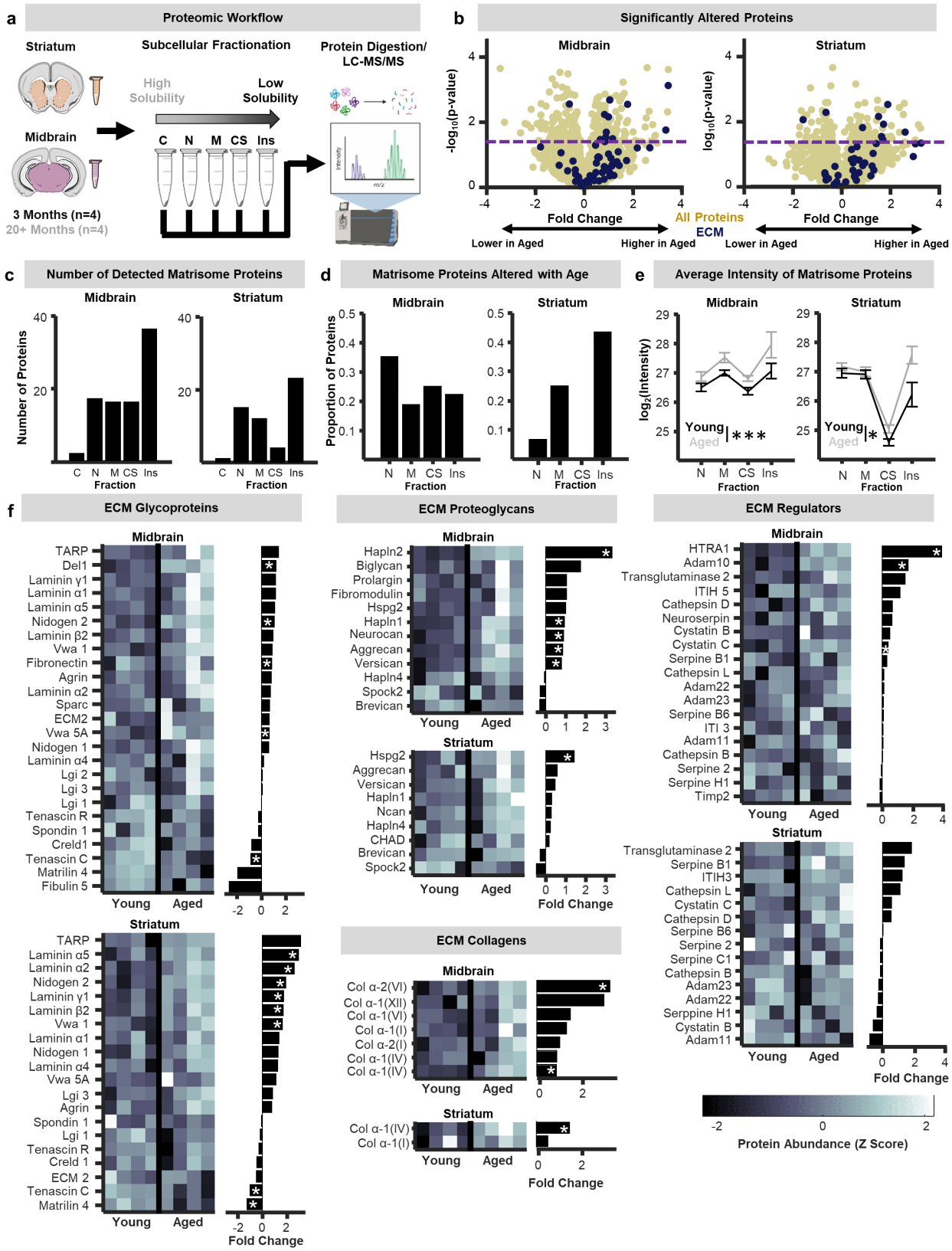

1077

1078 **Figure 1. a)** Schematic of the proteomic workflow. The midbrain and striatum of young-adult (3
1079 months) and aged (20-24 months) wild-type mice were extracted. Tissue underwent a solubility-
1080 based subcellular fractionation protocol that yielded multiple samples of proteins with
1081 decreasing solubility that correspond to cytoplasmic, nuclear, membrane, and cytoskeletal
1082 subcellular localizations, and a final insoluble pellet. All samples were then sent for liquid
1083 chromatography with tandem mass spectrometry (LC-MS/MS) analysis. **b)** Volcano plots of all
1084 proteins pooled across solubility fractions for the midbrain and striatum. Dark blue dots denote
1085 individual structural extracellular matrix (ECM) proteins (e.g., core matrisome) detected in each
1086 region. Fold-changes were calculated with respect to the aged mice (positive values indicate
1087 greater with age). **c)** Bar plots of the number of core matrisome proteins detected across the
1088 different subcellular fractions in the midbrain and striatum. **d)** Bar plots depicting the proportion
1089 of structural ECM proteins that exhibited significant increases or decreases in abundance with
1090 age ($p < 0.05$; unpaired t-test). **e)** Average log2-transformed intensity values of core matrisome
1091 proteins across the nuclear, membrane, cytoskeletal, and insoluble fractions for young-adult
1092 (black) and aged (grey) mice in the midbrain and striatum. Protein concentrations were higher in
1093 the aged mice across the nuclear, membrane, cytoskeletal, and insoluble fractions in the
1094 midbrain ($p < 0.001$; n-way ANOVA) and striatum ($p < p < 0.001$; n-way ANOVA). **f)** Heat maps
1095 of protein abundances (z scored) and bar plots of corresponding fold-changes with age for ECM
1096 glycoproteins, proteoglycans, collagens, and ECM regulators (* $p < 0.05$; unpaired t-test).

1097

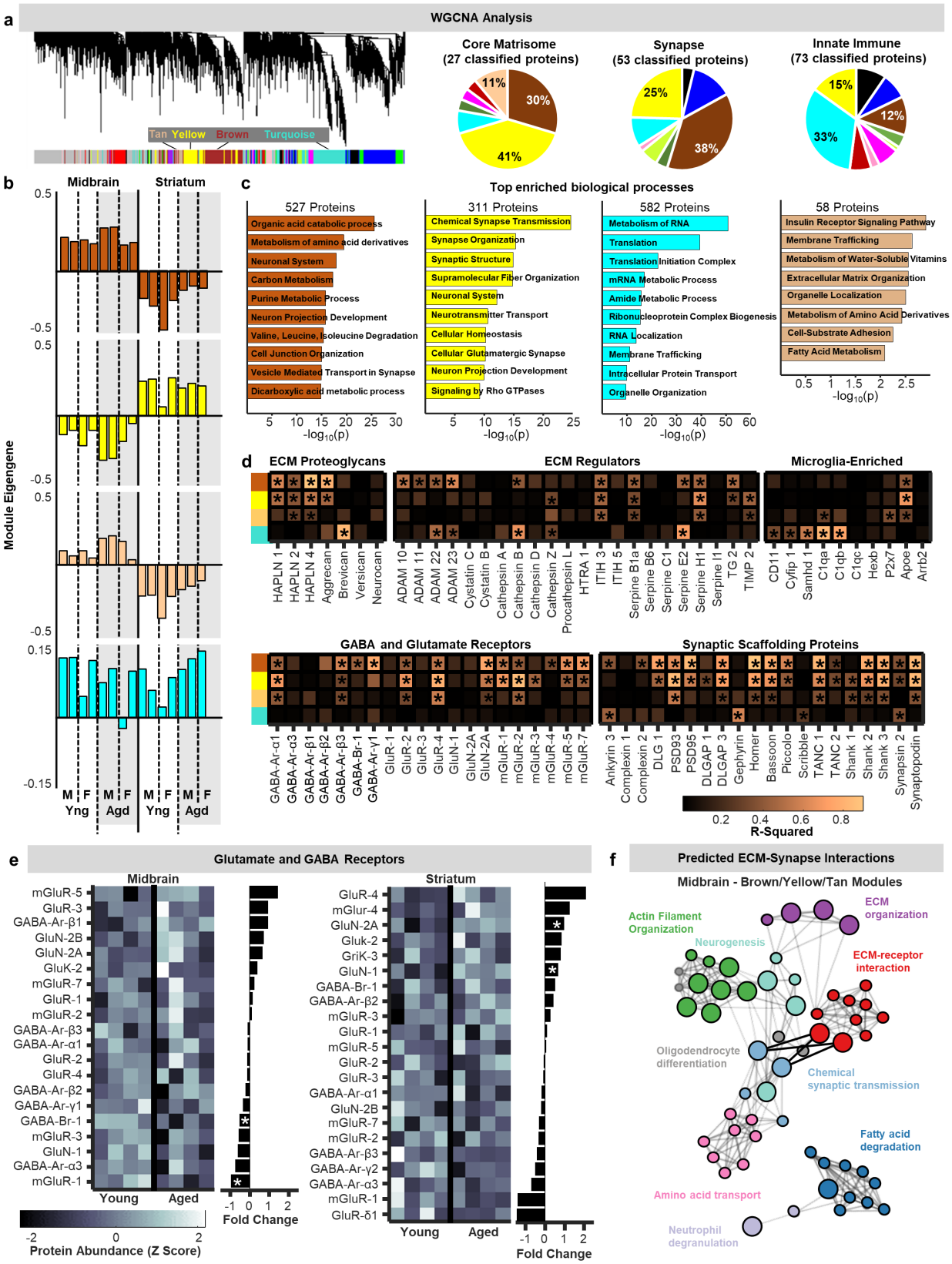
a
WGCNA Analysis
Tan Yellow Brown Turquoise
Core Matrisome (27 classified proteins)
30%
41%
11%
Synapse (53 classified proteins)
25%
38%
Innate Immune (73 classified proteins)
15%
12%
33%
b
Midbrain
Striatum
Module Eigengene
M F M F M F M F
Yng Agd Yng Agd
c
Top enriched biological processes
527 Proteins
Organic acid catabolic process
Metabolism of amino acid derivatives
Neuronal System
Carbon Metabolism
Purine Metabolic Process
Neuron Projection Development
Valine, Leucine, Isoleucine Degradation
Cell Junction Organization
Vesicle Mediated Transport in Synapse
Dicarboxylic acid metabolic process
311 Proteins
Chemical Synapse Transmission
Synapse Organization
Synaptic Structure
Supramolecular Fiber Organization
Neuronal System
Neurotransmitter Transport
Cellular Homeostasis
Cellular Glutamatergic Synapse
Neuron Projection Development
Signaling by Rho GTPases
582 Proteins
Metabolism of RNA
Translation
Translation Initiation Complex
mRNA Metabolic Process
Amide Metabolic Process
Ribonucleoprotein Complex Biogenesis
RNA Localization
Membrane Trafficking
Intracellular Protein Transport
Organelle Organization
58 Proteins
Insulin Receptor Signaling Pathway
Membrane Trafficking
Metabolism of Water-Soluble Vitamins
Extracellular Matrix Organization
Organelle Localization
Metabolism of Amino Acid Derivatives
Cell-Substrate Adhesion
Fatty Acid Metabolism
-log10(p)
d
ECM Proteoglycans
HAPLN 1 HAPLN 2 HAPLN 4 Aggrecan Brevican Versican Neurocan
ECM Regulators
ADAM 10 ADAM 11 ADAM 22 ADAM 23 Cystatin C Cystatin B Cathepsin A Cathepsin B Cathepsin D Cathepsin Z Procathepsin L HTRA 1 ITIH 3 ITIH 5 Serpine B1a Serpine B6 Serpine C1 Serpine E2 Serpine H1 Serpine I1 TG 2 TIMP 2
Microglia-Enriched
CD11 Cyfip 1 Samhd 1 C1qa C1qb C1qc Hexb P2x7 Apoe Arrb2
GABA and Glutamate Receptors
GABA-Ar-α1 GABA-Ar-α3 GABA-Ar-β1 GABA-Ar-β2 GABA-Ar-β3 GABA-Br-1 GABA-Ar-γ1 GluR-1 GluR-2 GluR-3 GluR-4 GluN-1 GluN-2A GluN-2A mGluR-1 mGluR-2 mGluR-3 mGluR-4 mGluR-5 mGluR-7
Synaptic Scaffolding Proteins
Ankyrin 3 Complexin 1 Complexin 2 DLG 1 PSD93 PSD95 DLGAP 1 DLGAP 3 Gephyrin Homer Bassoon Piccolo Scribble TANC 1 TANC 2 Shank 1 Shank 2 Shank 3 Synapsin 2 Synaptopodin
R-Squared
e
Glutamate and GABA Receptors
Midbrain
mGluR-5 GluR-3 GABA-Ar-β1 GluN-2B GluN-2A GluK-2 mGluR-7 GluR-1 mGluR-2 GABA-Ar-β3 GABA-Ar-α1 GluR-2 GluR-4 GABA-Ar-β2 GABA-Ar-γ1 GABA-Br-1 mGluR-3 GluN-1 GABA-Ar-α3 mGluR-1
Young Aged
Protein Abundance (Z Score)
Fold Change
Striatum
GluR-4 mGlur-4 GluN-2A Gluk-2 GriK-3 GluN-1 GABA-Br-1 GABA-Ar-β2 mGluR-3 GluR-1 mGluR-5 GluR-2 GluR-3 GABA-Ar-α1 GluN-2B mGluR-7 mGluR-2 GABA-Ar-β3 GABA-Ar-γ2 GABA-Ar-α3 mGluR-1 GluR-δ1
Young Aged
Fold Change
f
Predicted ECM-Synapse Interactions
Midbrain - Brown/Yellow/Tan Modules
ECM organization
Actin Filament Organization
Neurogenesis
ECM-receptor interaction
Oligodendrocyte differentiation
Chemical synaptic transmission
Fatty acid degradation
Amino acid transport
Neutrophil degranulation

1100 **Figure 2. a)** Left: dendrogram generated by Weighted Gene Coexpression Network Analysis
1101 (WGCNA) of all midbrain and striatal proteomic samples. Right: pie charts of classified core
1102 matrisome, synapse, and innate immune protein distributions across modules. **b)** Module
1103 eigengenes for the brown, yellow, tan, and turquoise modules for each sample. One aged
1104 female was classified as an outlier by the WGCNA and was removed from subsequent
1105 analyses. **c)** Enriched biological terms associated with brown, yellow, tan, and turquoise module
1106 proteins. **d)** Heatmaps representing correlations (r^2 values; linear regression) between brown,
1107 yellow, tan, and turquoise module eigengenes and abundances of specific extracellular matrix
1108 proteoglycans, complement proteins, GABAergic receptors, glutamatergic receptors, and
1109 synaptic scaffolding proteins. **e)** Heat maps of z-scored protein abundances and bar plots of
1110 corresponding fold-changes with age for all detected glutamate and GABA receptors (* $p < 0.05$;
1111 unpaired t-test). **f)** Network plots of process and pathway enrichment terms associated with all
1112 midbrain tan/yellow/brown module proteins whose abundances were modulated by age ($p <$
1113 0.05; Fisher's exact test).

1114

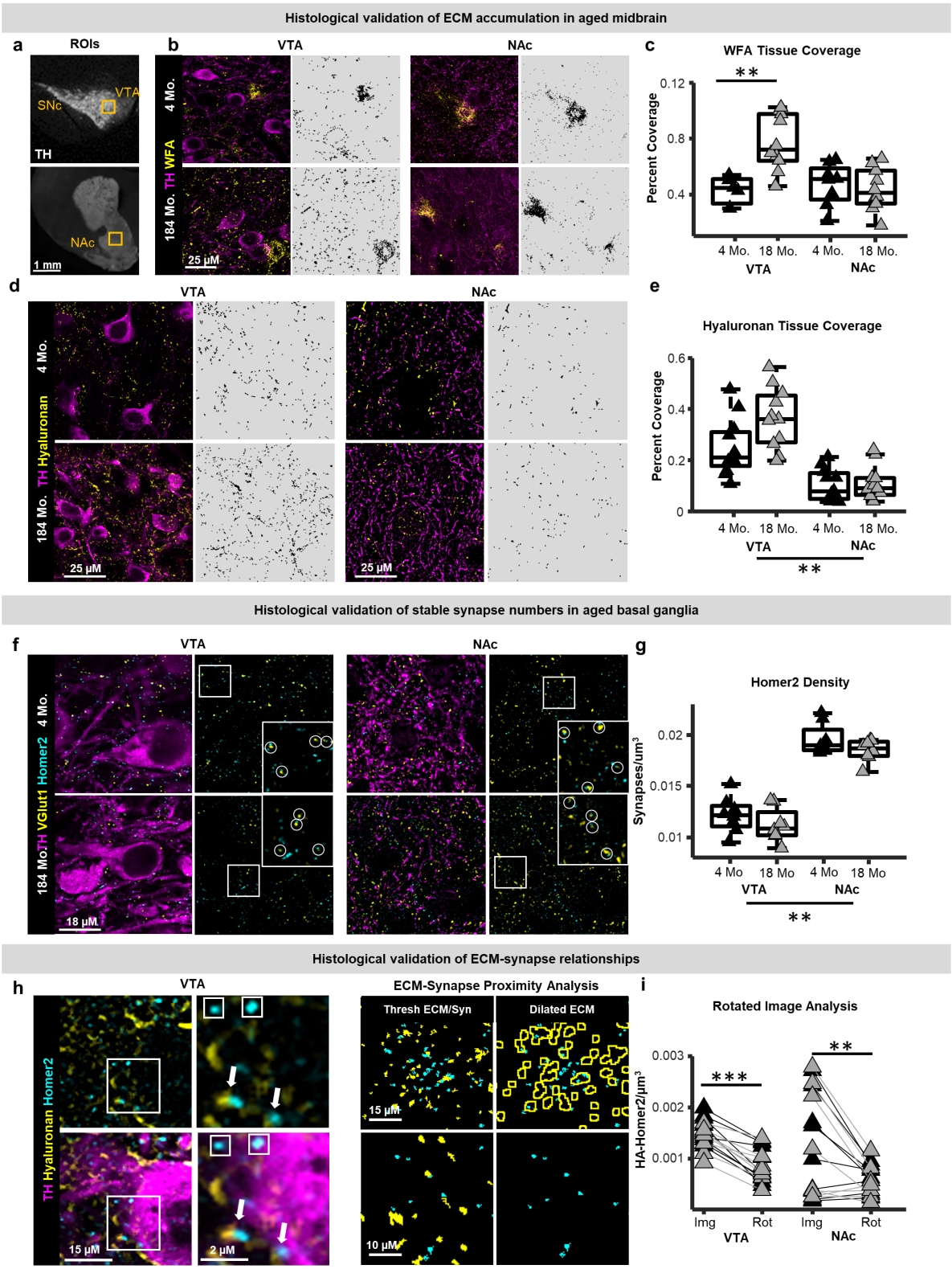
Histological validation of ECM accumulation in aged midbrain
a
ROIs
SNc
VTA
TH
NAc
1 mm
b
VTA
NAc
4 Mo.
184 Mo. TH WFA
25 µM
c
WFA Tissue Coverage
Percent Coverage
0.12
0.8
0.4
**
4 Mo.
18 Mo.
4 Mo.
18 Mo.
VTA
NAc
d
VTA
NAc
4 Mo.
184 Mo. TH Hyaluronan
25 µM
25 µM
e
Hyaluronan Tissue Coverage
Percent Coverage
0.6
0.4
0.2
0
4 Mo.
18 Mo.
4 Mo.
18 Mo.
VTA
NAc
**
Histological validation of stable synapse numbers in aged basal ganglia
f
VTA
NAc
4 Mo.
184 Mo.TH VGlut1 Homer2
18 µM
g
Homer2 Density
Synapses/um³
0.02
0.015
0.01
4 Mo
18 Mo
4 Mo
18 Mo
VTA
NAc
**
Histological validation of ECM-synapse relationships
h
VTA
TH Hyaluronan Homer2
15 µM
2 µM
ECM-Synapse Proximity Analysis
Thresh ECM/Syn
Dilated ECM
15 µM
10 µM
i
Rotated Image Analysis
HA-Homer2/µm³
0.003
0.002
0.001
***
**
Img
Rot
Img
Rot
VTA
NAc

1115

1116

1117 **Figure 3. a)** Histological validation of proteomic analysis of extracellular matrix (ECM) proteins
1118 was obtained from the ventral tegmental area (VTA; midbrain) and nucleus accumbens (NAc;
1119 striatum). **b)** Example photomicrographs of histochemically labelled tyrosine hydroxilase (TH)
1120 and Wisteria floribunda agglutinin (WFA) from a young-adult (4 months) and late-middle-aged
1121 (18 months) mouse (left panels). The right panels depict binarized images of the WFA matrix
1122 used for quantification. **c)** Boxplots depicting the proportion of a field of view occupied by WFA
1123 in the VTA and NAc of young-adult (black) and late-middle-aged (grey) mice. WFA tissue
1124 coverage was greater in the VTA of 18-month mice compared to young ($p < 0.01$; n-way
1125 ANOVA with post-hoc Tukey-Kramer) **d)** The ECM scaffold hyaluronan was analyzed in the
1126 same regions. The left panels show example photomicrographs of histochemically labelled
1127 hyaluronan and tyrosine hydroxylase in the VTA and NAc of a young-adult (4 months) and late-
1128 middle-aged (18 months) mouse (left panels). The right panels depict binarized images of the
1129 hyaluronan matrix used for quantification. **e)** Boxplots depicting the proportion of a field of view
1130 occupied by hyaluronan fibrils in the VTA and NAc of young-adult (black) and late-middle-aged
1131 (grey) mice. Hyaluronan tissue coverage was greater in the VTA compared to NAc ($p < 0.01$; n-
1132 way ANOVA), and on average greater in the VTA of late-middle-aged mice compared to young-
1133 adults ($p > 0.05$; post-hoc Tukey-Kramer). **f)** Example photomicrographs of
1134 immunohistochemically labelled Homer2 (excitatory postsynaptic puncta), VGlut1 (excitatory
1135 presynaptic puncta), and tyrosine hydroxylase in the VTA and NAc of young-adult and middle-
1136 aged wild-type mice. Inset images on the right depict the field of view outlined by the white
1137 squares within each image. Circles within the inset images delineate synapses with both a
1138 presynaptic and postsynaptic element. **g)** Homer2 densities were greater in the NAc compared
1139 to the VTA ($p < 0.01$; n-way ANOVA), but not different with age in either region. **h)** Left panels:
1140 example photomicrographs of histochemically labelled hyaluronan, homer2, and tyrosine
1141 hydroxylase in the VTA of a young-adult wild-type mouse. Images in the bottom panel are the
1142 same as in the top panel with the addition of the tyrosine hydroxylase channel. Zoomed in
1143 images are of the fields of view depicted by the white squares on the left images. Arrows
1144 highlight putative hyaluronan-homer2 colocalized puncta and small squares depict homer2
1145 puncta not associated with hyaluronan. Right panel: schematic ECM-synapse proximity analysis
1146 to identify synaptic puncta within <0.5 microns of ECM. **i)** Densities of homer2 within 0.5 μm of
1147 hyaluronan were significantly lower in images where 1 channel was rotated by 90 degrees in
1148 both the VTA ($p < 0.0001$; paired t-test) and NAc ($p < 0.01$; paired t-test).

1149

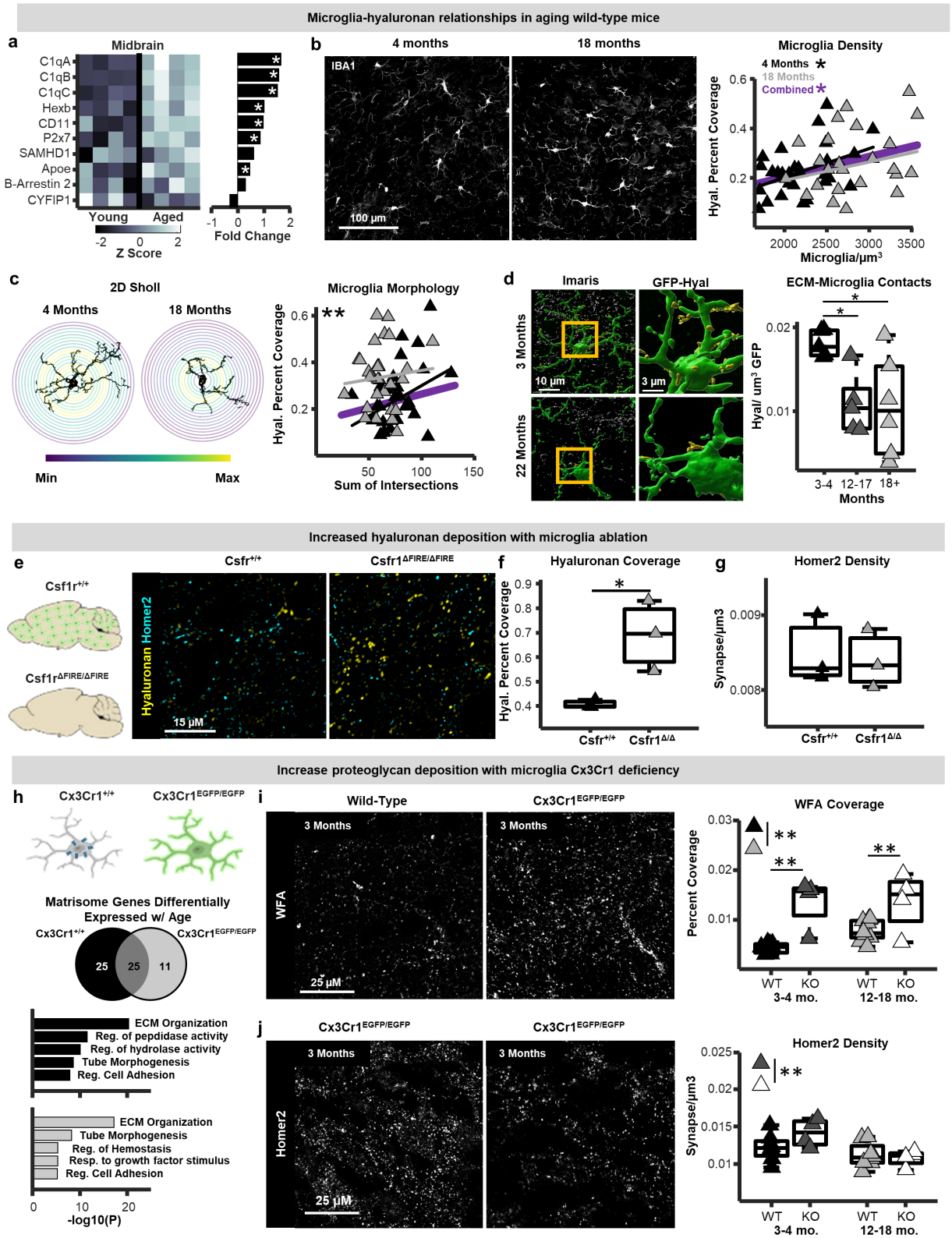
Microglia-hyaluronan relationships in aging wild-type mice
a
Midbrain
C1qA
C1qB
C1qC
Hexb
CD11
P2x7
SAMHD1
Apoe
B-Arrestin 2
CYFIP1
Young
Aged
Z Score
Fold Change
b
4 months
18 months
IBA1
100 µm
Microglia Density
4 Months
18 Months
Combined
Hyal. Percent Coverage
Microglia/µm3
c
2D Sholl
4 Months
18 Months
Min
Max
Microglia Morphology
Hyal. Percent Coverage
Sum of Intersections
d
Imaris
GFP-Hyal
3 Months
22 Months
10 µm
3 µm
ECM-Microglia Contacts
Hyal/ um3 GFP
3-4
12-17
18+
Months
Increased hyaluronan deposition with microglia ablation
e
Csf1r+/+
Csf1rΔFIRE/ΔFIRE
Csfr+/+
Csfr1ΔFIRE/ΔFIRE
Hyaluronan Homer2
15 µM
f
Hyaluronan Coverage
Hyal. Percent Coverage
Csfr+/+
Csfr1Δ/Δ
g
Homer2 Density
Synapse/µm3
Csfr+/+
Csfr1Δ/Δ
Increase proteoglycan deposition with microglia Cx3Cr1 deficiency
h
Cx3Cr1+/+
Cx3Cr1EGFP/EGFP
Matrisome Genes Differentially Expressed w/ Age
Cx3Cr1+/+
Cx3Cr1EGFP/EGFP
25
25
11
ECM Organization
Reg. of pepdidase activity
Reg. of hydrolase activity
Tube Morphogenesis
Reg. Cell Adhesion
ECM Organization
Tube Morphogenesis
Reg. of Hemostasis
Resp. to growth factor stimulus
Reg. Cell Adhesion
-log10(P)
i
Wild-Type
Cx3Cr1EGFP/EGFP
3 Months
WFA
25 µM
WFA Coverage
Percent Coverage
WT
KO
3-4 mo.
12-18 mo.
j
Cx3Cr1EGFP/EGFP
Homer2
25 µM
Homer2 Density
Synapse/µm3

1152 **Figure 4. a)** Heat maps of z-scored protein abundances and bar plots of corresponding fold-
1153 changes with age for all detected microglia-enriched proteins within the proteomic dataset from
1154 the young-adult and middle-aged midbrain (* $p < 0.05$; unpaired t-test). **b)** Left: example
1155 photomicrographs of IBA1-positive microglia in the ventral tegmental area (VTA) of young-adult
1156 (4 months) and late-middle-aged (18 months) wild-type mice. Right: scatter plots of the
1157 relationship between microglia densities and hyaluronan tissue coverage in the VTA. Microglia
1158 densities showed significant relationships with hyaluronan coverage in young-adult mice ($p <$
1159 0.05; robust regression) that were absent in middle-aged mice. **c)** Microglia morphological
1160 complexity was assessed in wild-type mice using a 2-dimensional Sholl analysis of IBA1-
1161 positive VTA microglia. Left: example binarized VTA microglia and Sholl radii from 4-month and
1162 18-month-old mice. Right: scatter plots of the relationship between microglia morphological
1163 complexities and hyaluronan tissue coverage in the VTA. Microglial complexities showed
1164 significant relationships with hyaluronan coverage in young-adult mice ($p < 0.01$; robust
1165 regression) that were absent in middle-aged mice. **e)** Hyaluronan matrix deposition and Homer2
1166 densities were assessed in young-adult (3 months) $Csf1r^{\Delta FIRE/\Delta FIRE}$ mice in which microglia are
1167 constitutively depleted, and $Csf1r^{+/+}$ control mice. **f)** Hyaluronan tissue coverage and **g)** Homer2
1168 puncta densities in the VTA of $Csf1r^{+/+}$ (black triangles) and $Csf1r^{\Delta FIRE/\Delta FIRE}$ (grey triangles) mice.
1169 Hyaluronan coverage was greater in $Csf1r^{\Delta FIRE/\Delta FIRE}$ mice compared to $Csf1r^{+/+}$ ($p < 0.05$;
1170 unpaired t-test), whereas Homer2 puncta densities were not different between genotypes. **h)**
1171 Top: ECM and synapse abundances were also examined in young-adult (3-4 months) and
1172 early-middle-aged (12-15 months) Cx3Cr1-knockout ($Cx3Cr1^{EGFP/EGFP}$) mice. Middle: pie chart of
1173 the number of differentially expressed matrisome-related genes between 12-month and 2-month
1174 wild-type and Cx3Cr1-knockout mice (from Gyoneva et al., 2019). Bottom: enriched biological
1175 pathways associated with differentially expressed matrisome genes with advanced age in wild-
1176 type and Cx3Cr1-knockout mice. **i)** Left: example photomicrographs of histochemically labelled
1177 Wisteria floribunda agglutinin (WFA; ECM) in the VTA of wild-type and Cx3Cr1-knockout mice.
1178 Right: Boxplots of WFA tissue coverage in wild type (black triangles; light grey triangles) and
1179 Cx3Cr1-knockout mice (dark grey triangles; white triangles). Cx3Cr1-knockout mice exhibited
1180 greater WFA matrix tissue coverage compared to wild type ($p < 0.001$; n-way ANOVA) and only
1181 wild-type mice exhibited age-related increases in WFA tissue coverage ($p < 0.05$; post-hoc
1182 Tukey-Kramer). **j)** Left: example photomicrographs of immunohistochemically labelled Homer2
1183 (postsynaptic) in the VTA of 3-month and 12-month-old Cx3Cr1-knockout mice. Right: boxplots
1184 of Homer2 puncta densities in wild-type and Cx3Cr1-knockout mice. Cx3Cr1-knockout mice
1185 exhibited a decrease in Homer2 densities with advanced age that the wild-type mice did not ($p <$
1186 0.05; n-way ANOVA with post-hoc Tukey-Kramer).

1187

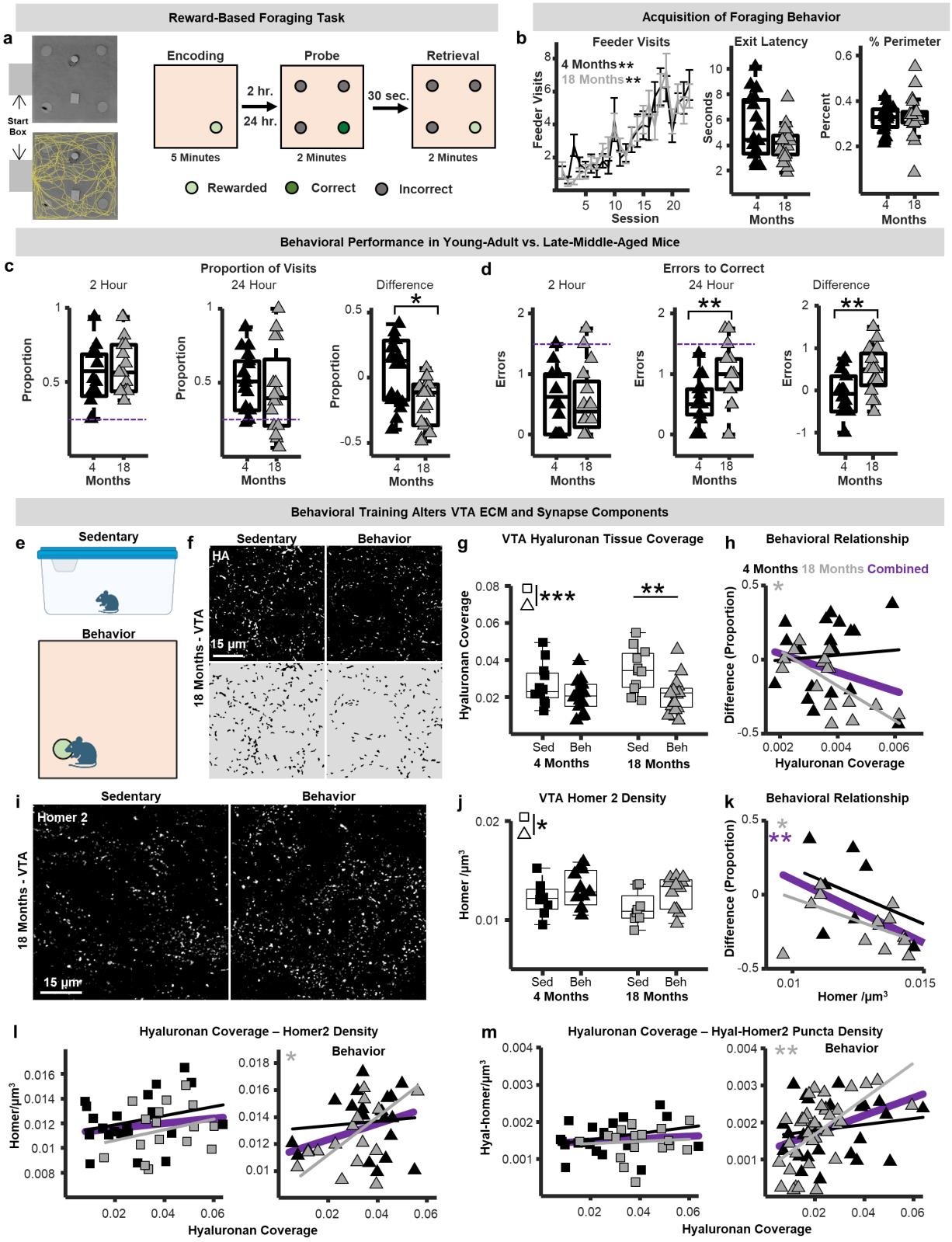
Reward-Based Foraging Task
a
Start Box
Encoding
Probe
Retrieval
2 hr.
24 hr.
30 sec.
5 Minutes
2 Minutes
2 Minutes
Rewarded
Correct
Incorrect
Acquisition of Foraging Behavior
b
Feeder Visits
4 Months**
18 Months**
Feeder Visits
Session
Exit Latency
Seconds
Months
% Perimeter
Percent
Months
Behavioral Performance in Young-Adult vs. Late-Middle-Aged Mice
c
Proportion of Visits
2 Hour
24 Hour
Difference
Proportion
Months
d
Errors to Correct
2 Hour
24 Hour
Difference
Errors
Months
Behavioral Training Alters VTA ECM and Synapse Components
e
Sedentary
Behavior
f
Sedentary
Behavior
HA
18 Months - VTA
15 µm
g
VTA Hyaluronan Tissue Coverage
Hyaluronan Coverage
Sed
Beh
4 Months
18 Months
h
Behavioral Relationship
4 Months 18 Months Combined
Difference (Proportion)
Hyaluronan Coverage
i
Sedentary
Behavior
Homer 2
18 Months - VTA
15 µm
j
VTA Homer 2 Density
Homer /µm³
Sed
Beh
4 Months
18 Months
k
Behavioral Relationship
Difference (Proportion)
Homer /µm³
l
Hyaluronan Coverage – Homer2 Density
Behavior
Homer/µm³
Hyaluronan Coverage
m
Hyaluronan Coverage – Hyal-Homer2 Puncta Density
Behavior
Hyal-homer/µm³
Hyaluronan Coverage

Figure 5. a) Left: schematic depicting the foraging arena with proximal (fixed objects within arena) reference landmarks, a start box equipped with a guillotine door, and overhead tracking of mouse behavior (yellow). Right: schematic depiction of the test phase of the reward-based foraging paradigm. **b)** Right: the number of feeder visits increased across sessions in both young-adult (4 months; black) and late-middle-aged (18 months; grey) mice ($p < 0.01$; repeated measures ANOVA). The latency to exit the start box (middle), and the proportion of time on the perimeter of the arena (right) were not different between age groups. **c)** The proportion of correct feeder visits during probe trials at 2- and 24-hour delays (left and middle), and the within-subject difference measure (24 hour-2 hour; right). Middle-aged mice made significantly fewer correct feeder visits at 24 hours compared to 2 hours ($p < 0.05$; n-way ANOVA), whereas the performance of the young-adult mice was similar between the two conditions. **d)** The number of errors to correct feeder visits during probe trials at 2- and 24-hour delays (left and middle), and the within subject difference measure (24 hr.-2 hr.). Middle-aged mice made more errors at the 24-hour condition compared to young ($p < 0.01$; unpaired t-test) and made significantly more errors at 24 hours compared to 2 hours. ($p < 0.01$; n-way ANOVA). **e)** Hyaluronan and Homer2 were assessed in the VTA of young-adult (4 months) and late-middle-aged (18 months) behavior-trained mice and sedentary controls. **f)** Top: example photomicrographs of histochemically labelled hyaluronan from a sedentary and behavior-trained 18-month-old mouse. Bottom: binarized images of the hyaluronan matrix used for quantification. **g)** Boxplots depicting VTA hyaluronan tissue coverage in young-adult (black) sedentary (squares) and behavior-trained (triangles) mice and late-middle-aged (grey) sedentary and behavior-trained mice. Behavior-trained mice exhibited lower hyaluronan coverage relative to controls ($p < 0.001$; n-way ANOVA), and behavior-trained middle-aged mice had lower hyaluronan levels relative to sedentary ($p < 0.01$; post-hoc Tukey-Kramer). **h)** Relationship between VTA hyaluronan coverage and performance on reward-based foraging task (proportion of correct feeder visits difference measure). A significant negative relationship was observed in middle-aged mice ($p < 0.05$; robust regression). **i)** Example photomicrographs of immunolabelled Homer2 from a sedentary and behavior-trained 18-month-old mouse. **j)** Boxplots of VTA Homer2 densities in young-adult sedentary and behavior-trained mice and late-middle-aged sedentary and behavior-trained mice. Behavior-trained mice exhibited higher Homer2 densities relative to controls ($p < 0.05$; n-way ANOVA). **k)** Relationship between VTA Homer2 densities and performance on reward-based foraging task. Significant negative relationships were observed across all mice (purple; $p < 0.01$; robust regression) and in middle-aged mice ($p < 0.05$; robust regression). **l)** Scatter plots of the relationship between hyaluronan tissue coverage and Homer2 puncta densities in young-adult and late-middle-aged sedentary and behavior-trained mice. A significant positive correlation was observed only in middle-aged behavior-trained mice (robust regression; $r = 0.48$; $p < 0.05$). **m)** Scatter plots of the relationship between hyaluronan tissue coverage and densities of Homer2 within 0.5 µm of hyaluronan fibrils in young-adult and late-middle-aged sedentary and behavior-trained mice. Again, a significant positive correlation was observed only in middle-aged behavior-trained mice (robust regression; $r = 0.59$; $p < 0.01$).

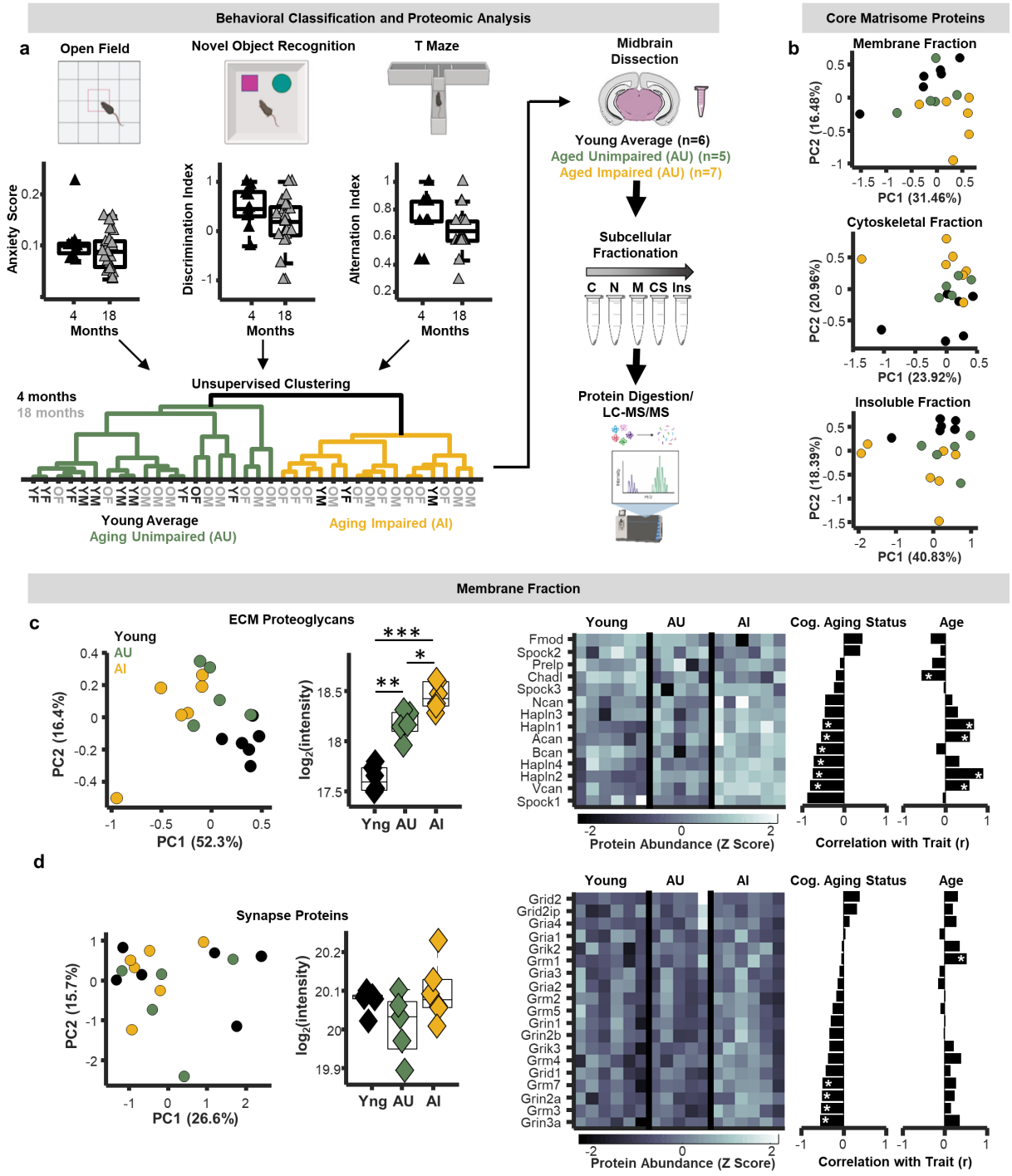
Behavioral Classification and Proteomic Analysis
a
Open Field
Novel Object Recognition
T Maze
Anxiety Score
Discrimination Index
Alternation Index
Months
Unsupervised Clustering
4 months
18 months
Young Average
Aging Unimpaired (AU)
Aging Impaired (AI)
Midbrain Dissection
Young Average (n=6)
Aged Unimpaired (AU) (n=5)
Aged Impaired (AU) (n=7)
Subcellular Fractionation
C N M CS Ins
Protein Digestion/ LC-MS/MS
Core Matrisome Proteins
b
Membrane Fraction
PC2 (16.48%)
PC1 (31.46%)
Cytoskeletal Fraction
PC2 (20.96%)
PC1 (23.92%)
Insoluble Fraction
PC2 (18.39%)
PC1 (40.83%)
Membrane Fraction
c
ECM Proteoglycans
Young
AU
AI
PC2 (16.4%)
PC1 (52.3%)
log2(intensity)
Yng AU AI
Fmod
Spock2
Prelp
Chadl
Spock3
Ncan
Hapln3
Hapln1
Acan
Bcan
Hapln4
Hapln2
Vcan
Spock1
Young AU AI
Cog. Aging Status
Age
Protein Abundance (Z Score)
Correlation with Trait (r)
d
Synapse Proteins
PC2 (15.7%)
PC1 (26.6%)
log2(intensity)
Yng AU AI
Grid2
Grid2ip
Gria4
Gria1
Grik2
Grm1
Gria3
Gria2
Grm2
Grm5
Grin1
Grin2b
Grik3
Grm4
Grid1
Grm7
Grin2a
Grm3
Grin3a
Young AU AI
Cog. Aging Status
Age
Protein Abundance (Z Score)
Correlation with Trait (r)

1232

1233

1234 **Figure 6. a)** Schematic behavioral classification and proteomic analysis. Young-adult (4
1235 months; n = 12; black triangles) and late-middle-aged (18 months; n = 24; grey triangles) male
1236 and female mice were tested on an open field, a novel object recognition test, and a T Maze
1237 task. Data from all 3 behaviors were used to perform hierarchical clustering analyses to
1238 delineate young average (black), aging unimpaired (AU; green), and aging impaired (AI; yellow)
1239 mice. Midbrains from these mice were dissected, and tissue underwent subcellular fractionation
1240 followed by proteomic analysis. **b)** PCA plots of all core matrisome proteins from membrane,
1241 cytoskeletal, and insoluble fractions. **c**) PCA plot of extracellular matrix proteoglycans from the
1242 membrane fraction (left). Average protein intensities of extracellular matrix proteoglycans in the
1243 membrane fraction separated by age and cognitive status (middle). Aging mice exhibited higher
1244 proteoglycan abundances ($p < 0.001$; n-Way ANOVA), and the aging impaired mice showed
1245 higher proteoglycan abundances compared to aging unimpaired mice ($p < 0.05$; post-hoc
1246 Tukey-Kramer). Right: heat plot of extracellular matrix proteoglycans abundances in the
1247 membrane fraction and bar plots of their relationship with cognitive status and age (* $p < 0.05$;
1248 linear probability model). **d**) PCA plot of synapse proteins from the membrane fraction (left).
1249 Average protein intensities of synapse proteins in the membrane fraction separated by age and
1250 cognitive status (middle). Right: heat plot of glutamate receptor abundances and bar plots of
1251 their relationship with cognitive status and age (* $p < 0.05$; linear probability model).

1252

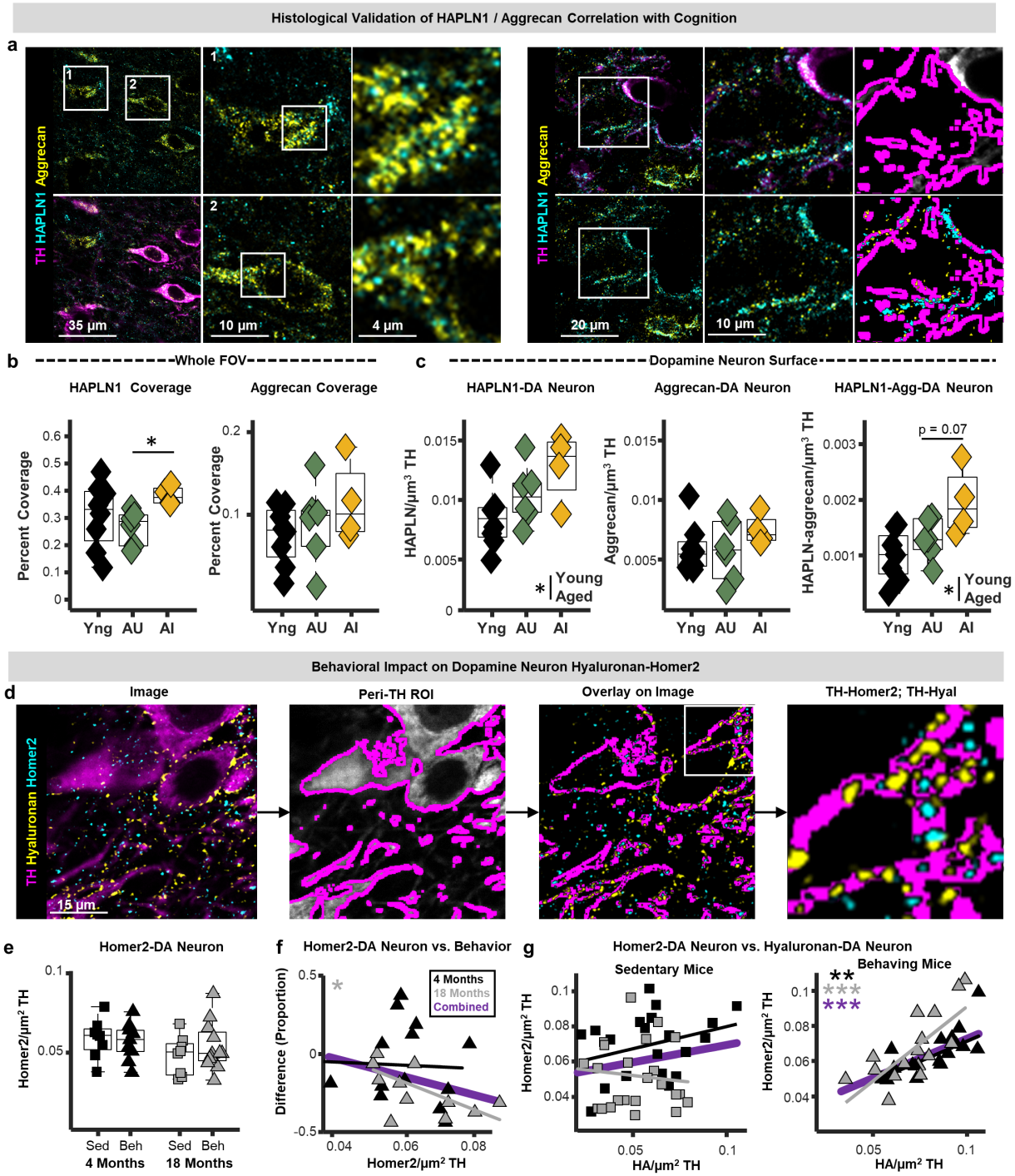
Histological Validation of HAPLN1 / Aggrecan Correlation with Cognition
a
TH HAPLN1 Aggrecan
35 µm
10 µm
4 µm
20 µm
10 µm
b
Whole FOV
HAPLN1 Coverage
Aggrecan Coverage
Percent Coverage
Yng AU AI
c
Dopamine Neuron Surface
HAPLN1-DA Neuron
Aggrecan-DA Neuron
HAPLN1-Agg-DA Neuron
HAPLN/µm³ TH
Aggrecan/µm³ TH
HAPLN-aggrecan/µm³ TH
p = 0.07
Young
Aged
Behavioral Impact on Dopamine Neuron Hyaluronan-Homer2
d
Image
Peri-TH ROI
Overlay on Image
TH-Homer2; TH-Hyal
TH Hyaluronan Homer2
15 µm
e
Homer2-DA Neuron
Homer2/µm² TH
Sed Beh Sed Beh
4 Months 18 Months
f
Homer2-DA Neuron vs. Behavior
Difference (Proportion)
4 Months
18 Months
Combined
Homer2/µm² TH
g
Homer2-DA Neuron vs. Hyaluronan-DA Neuron
Sedentary Mice
Behaving Mice
Homer2/µm² TH
HA/µm² TH

1253

1254

1255 **Figure 7. a)** Left: example photomicrographs of immunohistochemically labelled hyaluronan and
1256 proteoglycan link protein 1 (HAPLN1), aggrecan, and tyrosine hydroxylase (TH) from the VTA of
1257 a late-middle aged mouse. Numbered images in the middle panel correspond to the numbered
1258 fields of view depicted by the white squares on the left. The right panels depict the fields of view
1259 depicted by the white squares in the middle panel. Right: example photomicrographs depicting
1260 HAPLN1 and aggrecan deposition on dopamine neuron surfaces, as well as the peri-dopamine
1261 neuron region of interest used to estimate the abundance of each protein at neuronal
1262 membranes in the VTA. **b)** Boxplots depicting field of view coverage of HAPLN1 and aggrecan
1263 in the VTA of young (black), aging unimpaired (AU; green), and aging impaired (AI; yellow)
1264 mice. AI mice exhibited significantly higher HAPLN1 coverage compared to AU mice ($p < 0.05$;
1265 n-way ANOVA with post-hoc t-test). **c)** Boxplots depicting HAPLN1-DA neuron, aggrecan-DA
1266 neuron, and HAPLN1-aggrecan-DA neuron puncta densities in the VTA of young, aging
1267 unimpaired (AU), and aging impaired (AI) mice. HAPLN1-DA neuron and HAPLN1-aggrecan-DA
1268 neuron densities increased with age ($p < 0.05$; 2-way ANOVA)**.** AI mice tended to show higher
1269 HAPLN1-DA neuron and HAPLN1-aggrecan-DA neuron puncta densities compared to AU mice
1270 ($p = 0.07$; post-hoc Tukey-Kramer). **d)** Schematic of the analysis strategy used to examine
1271 hyaluronan and Homer2 on tyrosine-hydroxylase expressing dopamine neurons (Homer-DA
1272 neuron). **e)** Boxplots depicting homer-DA neuron puncta densities in young-adult (black)
1273 sedentary (squares) and behavior-trained (triangles) mice and late-middle-aged (grey)
1274 sedentary and behavior-trained mice. **f)** Relationship between homer-DA neuron puncta
1275 densities and performance on reward-based foraging task. A significant negative relationship
1276 was observed in middle-aged mice ($p < 0.05$; robust regression). **g)** Scatter plots of hyaluronan-
1277 DA neuron puncta densities plotted against Homer2-DA neuron puncta densities in sedentary
1278 and behavior-trained mice. No significant relationships were observed in sedentary mice, but
1279 significant positive relationships were seen in behavior-trained at both ages (young: $p < 0.01$;
1280 middle-aged: $p < 0.01$; all: $p < 0.001$ robust regression).

1281

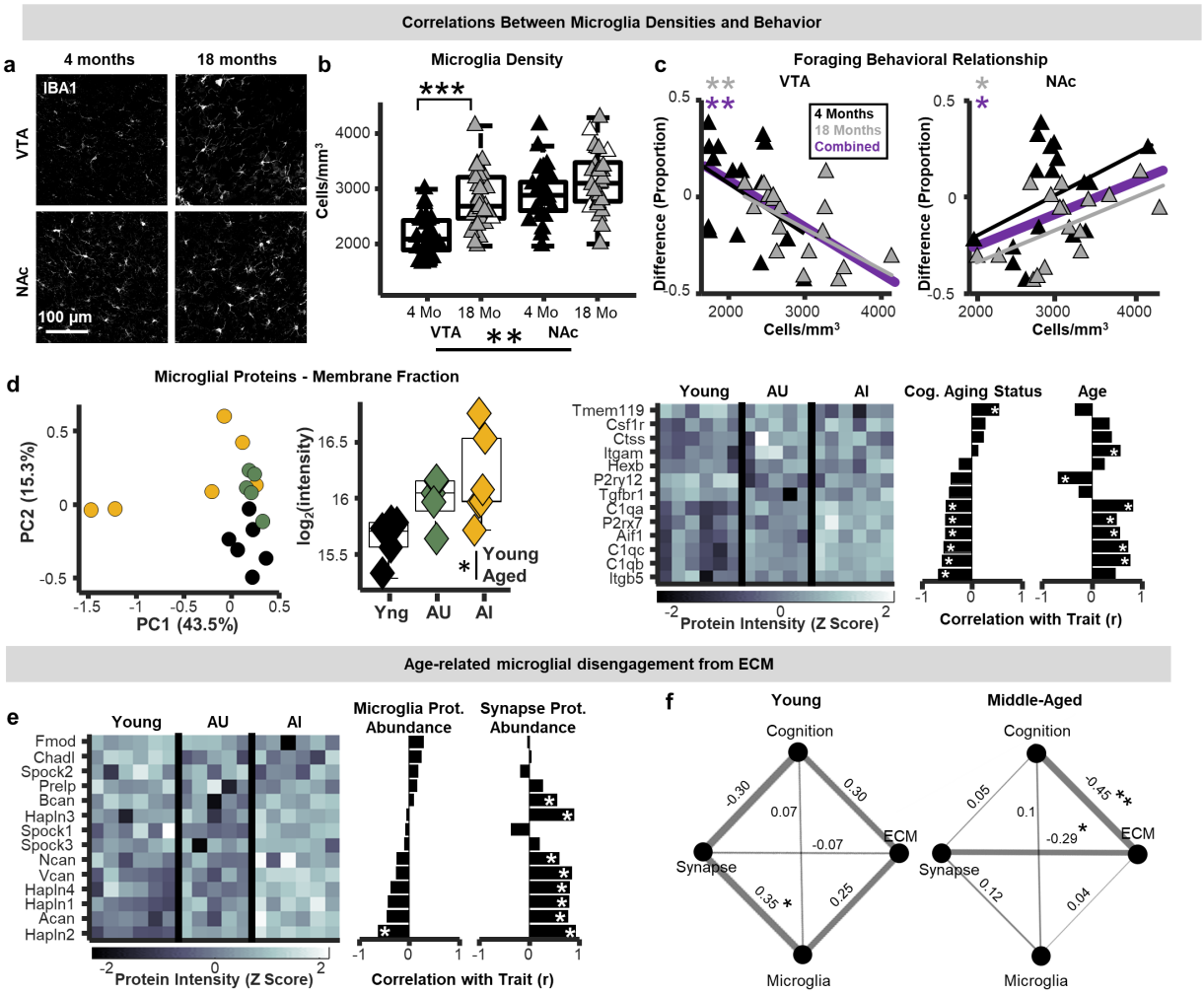
Correlations Between Microglia Densities and Behavior
a
4 months
18 months
IBA1
VTA
NAc
100 µm
b
Microglia Density
Cells/mm³
4 Mo
18 Mo
VTA
NAc
c
Foraging Behavioral Relationship
VTA
NAc
4 Months
18 Months
Combined
Difference (Proportion)
Cells/mm³
d
Microglial Proteins - Membrane Fraction
PC2 (15.3%)
PC1 (43.5%)
log2(intensity)
Young
Aged
Yng
AU
AI
Tmem119
Csf1r
Ctss
Itgam
Hexb
P2ry12
Tgfbr1
C1qa
P2rx7
Aif1
C1qc
C1qb
Itgb5
Cog. Aging Status
Age
Protein Intensity (Z Score)
Correlation with Trait (r)
Age-related microglial disengagement from ECM
e
Fmod
Chadl
Spock2
Prelp
Bcan
Hapln3
Spock1
Spock3
Ncan
Vcan
Hapln4
Hapln1
Acan
Hapln2
Microglia Prot. Abundance
Synapse Prot. Abundance
f
Young
Middle-Aged
Cognition
Synapse
ECM
Microglia
-0.30
0.30
0.07
-0.07
0.35
0.25
0.05
-0.45
0.1
-0.29
0.12
0.04

1282

1283

1284 **Figure 8. a)** IBA1-positive microglia in the ventral tegmental area (VTA) and nucleus
1285 accumbens (NAc) of behavior-trained mice. **b)** VTA and NAc microglia densities in young-adult
1286 (black) and middle-aged (grey) mice. Greater microglia densities were observed in the NAc
1287 compared to VTA ($p < 0.01$; n-way ANOVA), and in the VTA, microglia densities were greater in
1288 middle-aged mice ($p < 0.0001$; post-hoc Tukey-Kramer). **c)** Relationship between VTA and NAc
1289 microglia densities and performance on reward-based foraging task. In the VTA, significant
1290 negative relationships were observed across all mice (purple; $p < 0.01$; robust regression) and
1291 in middle-aged mice (grey; $p < 0.01$; robust regression), whereas in the NAc, significant positive
1292 relationships were observed (all: $p < 0.05$; middle-aged: $p < 0.05$, robust regression). **d)** PCA
1293 plot of select microglia-enriched proteins from the membrane fraction (left). Average protein
1294 intensities of microglia-enriched proteins separated by age and cognitive status (middle).
1295 Microglia-enriched proteins were significantly more abundant in the aged midbrain compared to
1296 young ($p < 0.05$; n-way ANOVA). Heat plot of microglia-enriched protein abundances and bar
1297 plots of their relationship with cognitive status and age (* $p < 0.05$; linear probability model). **e)**
1298 Heat plot of ECM proteoglycan abundances from the membrane fraction and bar plots of their
1299 relationship with total microglia-enriched protein and synapse receptor abundances (* $p < 0.05$;
1300 linear probability model). **f)** Correlation network plots of relationships between cognition and
1301 ECM, synapse, and microglia abundances from both behavioral experiments in this study
1302 shown separately for young-aged and middle-aged mice. Numbers are r values and the width of
1303 connections between variables scales with the strength of their correlation (* $p < 0.05$; ** $p <$
1304 0.01; linear regression).

1305

Extended Data Figures and Figure Legends

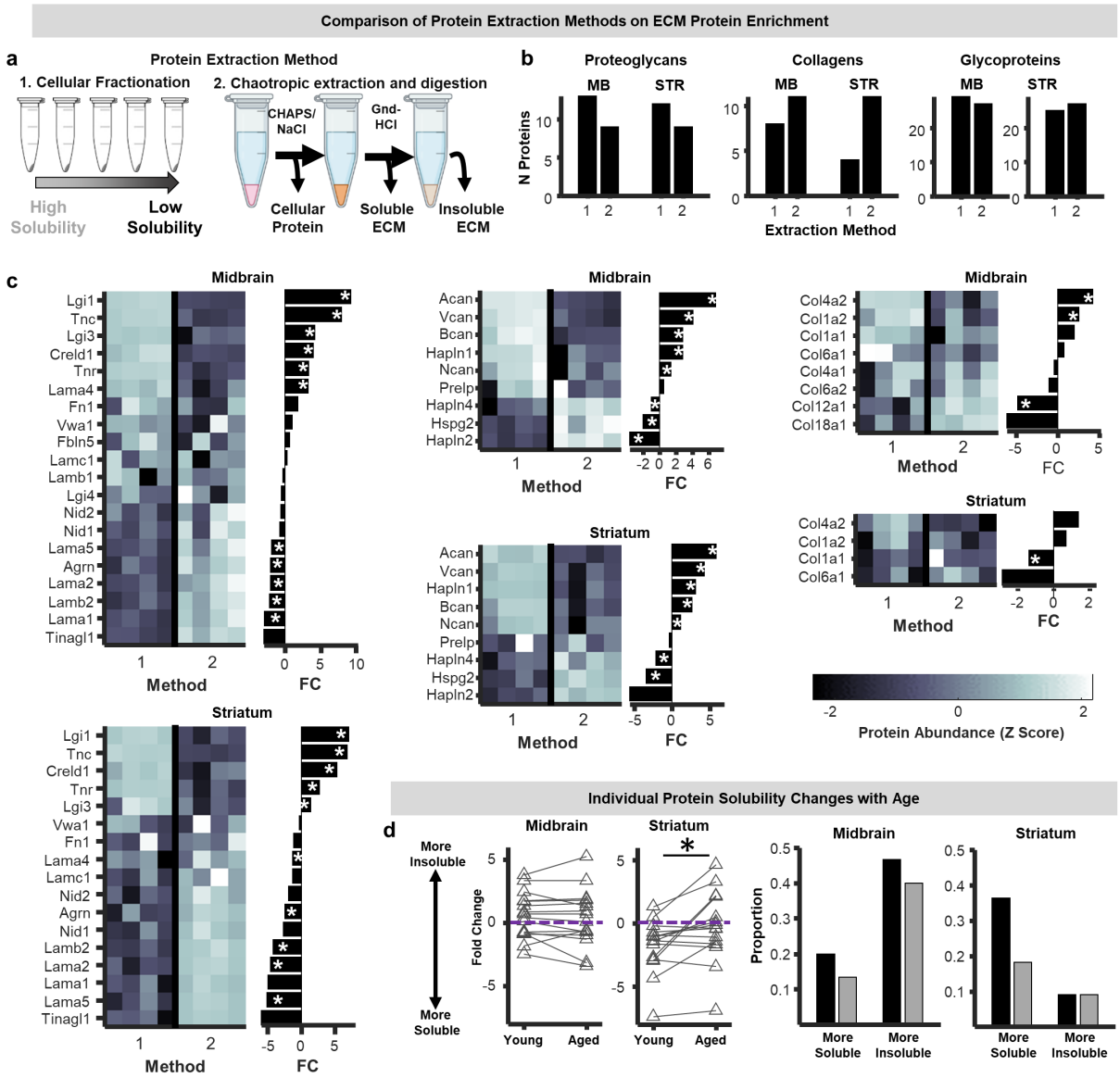

1308 **Extended Data Figure 1**. **a)** To compare distinct ECM protein enrichment strategies, the
1309 midbrain and striatum of young-adult (3 months) mice were dissected and underwent either 1:
1310 solubility-based subcellular fractionation (n=4) or 2: chaotropic extraction and digestion (n = 4)
1311 or protocols. **b)** Comparison of the number of core matrisome proteins detected using each
1312 approach. Extraction method 1 refers to solubility-based fractionation and extraction method 2
1313 refers to chaotropic extraction and digestion **c)** Heat maps of protein abundances (z scored) and
1314 bar plots of corresponding fold-changes with age for ECM glycoproteins, proteoglycans,
1315 collagens, and ECM regulators detected using the two approaches. (* $p < 0.05$ - unpaired t-
1316 test). **d)** Left: Paired plots of fold changes of individual matrisome proteins detected in the
1317 insoluble fraction that were detected in at least one of the subcellular/soluble fractions using the
1318 fractionation approach for young and aged mice. Fold-changes were calculated with respect to
1319 the insoluble fraction. There was a significant shift towards greater insolubility in the aged
1320 striatum ($p < 0.05$; paired t-test). Purple lines denote a fold change of 0, indicating no difference
1321 in abundance between insoluble and soluble fractions. Right: bar plot showing the proportion of
1322 matrisome proteins showing differences in solubility (upregulated and downregulated shown
1323 separately) in the young and aged mice.

1324

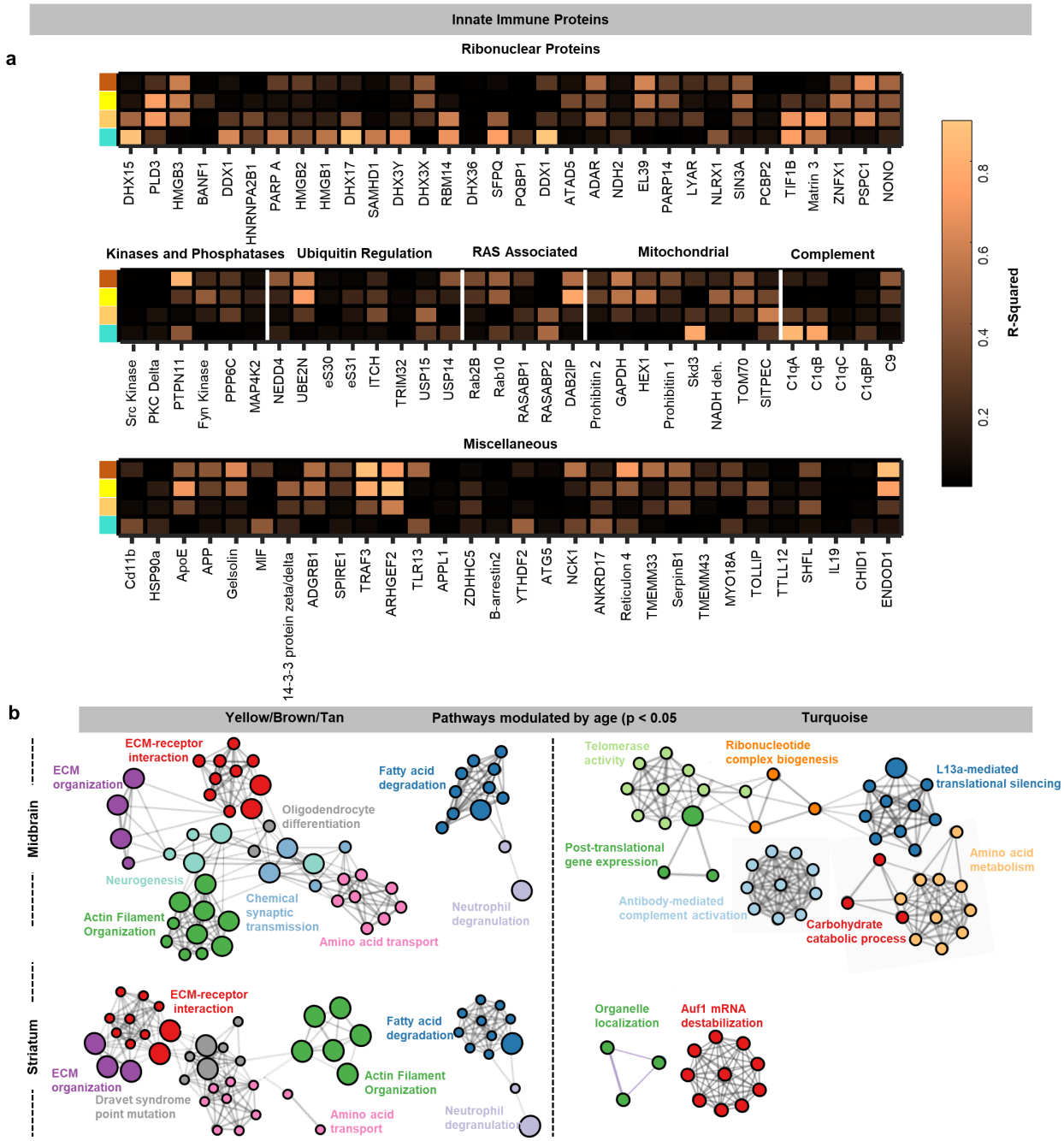
a
Innate Immune Proteins
Ribonuclear Proteins
DHX15
PLD3
HMGB3
BANF1
DDX1
HNRNPA2B1
PARP A
HMGB2
HMGB1
DHX17
SAMHD1
DHX3Y
DHX3X
RBM14
DHX36
SFPQ
PQBP1
DDX1
ATAD5
ADAR
NDH2
EL39
PARP14
LYAR
NLRX1
SIN3A
PCBP2
TIF1B
Matrin 3
ZNFX1
PSPC1
NONO
Kinases and Phosphatases
Ubiquitin Regulation
RAS Associated
Mitochondrial
Complement
Src Kinase
PKC Delta
PTPN11
Fyn Kinase
PPP6C
MAP4K2
NEDD4
UBE2N
eS30
eS31
ITCH
TRIM32
USP15
USP14
Rab2B
Rab10
RASABP1
RASABP2
DAB2IP
Prohibitin 2
GAPDH
HEX1
Prohibitin 1
Skd3
NADH deh.
TOM70
SITPEC
C1qA
C1qB
C1qC
C1qBP
C9
Miscellaneous
Cd11b
HSP90a
ApoE
APP
Gelsolin
MIF
14-3-3 protein zeta/delta
ADGRB1
SPIRE1
TRAF3
ARHGEF2
TLR13
APPL1
ZDHHC5
B-arrestin2
YTHDF2
ATG5
NCK1
ANKRD17
Reticulon 4
TMEMM33
SerpinB1
TMEMM43
MYO18A
TOLLIP
TTLL12
SHFL
IL19
CHID1
ENDOD1
R-Squared
0.2
0.4
0.6
0.8
b
Yellow/Brown/Tan
Pathways modulated by age (p < 0.05
Turquoise
Midbrain
ECM-receptor interaction
ECM organization
Fatty acid degradation
Oligodendrocyte differentiation
Neurogenesis
Chemical synaptic transmission
Actin Filament Organization
Amino acid transport
Neutrophil degranulation
Striatum
ECM-receptor interaction
Fatty acid degradation
ECM organization
Actin Filament Organization
Dravet syndrome point mutation
Amino acid transport
Neutrophil degranulation
Telomerase activity
Ribonucleotide complex biogenesis
L13a-mediated translational silencing
Post-translational gene expression
Amino acid metabolism
Antibody-mediated complement activation
Carbohydrate catabolic process
Organelle localization
Auf1 mRNA destabilization

1325

1326

1327 **Extended Data Figure 2**. **a)** Heatmaps representing correlations (r-squared values) between
1328 brown, yellow, tan, and turquoise module eigengenes and abundances of specific innate
1329 immune proteins separated by functional classification (ribonuclear proteins, kinases and
1330 phosphatases, ubiquitin-associated proteins, mitochondrial proteins, complement proteins, and
1331 other miscellaneous innate immune proteins). **b)** Network plots of process and pathway
1332 enrichment terms associated with all tan/yellow/brown module (left) and turquoise module (right)
1333 proteins whose abundances were modulated by age ($p < 0.05$) in the midbrain and striatum.

1334

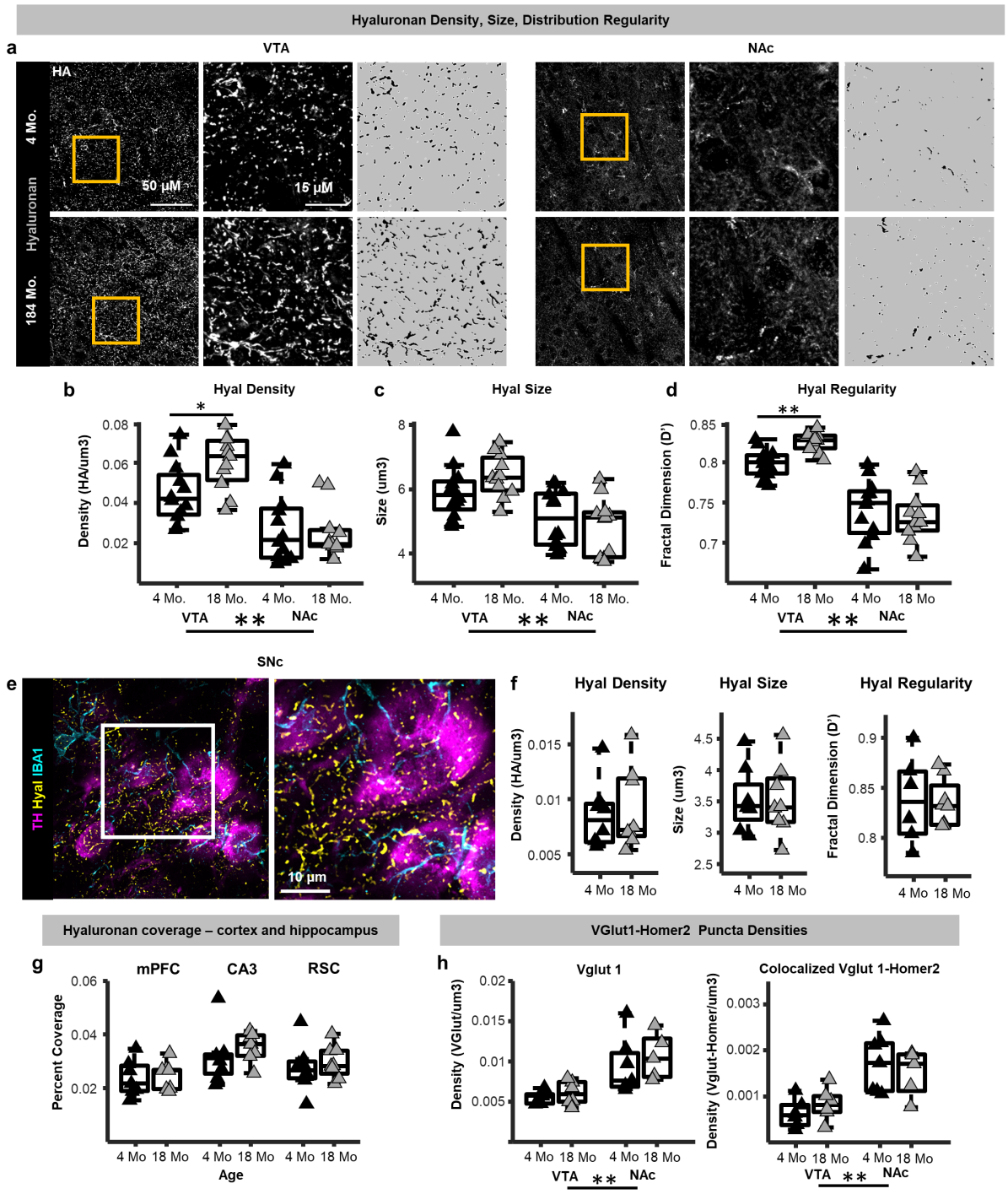
Hyaluronan Density, Size, Distribution Regularity
a
VTA
NAc
HA
4 Mo.
184 Mo.
Hyaluronan
50 µM
15 µM
b
Hyal Density
Density (HA/um3)
c
Hyal Size
Size (um3)
d
Hyal Regularity
Fractal Dimension (D')
4 Mo.
18 Mo.
VTA
NAc
SNc
e
TH Hyal IBA1
10 µm
f
Hyal Density
Hyal Size
Hyal Regularity
4 Mo
18 Mo
Hyaluronan coverage – cortex and hippocampus
g
mPFC
CA3
RSC
Percent Coverage
Age
VGlut1-Homer2 Puncta Densities
h
Vglut 1
Colocalized Vglut 1-Homer2
Density (VGlut/um3)
Density (Vglut-Homer/um3)

1335

1336

1337 **Extended Data Figure 3**. **a)** The ECM scaffold hyaluronan (Hyal) was analyzed in two critical
1338 regions of the mesolimbic dopamine system, the ventral tegmental area (VTA) and nucleus
1339 accumbens (NAc). **b)** Example photomicrographs of histochemically labelled hyaluronan in the
1340 VTA and NAc of a young-adult (4 months) and late-middle-aged (18 months) mouse (left
1341 panels). Middle panels show zoomed in images of the areas within the yellow squares in the left
1342 panels. The right panels depict binarized images of the hyaluronan matrix used for
1343 quantification. **c-e)** Boxplots depicting **c)** hyaluronan fibril densities, **d)** median hyaluronan fibril
1344 sizes, and **e)** hyaluronan distribution regularity (Fractal Dimension plugin – Fiji) in the VTA and
1345 NAc of young-adult (black) and late-middle-aged (grey) mice. Higher fractal dimension values
1346 (D') indicate more spatial regularity of the hyaluronan matrix. Hyaluronan fibril density, median
1347 size, and distribution regularity were greater in the VTA compared to NAc (Density: $p < 0.001$;
1348 Size: $p < 0.001$; Regularity: $p < 0.001$; n-way ANOVA). Late-middle-aged mice exhibited
1349 significantly greater VTA hyaluronan fibril density ($p < 0.05$; post hoc t-test) and distribution
1350 regularity ($p < 0.01$; post-hoc t-test). **e)** Example photomicrograpghs of histochemically labelled
1351 hyaluronan, tyrosine hydroxylase (TH)-positive dopaminergic neurons, and IBA1-positive
1352 microglia in the substantia nigra pars compacta (SNc). **f**) SNc hyaluronan fibril densities, sizes,
1353 and distribution regularity were not different between young-adult (4 months) and late-middle-
1354 aged mice (18 months). **g)** Hyaluronan fibril field of view coverage in the mPFC, CA3 region of
1355 the hippocampus, and retrosplenial cortex (RSC) of young-adult (4 months) and late-middle-
1356 aged mice (18 months). **h)** Left: densities of VGlut1 puncta in the VTA and NAc of young-adult
1357 and middle-aged mice. There was a greater density of VGlut1 in the NAc compared to VTA ($p <$
1358 0.01; n-way ANOVA). Right: densities of VGlut1-homer2 colocalized puncta in the VTA and NAc
1359 of young-adult and middle-aged mice. There was a greater density of VGlut1-homer2
1360 colocalized puncta in the NAc compared to VTA ($p < 0.01$; n-way ANOVA).

1361

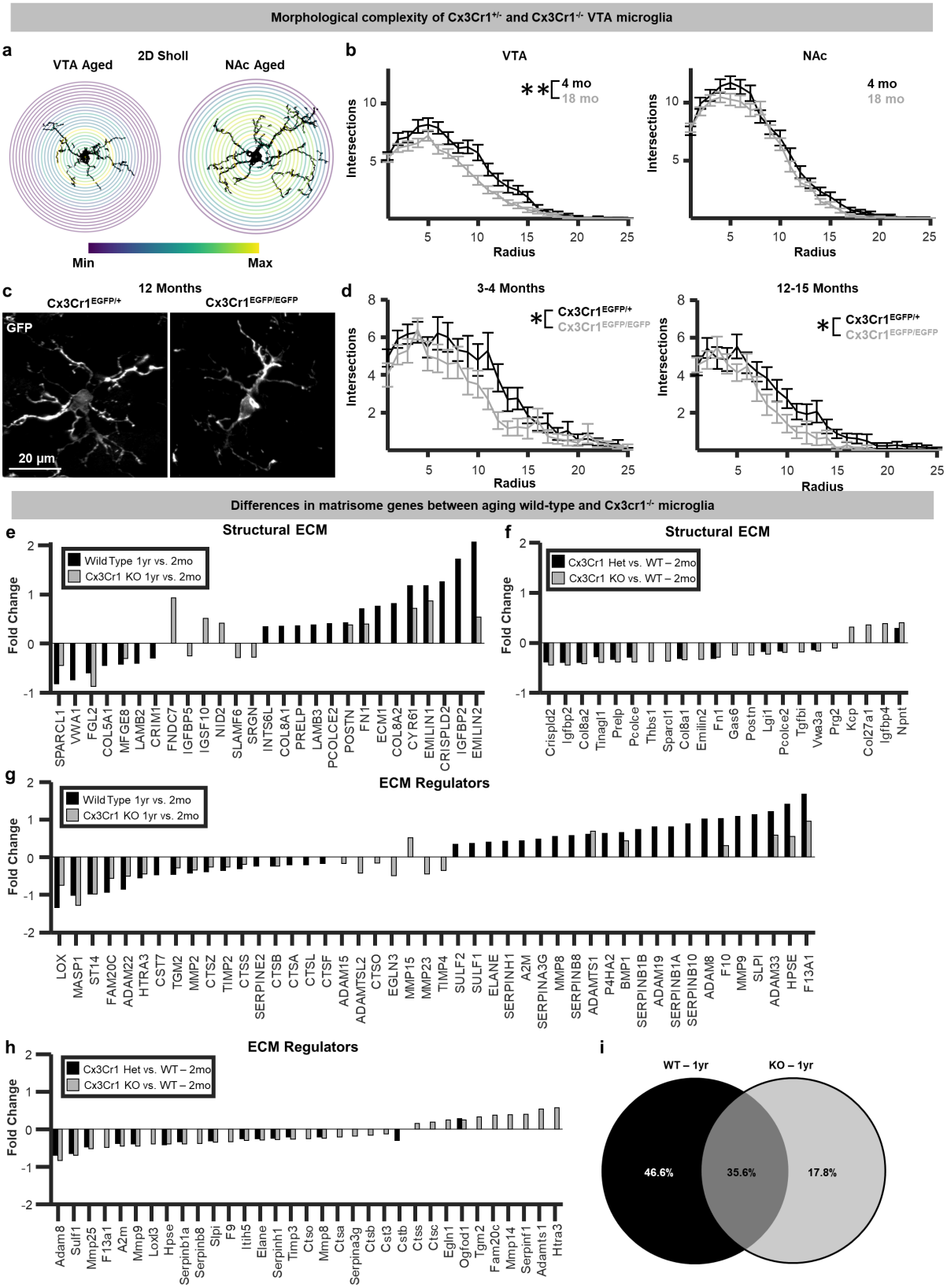
Morphological complexity of Cx3Cr1+/- and Cx3Cr1-/- VTA microglia
a
VTA Aged
2D Sholl
NAc Aged
Min
Max
b
VTA
NAc
4 mo
18 mo
Intersections
Radius
c
12 Months
Cx3Cr1EGFP/+
Cx3Cr1EGFP/EGFP
GFP
20 µm
d
3-4 Months
12-15 Months
Cx3Cr1EGFP/+
Cx3Cr1EGFP/EGFP
Differences in matrisome genes between aging wild-type and Cx3cr1-/- microglia
e
Structural ECM
Wild Type 1yr vs. 2mo
Cx3Cr1 KO 1yr vs. 2mo
Fold Change
SPARCL1 VWA1 FGL2 COL5A1 MFGE8 LAMB2 CRIM1 FNDC7 IGFBP5 IGSF10 NID2 SLAMF6 SRGN INTS6L COL8A1 PRELP LAMB3 PCOLCE2 POSTN FN1 ECM1 COL8A2 CYR61 EMILIN1 CRISPLD2 IGFBP2 EMILIN2
f
Structural ECM
Cx3Cr1 Het vs. WT – 2mo
Cx3Cr1 KO vs. WT – 2mo
Crispld2 Igfbp2 Col8a2 Tinagl1 Prelp Pcolce Thbs1 Sparcl1 Col8a1 Emilin2 Fn1 Gas6 Postn Lgi1 Pcolce2 Tgfbi Vwa3a Prg2 Kcp Col27a1 Igfbp4 Npnt
g
ECM Regulators
Wild Type 1yr vs. 2mo
Cx3Cr1 KO 1yr vs. 2mo
Fold Change
LOX MASP1 ST14 FAM20C ADAM22 HTRA3 CST7 TGM2 MMP2 CTSZ TIMP2 CTSS SERPINE2 CTSB CTSA CTSL CTSF ADAM15 ADAMTSL2 CTSO EGLN3 MMP15 MMP23 TIMP4 SULF2 SULF1 ELANE SERPINH1 A2M SERPINA3G MMP8 SERPINB8 ADAMTS1 P4HA2 BMP1 SERPINB1B ADAM19 SERPINB1A SERPINB10 ADAM8 F10 MMP9 SLPI ADAM33 HPSE F13A1
h
ECM Regulators
Cx3Cr1 Het vs. WT – 2mo
Cx3Cr1 KO vs. WT – 2mo
Fold Change
Adam8 Sulf1 Mmp25 F13a1 A2m Mmp9 Loxl3 Hpse Serpinb1a Serpinb8 Slpi F9 Itih5 Elane Serpinh1 Timp3 Ctso Mmp8 Ctsa Serpina3g Ctsb Cst3 Cstb Ctss Ctsc Egln1 Ogfod1 Tgm2 Fam20c Mmp14 Serpinf1 Adamts1 Htra3
i
WT – 1yr
KO – 1yr
46.6%
35.6%
17.8%

1364 **Extended Data Figure 4). a)** 2-dimensional Sholl analysis was performed on ventral tegmental
1365 area (VTA) and nucleus accumbens (NAc) IBA1-positive microglia in young-adult (4 months)
1366 and late-middle-aged (18 months) mice. **b)** Sholl intersection plots for VTA and NAc microglia
1367 for young-adult and late-middle-aged mice. Middle-aged VTA microglia exhibited a reduced
1368 morphological complexity compared to young adults ($p < 0.01$; n-way ANOVA). **c)** Example
1369 photomicrographs of GFP-positive microglia in the VTA of 12-month-old $Cx3Cr1^{EGFP/+}$(het) and
1370 $Cx3Cr1^{EGFP/EGFP}$ (KO) mice. **d)** Sholl intersection plots for VTA microglia from young-adult (3-4
1371 months) and early-middle-aged Cx3Cr1-het and Cx3Cr1-KO mice. Cx3Cr1 knockout microglia
1372 exhibited a reduced morphological complexity compared to both young-adult and middle-aged
1373 mice ($p < 0.01$; n-way ANOVA). **e)** Fold changes of structural matrisome genes that were
1374 significantly differentially expressed between 1-year and 2-month wild-type (black) and Cx3Cr1-
1375 knockout (grey) microglia (from Gyoneva et al., 2019). **f)** Fold changes of structural matrisome
1376 genes that were significantly differentially expressed between 2-month Cx3Cr1 heterozygous
1377 (black) and Cx3Cr1-knockout (grey) microglia. **g)** Fold changes of regulatory matrisome genes
1378 that were significantly differentially expressed between 1 year and 2 month wild-type (black) and
1379 Cx3Cr1-knockout (grey) microglia. **h)** Fold changes of regulatory matrisome genes that were
1380 significantly differentially expressed between 2-month Cx3Cr1 heterozygous (black) and
1381 Cx3Cr1-knockout (grey) microglia. **i)** Venn diagram depicting the proportion of matrisome-
1382 related genes that were uniquely impacted by age in wild-type and Cx3Cr1-knockout microglia
1383 (top).

1384

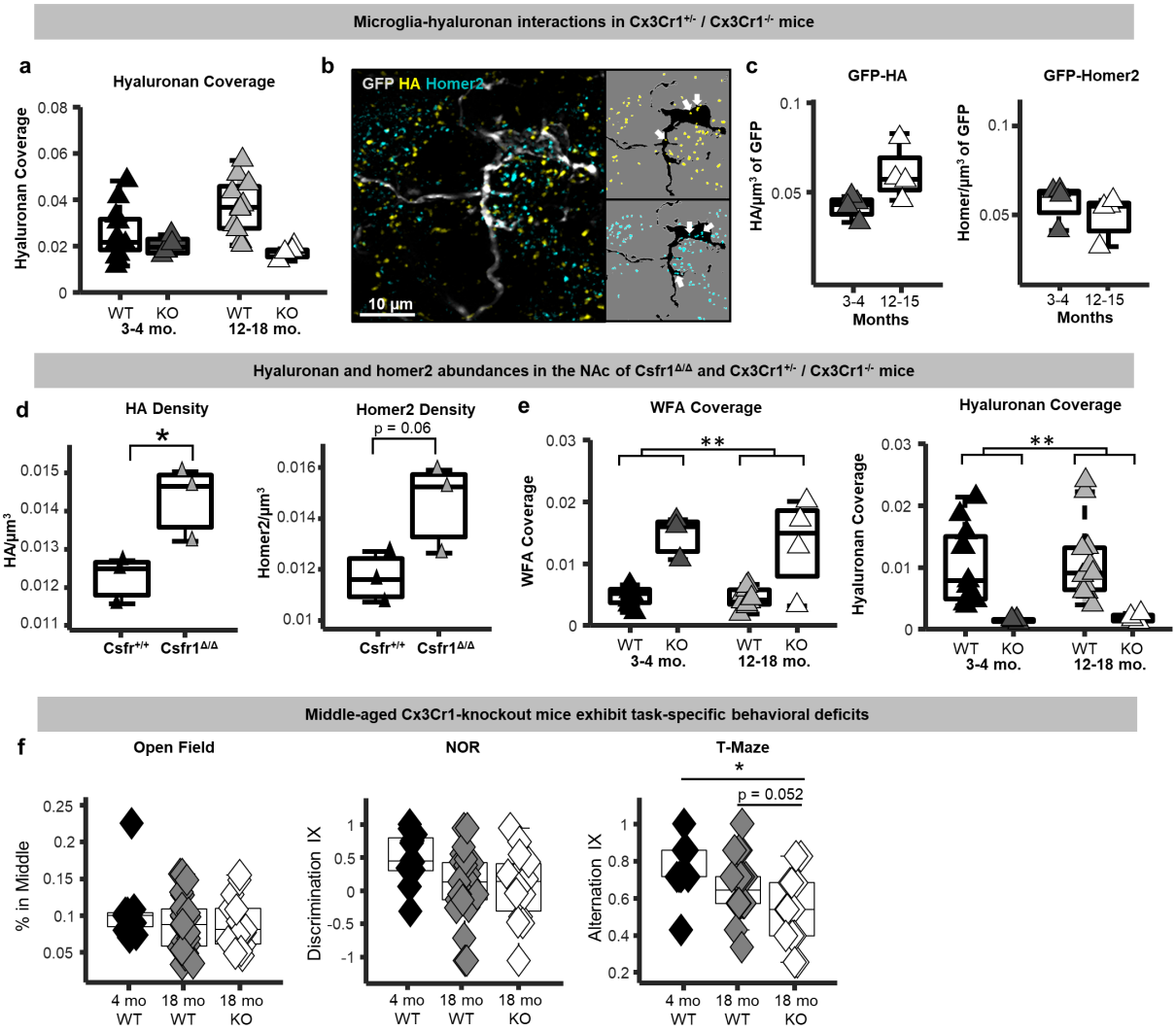
Microglia-hyaluronan interactions in Cx3Cr1+/- / Cx3Cr1-/- mice
a
Hyaluronan Coverage
Hyaluronan Coverage
0.08
0.06
0.04
0.02
0
WT KO WT KO
3-4 mo. 12-18 mo.
b
GFP HA Homer2
10 µm
c
GFP-HA
HA/µm3 of GFP
0.1
0.05
3-4 12-15
Months
GFP-Homer2
Homer/µm3 of GFP
0.1
0.05
3-4 12-15
Months
Hyaluronan and homer2 abundances in the NAc of Csfr1Δ/Δ and Cx3Cr1+/- / Cx3Cr1-/- mice
d
HA Density
*
HA/µm3
0.015
0.014
0.013
0.012
0.011
Csfr+/+ Csfr1Δ/Δ
Homer2 Density
p = 0.06
Homer2/µm3
0.016
0.014
0.012
0.01
Csfr+/+ Csfr1Δ/Δ
e
WFA Coverage
**
WFA Coverage
0.03
0.02
0.01
0
WT KO WT KO
3-4 mo. 12-18 mo.
Hyaluronan Coverage
**
Hyaluronan Coverage
0.03
0.02
0.01
0
WT KO WT KO
3-4 mo. 12-18 mo.
Middle-aged Cx3Cr1-knockout mice exhibit task-specific behavioral deficits
f
Open Field
% in Middle
0.25
0.2
0.15
0.1
0.05
4 mo 18 mo 18 mo
WT WT KO
NOR
Discrimination IX
1
0.5
0
-0.5
-1
4 mo 18 mo 18 mo
WT WT KO
T-Maze
*
p = 0.052
Alternation IX
1
0.8
0.6
0.4
0.2
4 mo 18 mo 18 mo
WT WT KO

1385

1386

1387 **Extended Data Figure 5. a)** VTA hyaluronan tissue coverage in young-adult (3-4 months) and
1388 middle-aged (12-18 months) wild-type and Cx3Cr1-knockout ($Cx3Cr1^{EGFP/EGFP}$) mice. **b)** Putative
1389 microglia engulfment of hyaluronan and homer2 was also examined in $Cx3Cr1^{EGFP/EGFP}$ mice. **c)**
1390 Putative microglia-hyaluronan engulfment and microglia-homer2 engulfment in $Cx3Cr1^{EGFP/EGFP}$
1391 mice. **d)** NAc hyaluronan fibril and homer2 puncta densities in $Csf1r^{+/+}$ (black triangles) and
1392 $Csf1r^{\Delta FIRE/\Delta FIRE}$ (grey triangles) mice. There was a significant increase in hyaluronan abundance
1393 in the $Csf1r^{\Delta FIRE/\Delta FIRE}$ mice compared to control ($p < 0.05$; unpaired t-test). **e)** WFA and
1394 hyaluronan tissue coverage in the NAc of young-adult (3-4 months) and middle-aged (12-18
1395 months) wild-type and Cx3Cr1-knockout ($Cx3Cr1^{EGFP/EGFP}$) mice. **f)** Performance of young-adult
1396 (4 months) wild-type, middle-aged wild-type (18 months), and middle-aged (18 months) Cx3Cr1-
1397 knockout mice on an open field test, a novel object recognition test, and a T-Maze test.

1398

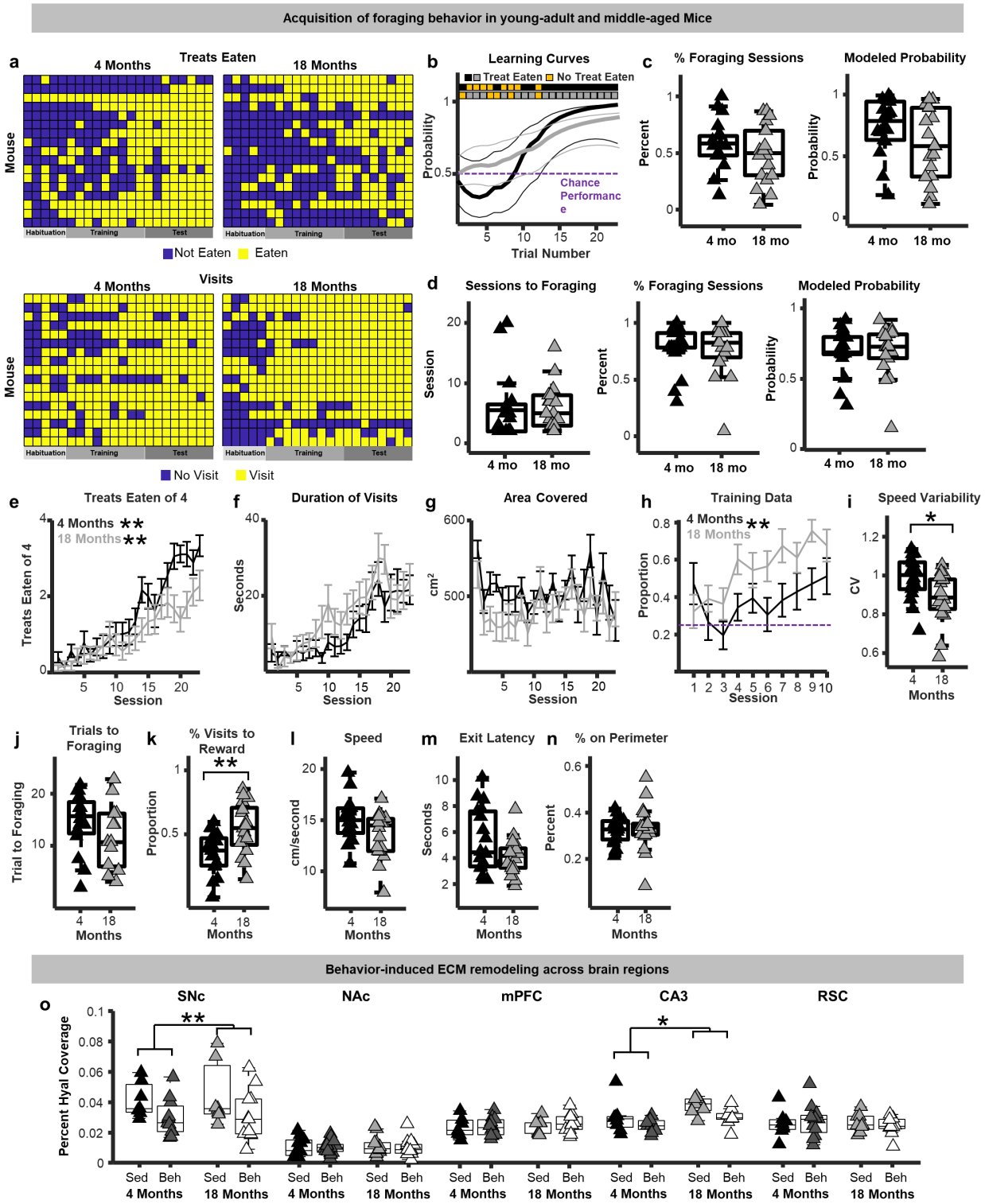
Acquisition of foraging behavior in young-adult and middle-aged Mice
a
Treats Eaten
4 Months
18 Months
Mouse
Habituation
Training
Test
Not Eaten
Eaten
Visits
No Visit
Visit
b
Learning Curves
Treat Eaten
No Treat Eaten
Probability
Chance Performance
Trial Number
c
% Foraging Sessions
Modeled Probability
Percent
Probability
4 mo
18 mo
d
Sessions to Foraging
Session
e
Treats Eaten of 4
Treats Eaten of 4
Session
f
Duration of Visits
Seconds
g
Area Covered
cm²
h
Training Data
Proportion
i
Speed Variability
CV
Months
j
Trials to Foraging
Trial to Foraging
k
% Visits to Reward
Proportion
l
Speed
cm/second
m
Exit Latency
Seconds
n
% on Perimeter
Percent
Behavior-induced ECM remodeling across brain regions
o
SNc
NAc
mPFC
CA3
RSC
Percent Hyal Coverage
Sed
Beh
4 Months
18 Months

Extended Data Figure 6. **a)** Behavioral raster plots of treats eaten (top) and feeder visits (bottom) during encoding across sessions used for hidden Markov modeling of foraging behavior. **b)** Representative learning curves from hidden Markov modeling for a young-adult and late-middle-aged mouse. **c)** The proportion of sessions mice exhibited foraging behavior (ate at least 1 treat), and modeled estimates of the probability of foraging using **c)** treat-eaten and **d)** feeder visits data for young-adult (4 months; black) and late-middle-aged (18 months; grey) mice. **e)** The number of treats eaten (of 4) across all encoding sessions for young-adult and middle-aged mice. Both young-adult and middle-aged mice exhibited increases in the number of treats eaten across foraging sessions ($p < 0.01$; n-way ANOVA). **f)** The duration of feeder visits also increased across sessions ($p < 0.01$; n-way ANOVA). **g)** The area covered across sessions for young-adult and late-middle-aged mice. **h)** The proportion of feeder visits to the correct feeder location during training sessions for young-adult and late-middle-aged mice. Middle-aged mice made more correct feeder visits during training compared to middle-aged ($p < 0.01$; n-way ANOVA). **i)** Variability in running speeds for young-adult and late-middle-aged mice. Middle-aged mice exhibited lower running speed variability compared to young ($p < 0.05$; unpaired t-test). **j)** The number of trials to consistent foraging behavior. **k)** The proportion of rewarded feeder visits across training sessions. A greater proportion of feeder visits were to the rewarded feeder in older mice ($p < 0.01$; unpaired t-test). **l)** Average running speed, **m)** the latency to exit the start box, and **n)** proportion of time on the perimeter of the arena. **o)** Boxplots depicting hyaluronan (hyal) tissue coverage in young-adult sedentary (black) and behavior-trained (dark grey) mice and late-middle-aged sedentary (light grey) and behavior-trained mice (white) in substantia nigra pars compacta (SNc), nucleus accumbens (NAc)**,** medial prefrontal cortex (mPFC), CA3 region of the hippocampus, and retrosplenial cortex (RSC). Significant behavior-induced hyaluronan remodeling was observed in the SNc ($p < 0.01$; n-way ANOVA) and CA3 ($p < 0.05$; n-way ANOVA), but not in the NAc, mPFC, or RSC.

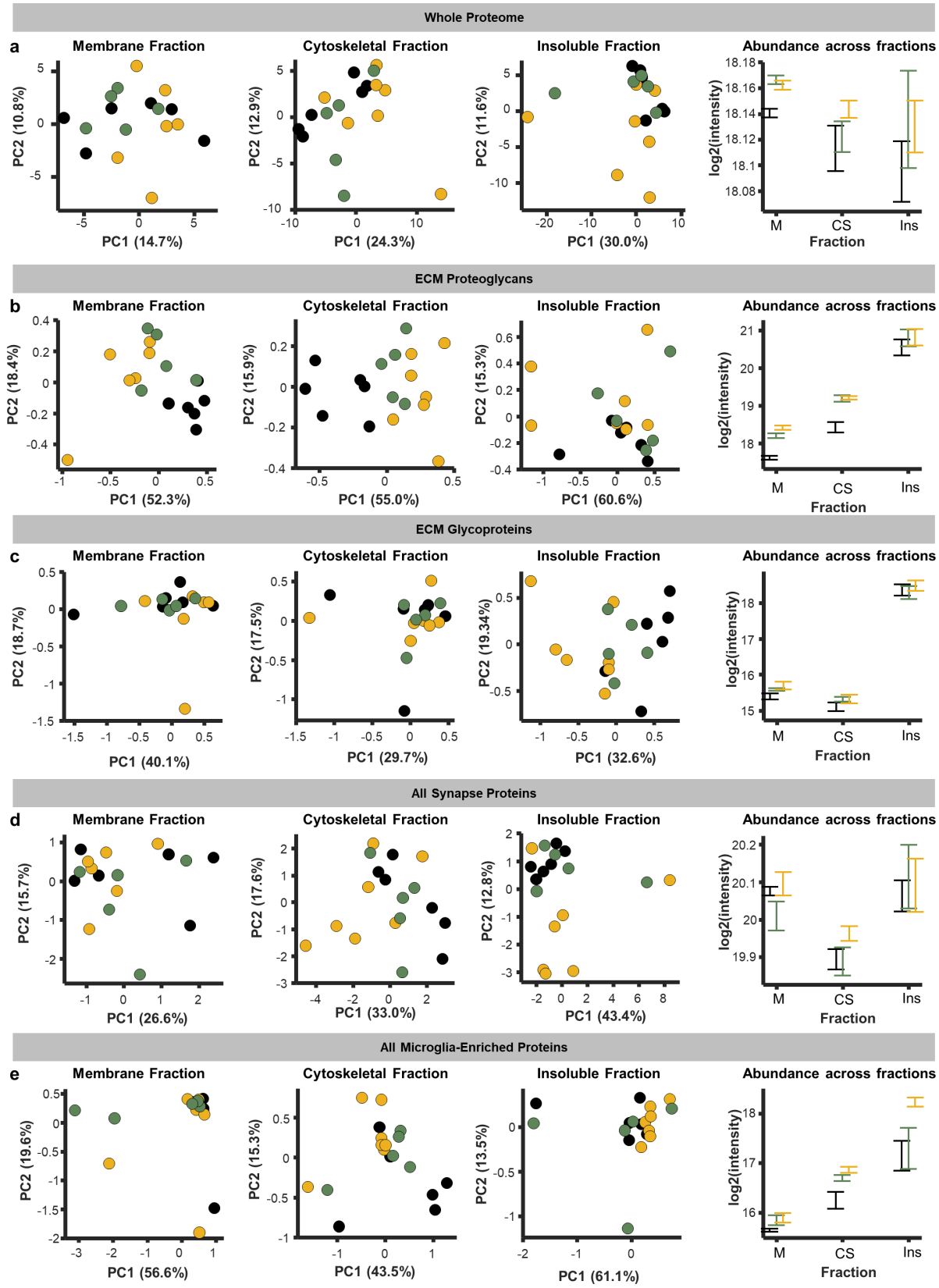
Whole Proteome
a
Membrane Fraction
PC2 (10.8%)
PC1 (14.7%)
Cytoskeletal Fraction
PC2 (12.9%)
PC1 (24.3%)
Insoluble Fraction
PC2 (11.6%)
PC1 (30.0%)
Abundance across fractions
log2(intensity)
M
CS
Ins
Fraction
ECM Proteoglycans
b
Membrane Fraction
PC2 (18.4%)
PC1 (52.3%)
Cytoskeletal Fraction
PC2 (15.9%)
PC1 (55.0%)
Insoluble Fraction
PC2 (15.3%)
PC1 (60.6%)
Abundance across fractions
log2(intensity)
M
CS
Ins
Fraction
ECM Glycoproteins
c
Membrane Fraction
PC2 (18.7%)
PC1 (40.1%)
Cytoskeletal Fraction
PC2 (17.5%)
PC1 (29.7%)
Insoluble Fraction
PC2 (19.34%)
PC1 (32.6%)
Abundance across fractions
log2(intensity)
M
CS
Ins
Fraction
All Synapse Proteins
d
Membrane Fraction
PC2 (15.7%)
PC1 (26.6%)
Cytoskeletal Fraction
PC2 (17.6%)
PC1 (33.0%)
Insoluble Fraction
PC2 (12.8%)
PC1 (43.4%)
Abundance across fractions
log2(intensity)
M
CS
Ins
Fraction
All Microglia-Enriched Proteins
e
Membrane Fraction
PC2 (19.6%)
PC1 (56.6%)
Cytoskeletal Fraction
PC2 (15.3%)
PC1 (43.5%)
Insoluble Fraction
PC2 (13.5%)
PC1 (61.1%)
Abundance across fractions
log2(intensity)
M
CS
Ins
Fraction

1427

1428

1429 **Extended Data Figure 7. a)** PCA plots of whole proteomes from membrane, cytoskeletal, and
1430 insoluble fractions (left 3 panels), and average log2-transformed protein intensities of the whole
1431 proteome across subcellular fractions. **b)** PCA plots of ECM proteoglycans from membrane,
1432 cytoskeletal, and insoluble fractions (left 3 panels), and average log2-transformed protein
1433 intensities of ECM proteoglycans across fractions. **c)** PCA plots of ECM glycoproteins from
1434 membrane, cytoskeletal, and insoluble fractions (left 3 panels), and average log2-transformed
1435 protein intensities of ECM glycoproteins across subcellular fractions. **d)** PCA plots of synapse
1436 proteins from membrane, cytoskeletal, and insoluble fractions (left 3 panels), and average log2-
1437 transformed protein intensities of synapse proteins across subcellular fractions. **e)** PCA plots of
1438 all microglia-enriched proteins from membrane, cytoskeletal, and insoluble fractions (left 3
1439 panels), and average log2-transformed protein intensities of microglia-enriched proteins across
1440 subcellular fractions.

1441

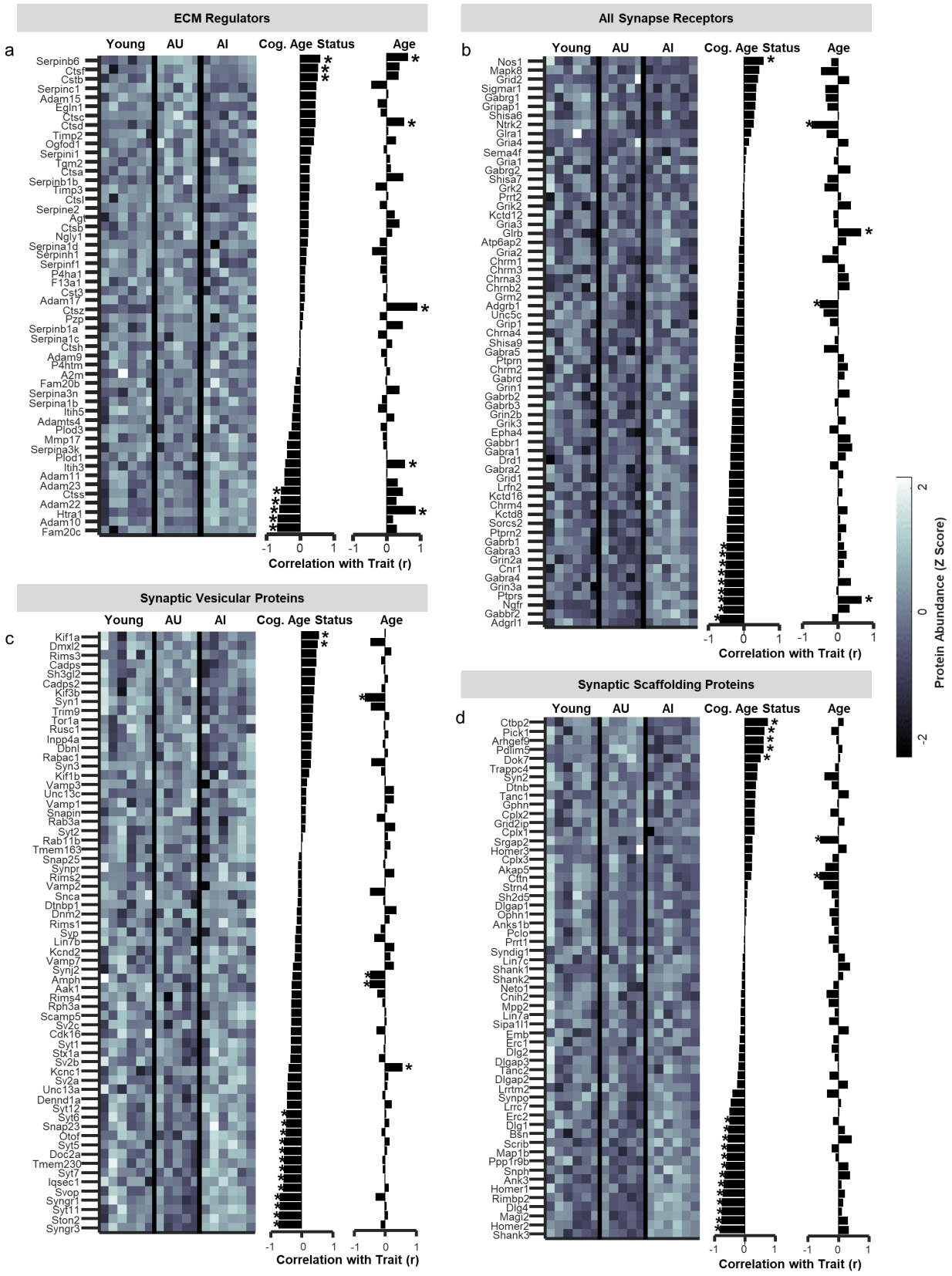
ECM Regulators
a
Young
AU
AI
Cog. Age Status
Age
Serpinb6
Ctsf
Cstb
Serpinc1
Adam15
Egln1
Ctsc
Ctsd
Timp2
Ogfod1
Serpini1
Tgm2
Ctsa
Serpinb1b
Timp3
Ctsl
Serpine2
Agt
Ctsb
Ngly1
Serpina1d
Serpinh1
Serpinf1
P4ha1
F13a1
Cst3
Adam17
Ctsz
Pzp
Serpinb1a
Serpina1c
Ctsh
Adam9
P4htm
A2m
Fam20b
Serpina3n
Serpina1b
Itih5
Adamts4
Plod3
Mmp17
Serpina3k
Plod1
Itih3
Adam11
Adam23
Ctss
Adam22
Htra1
Adam10
Fam20c
-1 0 1
Correlation with Trait (r)
All Synapse Receptors
b
Nos1
Mapk8
Grid2
Sigmar1
Gabrg1
Gripap1
Shisa6
Ntrk2
Glra1
Gria4
Sema4f
Gria1
Gabrg2
Shisa7
Grk2
Prrt2
Grik2
Kctd12
Gria3
Glrb
Atp6ap2
Gria2
Chrm1
Chrm3
Chrna3
Chrnb2
Grm2
Adgrb1
Unc5c
Grip1
Chrna4
Shisa9
Gabra5
Ptprn
Chrm2
Gabrd
Grin1
Gabrb2
Gabrb3
Grin2b
Grik3
Epha4
Gabbr1
Gabra1
Drd1
Gabra2
Grid1
Lrfn2
Kctd16
Chrm4
Kctd8
Sorcs2
Ptprn2
Gabrb1
Gabra3
Grin2a
Cnr1
Gabra4
Grin3a
Ptprs
Ngfr
Gabbr2
Adgrl1
Protein Abundance (Z Score)
2
0
-2
Synaptic Vesicular Proteins
c
Kif1a
Dmxl2
Rims3
Cadps
Sh3gl2
Cadps2
Kif3b
Syn1
Trim9
Tor1a
Rusc1
Inpp4a
Dbnl
Rabac1
Syn3
Kif1b
Vamp3
Unc13c
Vamp1
Snapin
Rab3a
Syt2
Rab11b
Tmem163
Snap25
Synpr
Rims2
Vamp2
Snca
Dtnbp1
Dnm2
Rims1
Syp
Lin7b
Kcnd2
Vamp7
Synj2
Amph
Aak1
Rims4
Rph3a
Scamp5
Sv2c
Cdk16
Syt1
Stx1a
Sv2b
Kcnc1
Sv2a
Unc13a
Dennd1a
Syt12
Syt6
Snap23
Otof
Syt5
Doc2a
Tmem230
Syt7
Iqsec1
Svop
Syngr1
Syt11
Ston2
Syngr3
Synaptic Scaffolding Proteins
d
Ctbp2
Pick1
Arhgef9
Pdlim5
Dok7
Trappc4
Syn2
Dtnb
Tanc1
Gphn
Cplx2
Grid2ip
Cplx1
Srgap2
Homer3
Cplx3
Akap5
Cttn
Strn4
Sh2d5
Dlgap1
Ophn1
Anks1b
Pclo
Prrt1
Syndig1
Lin7c
Shank1
Shank2
Neto1
Cnih2
Mpp2
Lin7a
Sipa1l1
Emb
Erc1
Dlg2
Dlgap3
Tanc2
Dlgap2
Lrrtm2
Synpo
Lrrc7
Erc2
Dlg1
Bsn
Scrib
Map1b
Ppp1r9b
Snph
Ank3
Homer1
Rimbp2
Dlg4
Magi2
Homer2
Shank3

1442

1443 **Extended Data Figure 8. a)** Heat plot of all detected ECM regulatory proteins abundances and
1444 bar plots of their relationship with cognitive status and age (* $p < 0.05$; linear probability model).
1445 **b)** Heat plot of all detected excitatory, inhibitory, and neuromodulator receptor abundances and
1446 bar plots of their relationship with cognitive status and age (* $p < 0.05$; linear probability model).
1447 **c)** Heat plot of all detected synaptic vesicle proteins abundances and bar plots of their
1448 relationship with cognitive status and age (* $p < 0.05$; linear probability model). **d)** Heat plot of all
1449 detected synaptic scaffolding proteins abundances and bar plots of their relationship with
1450 cognitive status and age (* $p < 0.05$; linear probability model).

1451

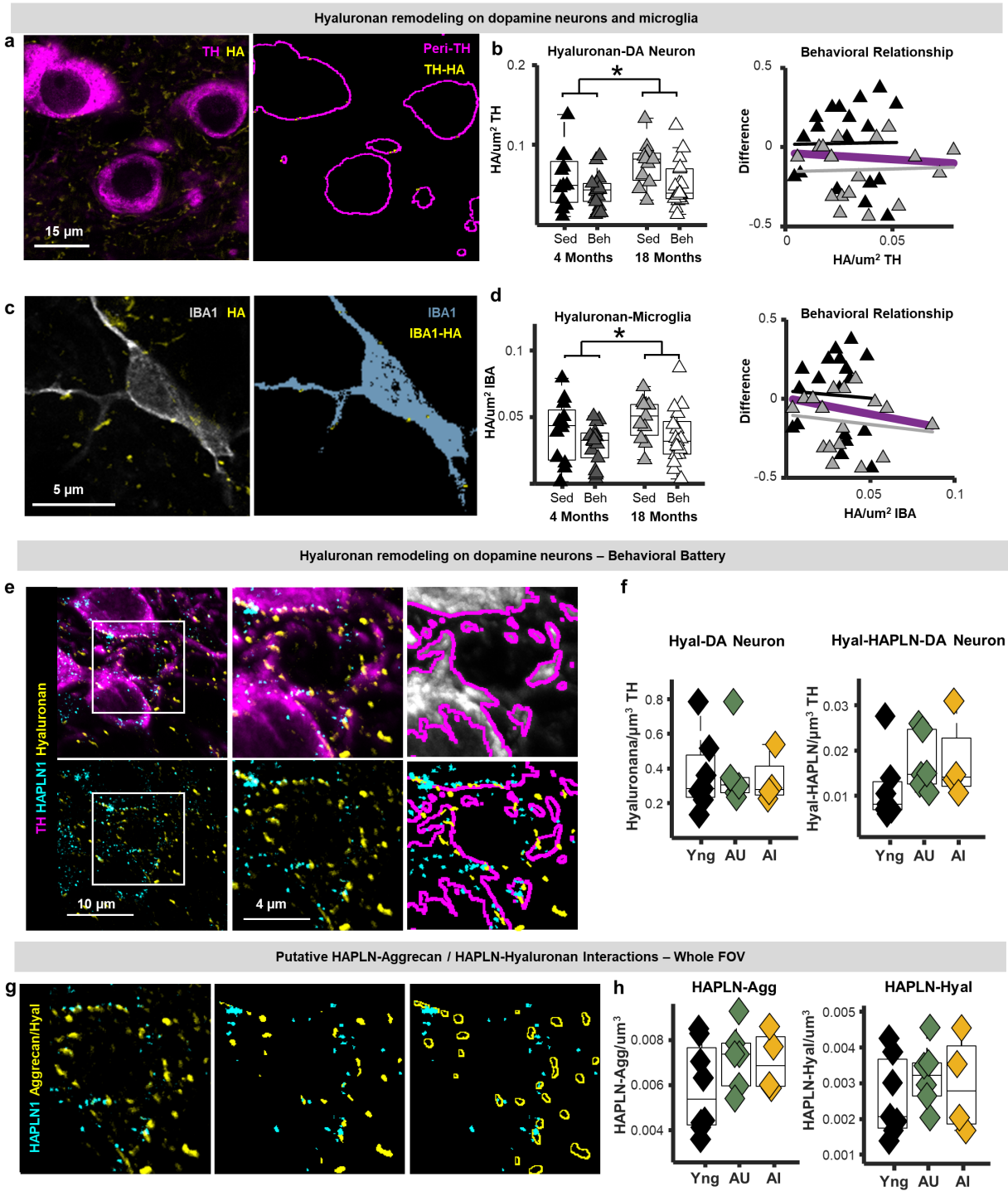
Hyaluronan remodeling on dopamine neurons and microglia
a
TH HA
15 µm
Peri-TH
TH-HA
b
Hyaluronan-DA Neuron
HA/um² TH
Sed Beh Sed Beh
4 Months 18 Months
Behavioral Relationship
Difference
HA/um² TH
c
IBA1 HA
5 µm
IBA1
IBA1-HA
d
Hyaluronan-Microglia
HA/um² IBA
Sed Beh Sed Beh
4 Months 18 Months
Behavioral Relationship
Difference
HA/um² IBA
Hyaluronan remodeling on dopamine neurons – Behavioral Battery
e
TH HAPLN1 Hyaluronan
10 µm
4 µm
f
Hyal-DA Neuron
Hyal-HAPLN-DA Neuron
Hyaluronana/µm³ TH
Hyal-HAPLN/µm³ TH
Yng AU AI
Putative HAPLN-Aggrecan / HAPLN-Hyaluronan Interactions – Whole FOV
g
HAPLN1 Aggrecan/Hyal
h
HAPLN-Agg
HAPLN-Hyal
HAPLN-Agg/um³
HAPLN-Hyal/um³
Yng AU AI

1452

Extended Data Figure 9. a) Left: example photomicrograph of histochemically labelled tyrosine hydroxylase (TH)-positive neurons and hyaluronan in the VTA of a middle-aged mouse. Right: peri-TH ROIs (magenta) used to index hyaluronan fragment on dopamine neurons (hyaluronan-DA neuron; yellow). **b)** Left: Boxplots depicting hyaluronan-DA neuron fibril densities normalized to the TH signal in young-adult sedentary (black) and behavior-trained (dark grey) mice and late-middle-aged sedentary (light grey) and behavior-trained mice (white). Behavior-trained mice exhibited lower hyaluronan-DA neuron densities relative to controls ($p < 0.05$; n-way ANOVA). Right: Relationship between TH-hyaluronan fibril densities and performance on reward-based foraging task (proportion of correct feeder visits difference measure). **c)** Left: example photomicrograph of an IBA1-positive microglia cell body and proximal branches and hyaluronan in the VTA of a middle-aged mouse. Right: IBA1 ROI used to examine hyaluronan fragments in contact with microglia (hyaluronan-microglia). **d)** Left: Boxplots depicting hyaluronan-microglia fibril densities normalized to the IBA1 signal in young-adult sedentary (black) and behavior-trained (dark grey) mice and late-middle-aged sedentary (light grey) and behavior-trained mice (white). Behavior-trained mice exhibited lower IBA1-hyaluronan densities relative to controls ($p < 0.05$; n-way ANOVA). Right: Relationship between IBA1-hyaluronan fibril densities and performance on reward-based foraging task (proportion of correct feeder visits difference measure). **e)** Example photomicrographs of histochemically labelled hyaluronan, hyaluronan and proteoglycan link protein 1 (HAPLN1), and tyrosine hydroxylase (TH) from the VTA of a late-middle aged mouse. The middle panels depict the fields of view depicted by the white squares in the left panel. Right: example of the peri-dopamine neuron region of interest used to estimate the abundance of hyaluronan and HAPLN1 on dopamine neuron surfaces in the VTA. **f)** Boxplots depicting hyaluronan-DA neuron puncta densities (left) and hyaluronan-HAPLN1-DA neuron puncta densities (right) in the VTA of young (black), aging unimpaired (AU; green), and aging impaired (AI; purple) mice. **g)** Schematic of hyaluronan-HAPLN and aggrecan-HAPLN1 proximity analysis to estimate the density of hyaluronan fibrils <0.5 microns from HAPLN1 without respect to the dopamine neuron surfaces. Note: this example photomicrograph is the same as in **e**. **h)** Boxplots depicting aggrecan-HAPLN1 (left) and hyaluronan-HAPLN1 (right) puncta densities (left) in the VTA of young, aging unimpaired (AU), and aging impaired (AI) mice.

1484 **References**

1485 1. Burke, S. N. & Barnes, C. A. Neural plasticity in the ageing brain. *Nat Rev Neurosci* **7**, 30–40 (2006).
1486 2. Tagliaferro, P. & Burke, R. E. Retrograde Axonal Degeneration in Parkinson Disease. *Journal of*
1487 *Parkinson's Disease* **6**, 1–15 (2016).
1488 3. Terry, R. D. *et al.* Physical basis of cognitive alterations in alzheimer's disease: Synapse loss is the
1489 major correlate of cognitive impairment. *Annals of Neurology* **30**, 572–580 (1991).
1490 4. Morrison, J. H. & Baxter, M. G. The ageing cortical synapse: hallmarks and implications for cognitive
1491 decline. *Nat Rev Neurosci* **13**, 240–250 (2012).
1492 5. Dityatev, A., Schachner, M. & Sonderegger, P. The dual role of the extracellular matrix in synaptic
1493 plasticity and homeostasis. *Nat Rev Neurosci* **11**, 735–746 (2010).
1494 6. Sorg, B. A. *et al.* Casting a Wide Net: Role of Perineuronal Nets in Neural Plasticity. *J. Neurosci.* **36**,
1495 11459–11468 (2016).
1496 7. Nguyen, P. T. *et al.* Microglial Remodeling of the Extracellular Matrix Promotes Synapse Plasticity.
1497 *Cell* **182**, 388-403.e15 (2020).
1498 8. Lensjø, K. K., Christensen, A. C., Tennøe, S., Fyhn, M. & Hafting, T. Differential Expression and Cell-
1499 Type Specificity of Perineuronal Nets in Hippocampus, Medial Entorhinal Cortex, and Visual Cortex
1500 Examined in the Rat and Mouse. *eNeuro* **4**, (2017).
1501 9. Dauth, S. *et al.* Extracellular matrix protein expression is brain region dependent. *Journal of*
1502 *Comparative Neurology* **524**, 1309–1336 (2016).
1503 10. Fawcett, J. W. & Kwok, J. C. F. Proteoglycan Sulphation in the Function of the Mature Central
1504 Nervous System. *Frontiers in Integrative Neuroscience* **16**, (2022).
1505 11. Foscarin, S., Raha-Chowdhury, R., Fawcett, J. W. & Kwok, J. C. F. Brain ageing changes proteoglycan
1506 sulfation, rendering perineuronal nets more inhibitory. *Aging (Albany NY)* **9**, 1607–1622 (2017).
1507 12. Ueno, H. *et al.* Age-dependent and region-specific alteration of parvalbumin neurons and
1508 perineuronal nets in the mouse cerebral cortex. *Neurochemistry International* **112**, 59–70 (2018).
1509 13. Maeda, N. Proteoglycans and neuronal migration in the cerebral cortex during development and
1510 disease. *Front. Neurosci.* **9**, (2015).
1511 14. Siddiqui, N., Oshima, K. & Hippensteel, J. A. Proteoglycans and glycosaminoglycans in central
1512 nervous system injury. *Am J Physiol Cell Physiol* **323**, C46–C55 (2022).
1513 15. Dityatev, A., Seidenbecher, C. I. & Schachner, M. Compartmentalization from the outside: the
1514 extracellular matrix and functional microdomains in the brain. *Trends in Neurosciences* **33**, 503–512
1515 (2010).
1516 16. Zhang, Y. *et al.* An RNA-Sequencing Transcriptome and Splicing Database of Glia, Neurons, and
1517 Vascular Cells of the Cerebral Cortex. *J. Neurosci.* **34**, 11929–11947 (2014).
1518 17. Bennett, M. L. *et al.* New tools for studying microglia in the mouse and human CNS. *PNAS* **113**,
1519 E1738–E1746 (2016).
1520 18. De Biase, L. M. *et al.* Local Cues Establish and Maintain Region-Specific Phenotypes of Basal Ganglia
1521 Microglia. *Neuron* **95**, 341-356.e6 (2017).
1522 19. Badimon, A. *et al.* Negative feedback control of neuronal activity by microglia. *Nature* **586**, 417–423
1523 (2020).
1524 20. Cserép, C. *et al.* Microglia monitor and protect neuronal function through specialized somatic
1525 purinergic junctions. *Science* (2020) doi:10.1126/science.aax6752.
1526 21. Miyamoto, A. *et al.* Microglia contact induces synapse formation in developing somatosensory
1527 cortex. *Nat Commun* **7**, 12540 (2016).
1528 22. Paolicelli, R. C. *et al.* Synaptic Pruning by Microglia Is Necessary for Normal Brain Development.
1529 *Science* **333**, 1456–1458 (2011).

1530 23. Schafer, D. P. *et al.* Microglia Sculpt Postnatal Neural Circuits in an Activity and Complement-
1531 Dependent Manner. *Neuron* **74**, 691–705 (2012).
1532 24. Weinhard, L. *et al.* Microglia remodel synapses by presynaptic trogocytosis and spine head filopodia
1533 induction. *Nat Commun* **9**, 1228 (2018).
1534 25. Venturino, A. *et al.* Microglia enable mature perineuronal nets disassembly upon anesthetic
1535 ketamine exposure or 60-Hz light entrainment in the healthy brain. *Cell Reports* **36**, 109313 (2021).
1536 26. Soria, F. N. *et al.* Synucleinopathy alters nanoscale organization and diffusion in the brain
1537 extracellular space through hyaluronan remodeling. *Nat Commun* **11**, 3440 (2020).
1538 27. Crapser, J. D. *et al.* Microglia facilitate loss of perineuronal nets in the Alzheimer's disease brain.
1539 *EBioMedicine* **58**, 102919 (2020).
1540 28. Gray, D. T. *et al.* Retrosplenial cortex microglia and perineuronal net densities are associated with
1541 memory impairment in aged rhesus macaques. *Cerebral Cortex* bhac366 (2022)
1542 doi:10.1093/cercor/bhac366.
1543 29. Bäckman, L., Lindenberger, U., Li, S.-C. & Nyberg, L. Linking cognitive aging to alterations in
1544 dopamine neurotransmitter functioning: Recent data and future avenues. *Neuroscience &*
1545 *Biobehavioral Reviews* **34**, 670–677 (2010).
1546 30. Dahl, M. J. *et al.* The integrity of dopaminergic and noradrenergic brain regions is associated with
1547 different aspects of late-life memory performance. *Nat Aging* **3**, 1128–1143 (2023).
1548 31. Moca, E. N. *et al.* Microglia Drive Pockets of Neuroinflammation in Middle Age. *J. Neurosci.* **42**,
1549 3896–3918 (2022).
1550 32. Naba, A., Clauser, K. R. & Hynes, R. O. Enrichment of Extracellular Matrix Proteins from Tissues and
1551 Digestion into Peptides for Mass Spectrometry Analysis. *J Vis Exp* 53057 (2015) doi:10.3791/53057.
1552 33. McCabe, M. C., Saviola, A. J. & Hansen, K. C. Mass Spectrometry-Based Atlas of Extracellular Matrix
1553 Proteins across 25 Mouse Organs. *J. Proteome Res.* **22**, 790–801 (2023).
1554 34. Langfelder, P. & Horvath, S. WGCNA: an R package for weighted correlation network analysis. *BMC*
1555 *Bioinformatics* **9**, 559 (2008).
1556 35. Hara, Y., Rapp, P. R. & Morrison, J. H. Neuronal and morphological bases of cognitive decline in aged
1557 rhesus monkeys. *Age (Dordr)* **34**, 1051–1073 (2012).
1558 36. Brückner, G. *et al.* Perineuronal nets provide a polyanionic, glia-associated form of
1559 microenvironment around certain neurons in many parts of the rat brain. *Glia* **8**, 183–200 (1993).
1560 37. Carulli, D. *et al.* Composition of perineuronal nets in the adult rat cerebellum and the cellular origin
1561 of their components. *Journal of Comparative Neurology* **494**, 559–577 (2006).
1562 38. Kwok, J. C. F., Dick, G., Wang, D. & Fawcett, J. W. Extracellular matrix and perineuronal nets in CNS
1563 repair. *Developmental Neurobiology* **71**, 1073–1089 (2011).
1564 39. Härtig, W., Meinicke, A., Michalski, D., Schob, S. & Jäger, C. Update on Perineuronal Net Staining
1565 With Wisteria floribunda Agglutinin (WFA). *Front. Integr. Neurosci.* **16**, (2022).
1566 40. Oohashi, T., Edamatsu, M., Bekku, Y. & Carulli, D. The hyaluronan and proteoglycan link proteins:
1567 Organizers of the brain extracellular matrix and key molecules for neuronal function and plasticity.
1568 *Experimental Neurology* **274**, 134–144 (2015).
1569 41. Wilson, E., Knudson, W. & Newell-Litwa, K. Hyaluronan regulates synapse formation and function in
1570 developing neural networks. *Sci Rep* **10**, 16459 (2020).
1571 42. Frischknecht, R. *et al.* Brain extracellular matrix affects AMPA receptor lateral mobility and short-
1572 term synaptic plasticity. *Nat Neurosci* **12**, 897–904 (2009).
1573 43. Rojo, R. *et al.* Deletion of a Csf1r enhancer selectively impacts CSF1R expression and development
1574 of tissue macrophage populations. *Nat Commun* **10**, 3215 (2019).
1575 44. Gyoneva, S. *et al.* Cx3cr1-deficient microglia exhibit a premature aging transcriptome. *Life Sci*
1576 *Alliance* **2**, e201900453 (2019).

1577 45. Gunner, G. *et al.* Sensory lesioning induces microglial synapse elimination via ADAM10 and
1578 fractalkine signaling. *Nat Neurosci* **22**, 1075–1088 (2019).
1579 46. Rivas-Fuentes, S. *et al.* CX3CL1 and CX3CR1 could be a relevant molecular axis in the
1580 pathophysiology of idiopathic pulmonary fibrosis. *Int J Med Sci* **17**, 2357–2361 (2020).
1581 47. Song, K. H., Park, J., Park, J. H., Natarajan, R. & Ha, H. Fractalkine and its receptor mediate
1582 extracellular matrix accumulation in diabetic nephropathy in mice. *Diabetologia* **56**, 1661–1669
1583 (2013).
1584 48. Gray, D. T. & Barnes, C. A. Distinguishing adaptive plasticity from vulnerability in the aging
1585 hippocampus. *Neuroscience* **309**, 17–28 (2015).
1586 49. Bäckman, L., Nyberg, L., Lindenberger, U., Li, S.-C. & Farde, L. The correlative triad among aging,
1587 dopamine, and cognition: Current status and future prospects. *Neuroscience & Biobehavioral*
1588 *Reviews* **30**, 791–807 (2006).
1589 50. Nyberg, L., Lövdén, M., Riklund, K., Lindenberger, U. & Bäckman, L. Memory aging and brain
1590 maintenance. *Trends in Cognitive Sciences* **16**, 292–305 (2012).
1591 51. Chang, M. C. *et al.* Narp regulates homeostatic scaling of excitatory synapses on parvalbumin-
1592 expressing interneurons. *Nat Neurosci* **13**, 1090–1097 (2010).
1593 52. Soles, A. *et al.* Extracellular Matrix Regulation in Physiology and in Brain Disease. *Int J Mol Sci* **24**,
1594 7049 (2023).
1595 53. Sugitani, K. *et al.* Hyaluronan degradation and release of a hyaluronan-aggrecan complex from
1596 perineuronal nets in the aged mouse brain. *Biochimica et Biophysica Acta (BBA) - General Subjects*
1597 **1865**, 129804 (2021).
1598 54. Cargill, R. *et al.* Astrocytes in aged non-human primate brain gray matter synthesize excess
1599 hyaluronan. *Neurobiol Aging* **33**, 830.e13-830.e24 (2012).
1600 55. Geinisman, Y., de Toledo-Morrell, L. & Morrell, F. Loss of perforated synapses in the dentate gyrus:
1601 morphological substrate of memory deficit in aged rats. *Proc Natl Acad Sci U S A* **83**, 3027–3031
1602 (1986).
1603 56. Dumitriu, D. *et al.* Selective Changes in Thin Spine Density and Morphology in Monkey Prefrontal
1604 Cortex Correlate with Aging-Related Cognitive Impairment. *J. Neurosci.* **30**, 7507–7515 (2010).
1605 57. Pizzorusso, T. *et al.* Reactivation of Ocular Dominance Plasticity in the Adult Visual Cortex. *Science*
1606 (2002) doi:10.1126/science.1072699.
1607 58. Morgan, B. P. Complement in the pathogenesis of Alzheimer's disease. *Semin Immunopathol* **40**,
1608 113–124 (2018).
1609 59. Wilton, D. K. *et al.* Microglia and complement mediate early corticostriatal synapse loss and
1610 cognitive dysfunction in Huntington's disease. *Nat Med* **29**, 2866–2884 (2023).
1611 60. Végh, M. J. *et al.* Hippocampal Extracellular Matrix Levels and Stochasticity in Synaptic Protein
1612 Expression Increase with Age and Are Associated with Age-dependent Cognitive Decline*. *Molecular*
1613 *& Cellular Proteomics* **13**, 2975–2985 (2014).
1614 61. Soto, J. S. *et al.* Astrocyte–neuron subproteomes and obsessive–compulsive disorder mechanisms.
1615 *Nature* 1–10 (2023) doi:10.1038/s41586-023-05927-7.
1616 62. Tsien, R. Y. Very long-term memories may be stored in the pattern of holes in the perineuronal net.
1617 *PNAS* **110**, 12456–12461 (2013).
1618 63. Fawcett, J. W. *et al.* The extracellular matrix and perineuronal nets in memory. *Mol Psychiatry* **27**,
1619 3192–3203 (2022).
1620 64. Pignataro, A. *et al.* Activity-Induced Amyloid-β Oligomers Drive Compensatory Synaptic
1621 Rearrangements in Brain Circuits Controlling Memory of Presymptomatic Alzheimer's Disease Mice.
1622 *Biological Psychiatry* **86**, 185–195 (2019).
1623 65. Bhembre, N., Bonthron, C. & Opazo, P. Synaptic Compensatory Plasticity in Alzheimer's Disease. *J*
1624 *Neurosci* **43**, 6833–6840 (2023).

66. Chipman, P. H. Synapse-Specific Reinnervation in the Injured Brain. *J Neurosci* **36**, 10239–10241 (2016).
67. Kim, A. *et al.* Reduced Fractalkine Levels Lead to Striatal Synaptic Plasticity Deficits in Huntington's Disease. *Front Cell Neurosci* **14**, 163 (2020).
68. Stephan, A. H. *et al.* A Dramatic Increase of C1q Protein in the CNS during Normal Aging. *J. Neurosci.* **33**, 13460–13474 (2013).
69. Cangalaya, C., Sun, W., Stoyanov, S., Dunay, I. R. & Dityatev, A. Integrity of neural extracellular matrix is required for microglia-mediated synaptic remodeling. *Glia* **72**, 1874–1892 (2024).
70. Scott-Hewitt, N. *et al.* Microglial-derived C1q integrates into neuronal ribonucleoprotein complexes and impacts protein homeostasis in the aging brain. *Cell* **187**, 4193-4212.e24 (2024).
71. Mitlöhner, J. *et al.* Dopamine Receptor Activation Modulates the Integrity of the Perisynaptic Extracellular Matrix at Excitatory Synapses. *Cells* **9**, 260 (2020).
72. Park, D. C. & Bischof, G. N. The aging mind: neuroplasticity in response to cognitive training. *Dialogues Clin Neurosci* **15**, 109–119 (2013).
73. Reuter-Lorenz, P. A. & Park, D. C. Cognitive aging and the life course: A new look at the Scaffolding theory. *Current Opinion in Psychology* **56**, 101781 (2024).
74. Spiegel, A. M., Koh, M. T., Vogt, N. M., Rapp, P. R. & Gallagher, M. Hilar interneuron vulnerability distinguishes aged rats with memory impairment. *Journal of Comparative Neurology* **521**, 3508–3523 (2013).
75. Khoshneviszadeh, M. *et al.* Microvascular damage, neuroinflammation and extracellular matrix remodeling in *Col18a1* knockout mice as a model for early cerebral small vessel disease. *Matrix Biology* **128**, 39–64 (2024).
76. Badran, A., Hollocks, M. J., Brookes, R. L., Morris, R. G. & Markus, H. S. Framingham vascular age is associated with worse cognitive performance in the middle-aged and elderly. *Neuropsychol Dev Cogn B Aging Neuropsychol Cogn* **26**, 531–540 (2019).
77. Toth, P., Tarantini, S., Csiszar, A. & Ungvari, Z. Functional vascular contributions to cognitive impairment and dementia: mechanisms and consequences of cerebral autoregulatory dysfunction, endothelial impairment, and neurovascular uncoupling in aging. *Am J Physiol Heart Circ Physiol* **312**, H1–H20 (2017).
78. Austin, J. W., Gilchrist, C. & Fehlings, M. G. High molecular weight hyaluronan reduces lipopolysaccharide mediated microglial activation. *Journal of Neurochemistry* **122**, 344–355 (2012).
79. Campo, G. M. *et al.* Small hyaluronan oligosaccharides induce inflammation by engaging both toll-like-4 and CD44 receptors in human chondrocytes. *Biochemical Pharmacology* **80**, 480–490 (2010).
80. Frattini, T. *et al.* Benefits and limits of decellularization on mass-spectrometry-based extracellular matrix proteome analysis of mouse kidney. *PROTEOMICS* **24**, 2400052 (2024).
81. Naba, A. Ten Years of Extracellular Matrix Proteomics: Accomplishments, Challenges, and Future Perspectives. *Molecular & Cellular Proteomics* **22**, 100528 (2023).
82. Naba, A. *et al.* The extracellular matrix: Tools and insights for the "omics" era. *Matrix Biology* **49**, 10–24 (2016).
83. Štepánková, K. *et al.* Low oral dose of 4-methylumbelliferone reduces glial scar but is insufficient to induce functional recovery after spinal cord injury. *Sci Rep* **13**, 19183 (2023).
84. Dubisova, J. *et al.* Oral treatment of 4-methylumbelliferone reduced perineuronal nets and improved recognition memory in mice. *Brain Research Bulletin* **181**, 144–156 (2022).
85. Hill, J. J., Jin, K., Mao, X. O., Xie, L. & Greenberg, D. A. Intracerebral chondroitinase ABC and heparan sulfate proteoglycan glypican improve outcome from chronic stroke in rats. *Proc Natl Acad Sci U S A* **109**, 9155–9160 (2012).
86. Balashova, A. *et al.* Enzymatic Digestion of Hyaluronan-Based Brain Extracellular Matrix in vivo Can Induce Seizures in Neonatal Mice. *Frontiers in Neuroscience* **13**, (2019).

1673 87. George, N. & Geller, H. M. Extracellular Matrix and Traumatic Brain Injury. *J Neurosci Res* **96**, 573–
1674 588 (2018).
1675 88. Loane, D. J. & Byrnes, K. R. Role of Microglia in Neurotrauma. *Neurotherapeutics* **7**, 366–377 (2010).
1676 89. Goertsen, D. *et al.* AAV capsid variants with brain-wide transgene expression and decreased liver
1677 targeting after intravenous delivery in mouse and marmoset. *Nat Neurosci* **25**, 106–115 (2022).
1678 90. Jung, S. *et al.* Analysis of fractalkine receptor CX(3)CR1 function by targeted deletion and green
1679 fluorescent protein reporter gene insertion. *Mol Cell Biol* **20**, 4106–4114 (2000).
1680 91. Hayashi, Y. *et al.* The intrinsic microglial molecular clock controls synaptic strength via the circadian
1681 expression of cathepsin S. *Sci Rep* **3**, 2744 (2013).
1682 92. Ferreira, T. A. *et al.* Neuronal morphometry directly from bitmap images. *Nat Methods* **11**, 982–984
1683 (2014).
1684 93. Jami-Alahmadi, Y., Pandey, V., Mayank, A. K. & Wohlschlegel, J. A. A Robust Method for Packing
1685 High Resolution C18 RP-nano-HPLC Columns. *Journal of Visualized Experiments (JoVE)* e62380 (2021)
1686 doi:10.3791/62380.
1687 94. Cox, J. & Mann, M. MaxQuant enables high peptide identification rates, individualized p.p.b.-range
1688 mass accuracies and proteome-wide protein quantification. *Nat Biotechnol* **26**, 1367–1372 (2008).
1689 95. Batth, T. S. *et al.* Protein Aggregation Capture on Microparticles Enables Multipurpose Proteomics
1690 Sample Preparation. *Mol Cell Proteomics* **18**, 1027–1035 (2019).
1691 96. Demichev, V., Messner, C. B., Vernardis, S. I., Lilley, K. S. & Ralser, M. DIA-NN: neural networks and
1692 interference correction enable deep proteome coverage in high throughput. *Nat Methods* **17**, 41–44
1693 (2020).
1694 97. Hsiao, Y. *et al.* Analysis and visualization of quantitative proteomics data using FragPipe-Analyst.
1695 *bioRxiv* 2024.03.05.583643 (2024) doi:10.1101/2024.03.05.583643.
1696 98. Shao, X. *et al.* MatrisomeDB 2.0: 2023 updates to the ECM-protein knowledge database. *Nucleic*
1697 *Acids Res* **51**, D1519–D1530 (2023).
1698 99. Lynn, D. J. *et al.* InnateDB: facilitating systems-level analyses of the mammalian innate immune
1699 response. *Molecular Systems Biology* **4**, 218 (2008).
1700 100. Koopmans, F. *et al.* SynGO: An Evidence-Based, Expert-Curated Knowledge Base for the Synapse.
1701 *Neuron* **103**, 217-234.e4 (2019).
1702 101. Zhou, Y. *et al.* Metascape provides a biologist-oriented resource for the analysis of systems-level
1703 datasets. *Nat Commun* **10**, 1523 (2019).
1704 102. Takeuchi, T. *et al.* Locus coeruleus and dopaminergic consolidation of everyday memory. *Nature*
1705 **537**, 357–362 (2016).
1706 103. Smith, A. C. *et al.* Dynamic Analysis of Learning in Behavioral Experiments. *J. Neurosci.* **24**, 447–
1707 461 (2004).
1708

Acknowledgements: The authors would like to thank Keionna Newton and Fanny Etienne for providing tissue used in this study. Additionally, we thank Mia Donato and Claribel Charway for important contributions to mouse behavior pipelines used in this study. This work was supported by the American Federation on Aging Research grant number: MCKNIGHT21003, as well as by the Simons foundation Collaboration on Plasticity in the Aging Brain grant number: SFI-AN-NC-AB-Independence Postdoctoral-00007445.

Author Contributions: DTG conceived the study, designed methodology, performed experiments, analyzed data, and wrote the manuscript. **AG** performed behavioral experiments and microglial analysis. **YJA** performed proteomic experiments and proteomic data analysis. **VP** performed proteomic experiments and proteomic data analysis. **LP** performed proteomic experiments comparing ECM enrichment strategies. **YZ** performed proteomic experiments comparing ECM enrichment strategies and provided critical support in manuscript preparation. **JAW** conceptualized proteomic experiments and analysis. **RAM** help conceptualize behavioral experiments and provided critical support in manuscript preparation. **LMD** conceived the study, designed methodology, and wrote the manuscript.

Competing Interests: The authors do not claim any conflicts of interest. This research was supported in part by the Intramural Research Program of the National Institutes of Health (NIH). The contributions of the NIH author(s) were made as part of their official duties as NIH federal employees, are in compliance with agency policy requirements, and are considered Works of the United States Government. However, the findings and conclusions presented in this paper are those of the author(s) and do not necessarily reflect the views of the NIH or the U.S. Department of Health and Human Services.

1733